

AD \_\_\_\_\_  
(Leave blank)

Award Number: W81XWH-07-1-0242

TITLE: Infrared Spectroscopic Imaging for Prostate Pathology Practice

PRINCIPAL INVESTIGATOR: Rohit Bhargava, Ph.D.

CONTRACTING ORGANIZATION: University of Illinois  
Champaign, IL 61820

REPORT DATE: March 2008

TYPE OF REPORT: Annual

PREPARED FOR: U.S. Army Medical Research and Materiel Command  
Fort Detrick, Maryland 21702-5012

DISTRIBUTION STATEMENT: (Check one)

- \* Approved for public release; distribution unlimited
- Distribution limited to U.S. Government agencies only;  
report contains proprietary information

The views, opinions and/or findings contained in this report are those of the author(s) and should not be construed as an official Department of the Army position, policy or decision unless so designated by other documentation.

# REPORT DOCUMENTATION PAGE

*Form Approved  
OMB No. 0704-0188*

Public reporting burden for this collection of information is estimated to average 1 hour per response, including the time for reviewing instructions, searching existing data sources, gathering and maintaining the data needed, and completing and reviewing this collection of information. Send comments regarding this burden estimate or any other aspect of this collection of information, including suggestions for reducing this burden to Department of Defense, Washington Headquarters Services, Directorate for Information Operations and Reports (0704-0188), 1215 Jefferson Davis Highway, Suite 1204, Arlington, VA 22202-4302. Respondents should be aware that notwithstanding any other provision of law, no person shall be subject to any penalty for failing to comply with a collection of information if it does not display a currently valid OMB control number. **PLEASE DO NOT RETURN YOUR FORM TO THE ABOVE ADDRESS.**

<b>1. REPORT DATE (DD-MM-YYYY)</b> 14 - 03 - 2008			<b>2. REPORT TYPE</b> Annual		<b>3. DATES COVERED (From - To)</b> 15 FEB 2007 - 14 FEB 2008	
<b>4. TITLE AND SUBTITLE</b>  Infrared Spectroscopic Imaging for Prostate Pathology			<b>5a. CONTRACT NUMBER</b> W81XWH-07-1-0242		<b>5b. GRANT NUMBER</b>	
					<b>5c. PROGRAM ELEMENT NUMBER</b>	
<b>6. AUTHOR(S)</b>  Rohit Bhargava, Ph.D.  Email: rxb@uiuc.edu			<b>5d. PROJECT NUMBER</b>		<b>5e. TASK NUMBER</b>	
					<b>5f. WORK UNIT NUMBER</b>	
<b>7. PERFORMING ORGANIZATION NAME(S) AND ADDRESS(ES)</b>  University of Illinois 1901 First St. Suite A Champaign, IL 61820					<b>8. PERFORMING ORGANIZATION REPORT NUMBER</b>	
<b>9. SPONSORING / MONITORING AGENCY NAME(S) AND ADDRESS(ES)</b>  US Army Medical Research and Materiel Command 504 Scott Street Fort Detrick, MD 21702-5012					<b>10. SPONSOR/MONITOR'S ACRONYM(S)</b>	
					<b>11. SPONSOR/MONITOR'S REPORT NUMBER(S)</b>	
<b>12. DISTRIBUTION / AVAILABILITY STATEMENT</b> Approved for public release; distribution unlimited						
<b>13. SUPPLEMENTARY NOTES</b>						
<b>14. ABSTRACT</b> The report summarizes progress towards using Fourier transform infrared spectroscopic imaging for prostate pathology. The aim of the work is to enable histopathologic recognition without the use of human input or stains. The major accomplishments are : 1. Optimization of experimental parameters for spectroscopic imaging experiments. The optimization provides an understanding of the classification process and allows ~40 fold decrease in data acquisition time. 2. Classification of prostate histology using Genetic Algorithms. The work explicitly identifies spectroscopic biomarkers needed to classify tissue correctly. 3. A new method is introduced to reduce noise by nearly an order of magnitude. The method is based on post-processing to reduce non-correlated signals in images using the covariance of the recorded data. The method enables a ~7 fold higher signal to noise ratio, which translates into a 50-fold faster data acquisition rate.						
<b>15. SUBJECT TERMS</b> Spectroscopy, prostate, histopathology, cancer, optimization, optical imaging						
<b>16. SECURITY CLASSIFICATION OF:</b> U			<b>17. LIMITATION OF ABSTRACT</b> UU	<b>18. NUMBER OF PAGES</b> 106	<b>19a. NAME OF RESPONSIBLE PERSON</b> USAMRMC	
<b>a. REPORT</b> U	<b>b. ABSTRACT</b> U	<b>c. THIS PAGE</b> U			<b>19b. TELEPHONE NUMBER (include area code)</b>	

## **Table of Contents**

	<u>Page</u>
<b>Introduction.....</b>	<b>4</b>
<b>Body.....</b>	<b>4</b>
<b>Key Research Accomplishments.....</b>	<b>25</b>
<b>Reportable Outcomes.....</b>	<b>25</b>
<b>Conclusion.....</b>	<b>28</b>
<b>References.....</b>	<b>29</b>
<b>Appendices.....</b>	<b>31</b>

## **Introduction**

Prostate cancer accounts for one-third of noncutaneous cancers diagnosed in US men,<sup>1</sup> is a leading cause of cancer-related death and is, appropriately, the subject of heightened public awareness and widespread screening. If prostate-specific antigen (PSA)<sup>2</sup> or digital rectal screens are abnormal,<sup>3</sup> a biopsy is considered to detect or rule out cancer. Pathologic status of biopsied tissue forms the definitive diagnosis for prostate cancer and constitutes an important cornerstone of therapy and prognosis.<sup>4</sup> There is, hence, a need to add useful information to diagnoses and to introduce new technologies that allow efficient analyses of cancer to focus limited healthcare resources. For the reasons underlined above, there is an urgent need for high-throughput, automated and objective pathology tools. Our general hypothesis is that these requirements are satisfied through innovative spectroscopic imaging approaches that are compatible with, and add substantially to, current pathology practice. Hence, the overall aim of this project is to demonstrate the utility of novel Fourier transform infrared (FTIR) spectroscopy-based, computer-aided diagnoses for prostate cancer and develop the required microscopy and software tools to enable its application. FTIR spectroscopic imaging is a new technique that combines the spatial specificity of optical microscopy and the biochemical content of spectroscopy.<sup>5</sup> As opposed to thermal infrared imaging, FTIR imaging measures the absorption properties of tissue through a spectrum consisting of (typically) 1024 to 2048 wavelength elements per pixel.<sup>6</sup> Since mid-IR (2-12  $\mu\text{m}$  wavelength) spectra reflect the molecular composition of the tissue, image contrast arises from differences in endogenous chemical species. As opposed to visible microscopy of stained tissue that requires a human eye to detect changes, numerical computation is required to extract information from IR spectra of unstained tissue. Extracted information, based on a computer algorithm, is inherently objective and automated. Recent work has demonstrated that these determinations are also accurate and reproducible in large patient populations.<sup>7</sup> Hence, we focused, in the first year of this project, on demonstrating that the laboratory results could be optimized using novel approaches to fast imaging. This is a critical step, since we propose next to analyze 375 radical prostatectomy samples. We have been able to optimize data acquisition parameters and develop a novel algorithm for processing data that enables almost 50-fold faster imaging.

We apologize for an incomplete report earlier as the PI misunderstood the length of detail in the body of the report versus attachments.

## **Body**

Specific activities and tasks as per statement of work are below:

*Task 1.* Perform infrared spectroscopic imaging on prostate biopsy specimens

**Goal:** Obtain high throughput IR imaging on prostate biopsy specimens

**Activities:** A focal plane array (FPA) detector was interfaced to an infrared interferometer and microscope to record high-throughput spectroscopic imaging data. A rapid-scanning FTIR imaging system that can image more than 16,000 spectra per second was available. The system, however, provided low signal to noise ratio (SNR) data. In increasing the SNR of data acquired, there are typically hardware or experimental approaches. It is prohibitively expensive to procure new hardware. Hence, typically, the approach has been to increase SNR by averaging successively acquired images. The benefits in SNR are  $\sqrt{n}$ , where  $n$  is the numbers of averaged spectral data cubes. Hence, we focused next on developing post-processing methods, as detailed next.

**Goal:** Develop a route to mathematically transform data to eliminate noise and yield high quality data. A custom algorithm will be developed in which the covariance matrix is employed to first perform a factor analysis equivalent operation followed by image separation from noise and re-transformation. Software to automatically correct data will be available. (Months 2-6)

**Activities:** The methodology was developed and is demonstrated to show a 50-fold improvement in SNR. Results are reported in publication to Journal of Chemometrics (submitted) and were presented at 2 conferences.

The first and simplest approach to higher fidelity imaging required co-adding a large number of array detector snapshots of the same scene, resulted in long dwell times of the mirror at every optical retardation<sup>8</sup>. We operated the interferometer in step-scan mode and wrote custom software to analyze the data. The advantages of this frame co-addition process were limited due to the noise characteristics of the detector. Hence, an optimal combination of frame co-addition and repeated scanning was implemented, as previously proposed<sup>9</sup>. Though these methods make the best use of the available hardware, they unfortunately, require large increases in data acquisition time as the SNR reduction scales less than linearly with the acquisition time. In order to obtain high SNR data using acquisition-side approaches, the trade-off with respect to time is unavoidable. Such a trade-off limits the possible applications of FT-IR imaging as a routine microscopic analysis tool in prostate cancer.

For a finite data acquisition time, other schemes to extract low noise information are available<sup>10</sup> but these methods neglect the image as a whole and result in loss of image fidelity. While we implemented these schemes here, it was clear that structural fidelity of the tissue image was being affected. Hence, we turned our attention to another alternative to hardware improvement or co-addition schemes for high fidelity imaging. This approach is the use of mathematical noise reduction techniques. For example, a procedure based on the Minimum Noise Fraction (MNF) transform was adopted from the satellite and airborne imaging community<sup>11</sup>. With rapid development of powerful computers and increased storage capacities, using computation to enhance instrument performance is becoming an attractive option. Using chemometric methods to enhance acquired FT-IR imaging data has been a relatively recent development. A convenient approach is to use an Eigenvalue decomposition of the data using a forward transform, e.g. PCA. After selecting eigenimages with sufficient SNR, the selected data are inverse transformed to yield the entire dataset with lower noise content. This approach was used<sup>12</sup> to examine phase compositions by enhancing contrast between different regions. PCA reorders data in decreasing order of variance.

A similar technique called MNF transform was proposed<sup>13</sup> to re-order image data in decreasing order of SNR. A modified version<sup>14</sup> of this transform has been shown to improve image fidelity and achieve better noise reduction than PCA, for example. Mathematical transform techniques for noise reduction generally utilize the fact that noise is uncorrelated whereas spectra (signals) have a fairly high degree of correlation. In the transform domain, the signal is primarily restricted to a few factors whereas the noise is spread across all factors. We use the term 'factors' to refer to images of eigenvalues in the transform domain. Noise reduction can be achieved by retaining factors corresponding to high signal content, removing factors predominantly

corresponding to noise and computing the inverse transform. Identifying factors corresponding to high signal content is an important step in the noise reduction process.

The identification of factors to include is invariably a manual process and is the key impediment to routine application of these methods for noise reduction. First, the manual selection will vary from practitioner to practitioner, leading to variance in the results obtained from the same data set. The scientific conclusions or confidence in results, hence, may vary in an unpredictable manner. Second, the need to examine every eigenvalue image (or, at least, a large set of images) is time-consuming. The decision to exclude or include images with questionable content is especially difficult and requires significant time as some quantitative guidance is often used. For example, we have used comparisons of values from sample and sample-less regions. These two factors are a key barrier in the use of these post-processing techniques for enhancing IR imaging data. There are many dimensional reduction and noise reduction schemes proposed<sup>15,16</sup> to address this issue. Many of these methods<sup>15,17,18</sup> choose all factors before a certain cut off ( $k$ ) determined based on predefined criteria. However, the assumption that all of the first  $k$  factors are important is questionable. The MNF approach was specifically developed to overcome the observation that the first  $k$  factors in PCA were not always optimal. Other methods<sup>16,19</sup> can be computationally expensive or do not utilize some of the features of the data in factors.

We recognized that a major limitation of these methods is that they do not explicitly account for the spatial and spectral information in the data. For example, PCA separates features in the spatial domain by accounting for variance in the scene. The variance may arise from the data, sensor or may be an artifact. Similarly, the signal in the re-ordering of MNF factors is assumed to be features in the image but could come from factors other than the sample of interest. For example, Figure 1 shows the 4<sup>th</sup>, 8<sup>th</sup>, 12<sup>th</sup> and 19<sup>th</sup> MNF factor for FT-IR data from a breast tissue sample. The 4<sup>th</sup> MNF factor shows interesting tissue structural features. Although the 8<sup>th</sup> factor has higher SNR compared to the 12<sup>th</sup> or 19<sup>th</sup> factor, the 12<sup>th</sup> and 19<sup>th</sup> factors contain relatively more features of interest. We would include the 12<sup>th</sup> and 19<sup>th</sup> factors but not the 8<sup>th</sup> in a noise reduction scheme involving MNF transform. The 8<sup>th</sup> factor likely arises from illumination or water vapor differences and not from the sample itself.

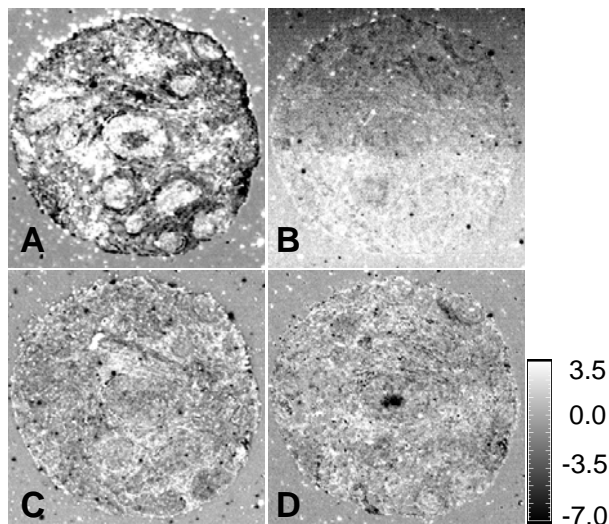


**Figure 1 (A) 4<sup>th</sup> MNF Factor (Tissue structural features visible) (B) 8<sup>th</sup> MNF factor (C) 12<sup>th</sup> MNF factor (D) 19<sup>th</sup> MNF factor. The 8<sup>th</sup> factor has less structural features compared to 12<sup>th</sup> or 19<sup>th</sup> factor.**

Hence, we proposed a factor selection algorithm that selects factors based on structural features in a quantitative manner. The MNF transform of our dataset is computed to obtain factor images corresponding to decreasing SNR values. We are interested in retaining only those factor images that have visible structural features. These features include boundaries of tissue samples, ducts and boundaries between different structural units. An important observation here is that images having distinct features have well defined edges. Edges capture these structural features and form the basis of our factor selection scheme. Several methods for edge detection<sup>20</sup> based on different filters and different thresholding schemes have been proposed and studied. Three well known edge detection techniques (Sobel, Roberts, and Canny) were used and Canny's method<sup>21</sup> was found to be the most effective one for our application. The result of edge detection is a binary image that we will call an 'edge map'. A typical edge map is shown in figure 2. It must be noted that the presence of impulsive noise hinders edge detection. A median filter is used to mitigate the effect of such impulsive noise. The choice of size of the median filter is a compromise between the size of structural features in the image and the size of noise clusters that need to be removed. Using a large median filter would be effective in removing large clusters of noise but could also result in loss of features, especially those that are smaller than the size of the median filter. Median filters of sizes between 7x7 and 13x13 were found to be effective in our application. It may be noted that the edge map in Figure 2 has been obtained after median filtering with a size 9x9 filter.

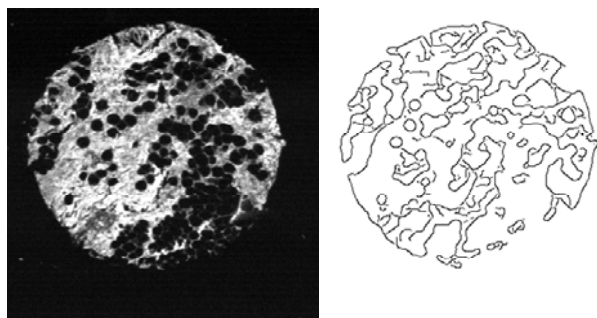


**Figure 2. Left:** Typical 'ideal' image (**I**) **Right:** corresponding edge map (**E<sub>I</sub>**)

The next step in factor selection is to choose an 'ideal', high SNR image (**I**) that has all the structural features of interest. The edge map of **I** and edge maps of factors images are compared to decide whether or not a factor is significant. Since the first MNF factor corresponds to the highest SNR, it could be used as our 'ideal' image **I**. However, it may be possible to choose a better image than the first factor in terms of structure if we have some prior knowledge about the sample, for example, information about its spectral characteristics. For many biological tissues, the wavenumber region between  $1050\text{cm}^{-1}$  to  $1810\text{cm}^{-1}$  and from  $2165\text{cm}^{-1}$  to  $3050\text{cm}^{-1}$  is known to have chemical significance. The ideal image **I** could be computed by first calculating the second derivative of spectra in these ranges using a Savitzky-Golay algorithm<sup>22</sup>. The sum of the absolute values of the second derivative data is indicative of the chemical composition of the

tissue. While we have used specific knowledge regarding tissue in this case, the finger print region of the IR spectrum is likely universally applicable for this procedure. The Savitzky-Golay filter reduces noise while preserving peak heights and widths, and the summation helps improve overall SNR by averaging noise. This gives us a high SNR  $\mathbf{I}$  (figure 2) that captures features from important spectral bands. An alternative is to simply calculate the Gram-Schmidt intensity of the interferogram of the sample<sup>23</sup>. Hence, the image would retain the structural and biochemical contributions from all functional groups and scattering interfaces. Yet another approach could be to use the bright field optical microscopy image. The optical image may not contain sufficient contrast, have differences observed in the IR image or may experience a mismatch in resolution. Hence, we would suggest the use of the IR “bright field” equivalent, which is simply the height of the centerburst. Since a background is always collected for absorbance data. The ceterburst height in the sample data set could be corrected for illumination differences using background data.

Having chosen an ‘ideal’ image  $\mathbf{I}$ , its edge map  $\mathbf{E}_I$  is computed after median filtering. Next, each MNF factor image is median filtered and edge maps  $\mathbf{E}_j$ ,  $j=0,1,\dots,N-1$  are found. In practice, the number of significant MNF factors for our data was much smaller (<60) than the number of spectral bands (~1640) and it would be prudent to compute only the first few (~60) factors so as to save computation time. The significant factors could be chosen from this subset of factor images. Next, the root mean square error (RMSE) between  $\mathbf{E}_I$  and  $\mathbf{E}_j$ ,  $j=0,\dots,N-1$  is computed. A typical plot of RMSE vs factor number is shown in Figure 3. RMSE here is an estimate of the closeness of a factor image to the ideal image  $\mathbf{I}$  in terms of structural features. The plot reveals that factors corresponding to higher eigen values may not necessarily have more significant features. Significant factors are those which have lower RMSE. The RMSE values are sorted in ascending order while keeping track of the indices (corresponding to MNF factor numbers).

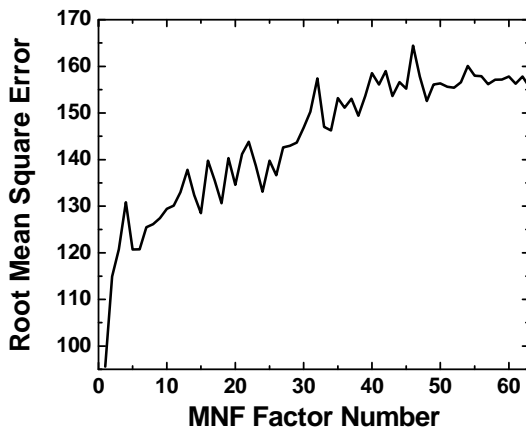


**Figure 3. Typical error plot before sorting RMSE**

A typical RMSE plot after sorting is shown in

**Figure 4.** A characteristic of this curve is that it increases rapidly in the beginning and transitions to a plateau later. Comparing edge maps and factor images corresponding to various points on the curve, we observe that the initial steep region corresponds to factors with significant features and the later plateau region of the curve corresponds to noise. Therefore, a good cut-off point for factor selection would be a point on the curve just before the onset of the plateau. By choosing all factors corresponding to RMSE values less than that at the cut-off point, we select only those

factors with significant features. The derivative of the curve in the plateau region is zero and this could be utilized in finding the cut off point. However, in order to mitigate the effect of local variation, a moving average filter is first used to smooth the curve before finding the discrete derivative. The cut-off is chosen to be the point after which the derivative does not rise more than  $\mu+3\sigma$  where  $\mu$  and  $\sigma$  correspond to the mean and standard deviation of the derivative of flat region of the curve.

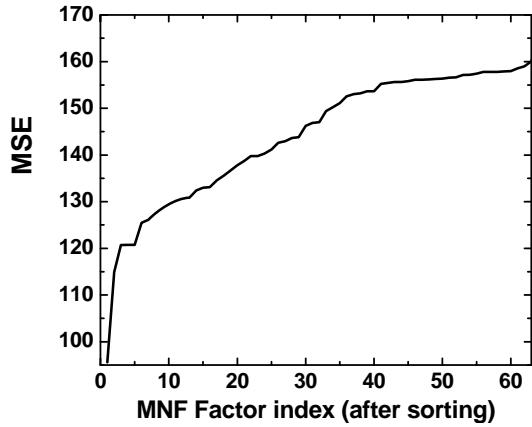


**Figure 4. Typical error plot after sorting RMSE and reordering MNF factors in terms of increasing RMSE**

Finally, the MNF factors corresponding to the chosen indices are rearranged in the order of decreasing correspondence with the reference image and only the objectively selected factors are used in the inverse MNF transform. Computing the MNF transform, selecting factors based on edge maps and computing the inverse MNF using these factors gives a complete automated noise reduction algorithm that does not require human input. There are choices that can be made while setting up the protocol, for example, in choice of the reference image, that are under operator control. Once the protocol is finalized, however, the process is entirely automated and can be high throughput. Thus, the criteria of both objectivity and automation for noise reduction are addressed.

Although we illustrate the utility of the proposed algorithm for tissue FT-IR data, the technique is more general and can be applied to any other data in which structures in images are well described by edges. We could also use the proposed factor selection algorithm with other transform techniques like PCA for example. A generalization of the MNF transform has been proposed by<sup>24</sup>. However, we did not observe the kind of distortion described in [24] in our data and therefore did not find the need to use the generalized MNF. We demonstrate the efficacy of this automated SNR enhancement by applying the process to breast tissue data. The effects of SNR are quantitatively measured by the accuracy of classifying tissue.

Tissue classification accuracy is related to SNR of the data. In Figure 5, we report the qualitative evaluation of classified images from example tissue from both as-acquired FT-IR imaging data (A) and from the data with added noise (B-D), as discussed previously. There is a significant decrease in classification accuracy when the noise is greater than 0.01a.u.. Image sets with higher noise produce classified images with regions of distinguishable classes (stroma and epithelium). Increasing noise produces increasingly noisy images until pixels in the high noise image become

almost randomly assigned to a class (D). This evaluation is confirmed in the plot of classification accuracy vs added noise (E), in which the accuracy value does not change initially but decreases with the addition of noise. The accuracy measure is the area under the receiver operating characteristic (ROC) curve (AUC). AUC values finally fall to about 0.5, which is equivalent to random guessing and does not provide any useful classification information. These results also give us the order of magnitude estimate of acceptable noise for reasonable classification accuracy. The dependence of prostate classification accuracy on SNR is detailed in the next section for a more complete model.

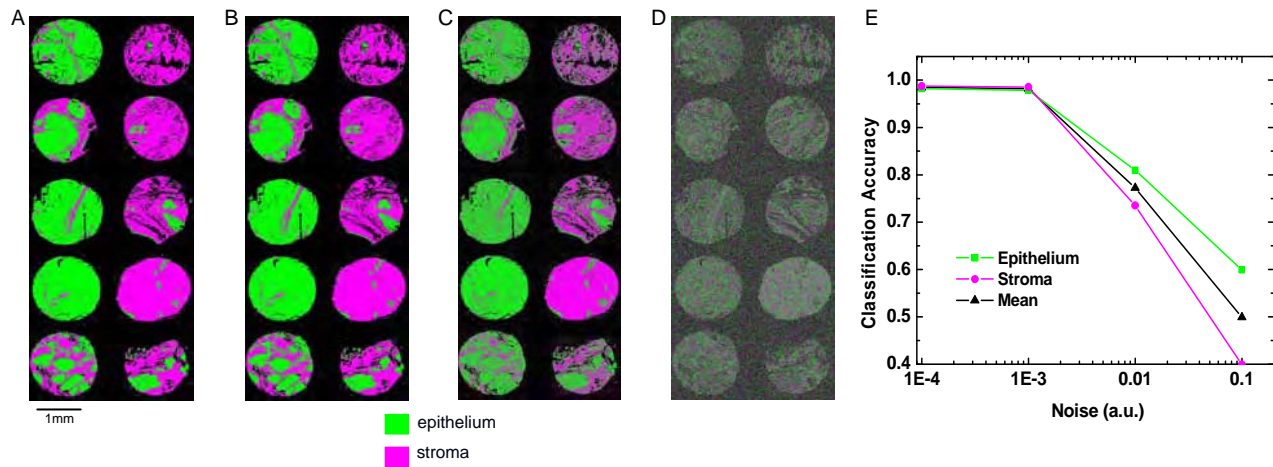


**Figure 5. Effect of noise on FT-IR image classification.** Classified images correspond to (A) as-acquired data, (B) data with added Gaussian noise of ~ 0.001a.u., (C) 0.01a.u., and (D) 0.1a.u. (E) Classification accuracy is provided as a function of noise for two classes of breast tissue.

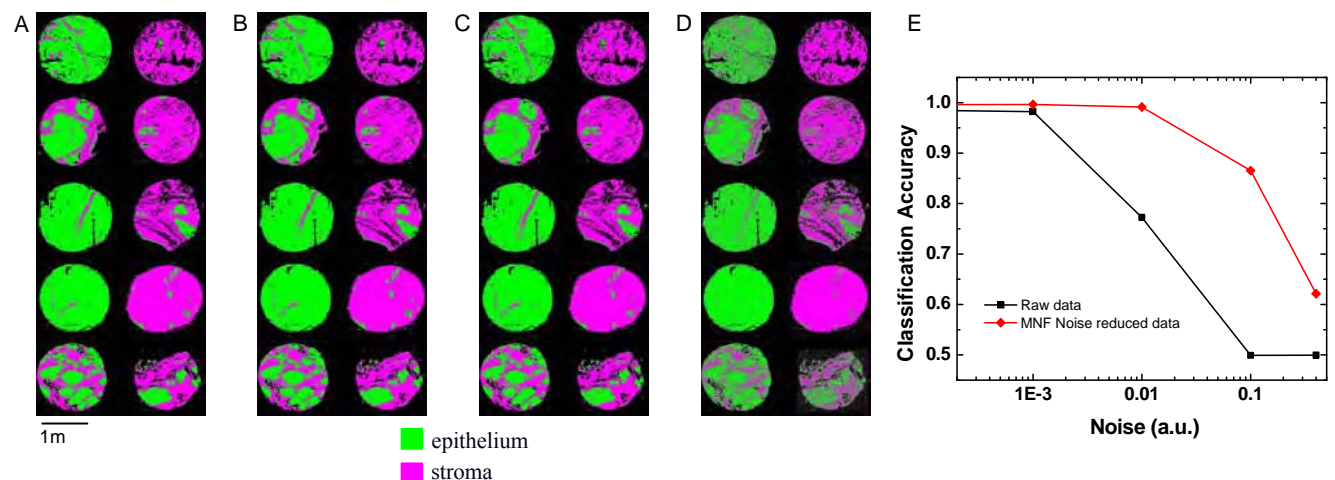


**Figure 6. Image classification improvement upon using the noise reduction algorithm.** Classified images correspond to noise reduced (A) raw data, (B) 0.001 noise (C) 0.01 noise (D) 0.1 noise (E) Comparing classification before and after noise reduction.

The impact of noise reduction on classification is demonstrated in Fig. 6. The proposed noise reduction scheme is used on data shown in figure 5. Classified images are displayed for each noise-reduced case (A-D) and the classification accuracy values for the noise reduced images are compared with the classification accuracy values for original images (E). Examination of classified images and classification accuracy values indicates that our noise reduction scheme improves classifier performance in each case. For as-acquired data and data with noise  $\sim 0.001$ a.u. added, noise reduction does not appear to significantly impact classification since the classification accuracy is already close to 1. On the other hand, noise reduction significantly improves classification from FT-IR spectroscopic imaging data with higher noise levels. Hence, a potential route to faster data acquisition for histopathology, without the need to modify hardware or change any experimental configuration, can be proposed based on post-processing noise reduction. Instead of needing  $\sim 300$  hrs (12 days) to scan a 1 cm x 1 cm area, the proposed approach will allow the same in a few hours.

In summary, a noise reduction algorithm with a factor selection scheme based on object structural features has been proposed. An order of magnitude reduction in noise could be achieved using this algorithm. When noise reduced data is subject to further processing, for example for tissue classification, there is a substantial improvement in classification performance at higher noise levels. The improvement translates directly time required for data collection, while preserving the accuracy of classification. It must be noted that the gain here is through post-acquisition computational techniques and does not involve changes in instrumentation hardware or data acquisition schemes. Hence, it is easy to implement and inexpensive to deploy routinely. It is anticipated that the automated nature of the proposed approach will allow it to become routinely applied to enhance data quality and the quality of scientific information derived. For translating prostate tissue histopathology using IR to clinical studies, this development is critical. Further, it allows us to image tissues in large numbers as proposed next.

**Goal:** Data acquisition and treatment protocol will be optimized and feedback loop implemented. Image sets will be acquired at low averaging and extensive averaging conditions to verify performance and optimize algorithm. A validated protocol for collecting data will be available. (Months 5-7)

**Activities:** Data were acquired and experimental conditions were optimized to help determine the operating points for prostate histology. Briefly, the spectral resolution was not found to be important unless coarse resolution was obtained. SNR was found to be crucial and a plot of the SNR versus the classification accuracy yielded the optimal operating point. Results are summarized in a peer-reviewed manuscript<sup>25</sup> and the methodology is described in a review paper. Results were presented at three different meetings. A single button operation is implemented in our software that now pre-processes data and adjusts for appropriate SNR. A second step can then classify the resulting data into histologically correct classes. The work is described in detail next.

**Effect of Signal to Noise Ratio:** There are two issues: what is the “best” SNR to formulate algorithms and second, provided an algorithm, what is the least SNR that would provide adequate classification. Only the latter issue is examined here. As with conventional FTIR spectrometers, imaging spectrometers obey the trading rules of IR spectroscopy. Hence, if an  $n$ -

fold reduction in SNR provides the same results, data acquisition will be  $n^2$ -fold faster. Thus, in addition to an interesting fundamental behavior of the classifier, the role of SNR has a direct bearing on the speed at which data is acquired.

We examined classification accuracy as a function of average spectral noise. To strictly examine the effect of noise, data must be acquired at different co-added spectral numbers. The time required for imaging an array multiple times, however, is prohibitive. Hence, we computationally added random, Gaussian noise to the original spectral data. Peak-to-peak and root mean square (rms) noise were measured in the 1950-2150  $\text{cm}^{-1}$  region adjacent to the amide I peak.<sup>26</sup> Representative single pixel spectra from the data sets are shown, as a function of noise, in Figure 7(a). We additionally plotted the observed noise levels against the added noise to verify linearity (plot not shown). The linear relationship conforms to the expected result and provides a scaling factor to express the equivalent reduction in data acquisition time (co-addition) that would be realized at that noise level. For example, the addition of 0.005 a.u. of noise raises the peak-to-peak noise from 0.0013 to 0.015 a.u., corresponding to a decrease in data acquisition time by a factor of  $\sim 100$  for this data set. In addition to increasing noise, we employed an MNF-transform<sup>27,28</sup> based algorithm to mathematically eliminate noise. The observed peak-to-peak noise was 0.00017 a.u. corresponding to an increase in data acquisition time by a factor greater than  $\sim 100$ . Hence, the data examined span about 5 orders in magnitude of collection time.

The average height of the Amide I peak was 0.42 a.u. in all cases, providing a SNR of 2500 (MNF-corrected data) to 1.5 for the data sets. Accuracy as a function of the noise level is shown in Figure 7(b). While the x-error bars indicate the standard deviation of noise levels in pixels, the y-error bars indicate the standard deviation in AUC values of all ten classes. As a general rule, the classification improves with lower noise levels. We first note that the classification does not become perfect for any noise level and there is a significantly diminishing return in increasing the SNR beyond a level. At the other end, the ability to distinguish classes is entirely lost at levels of  $\sim 0.1$ . Performance across multiple data sets observed using our prediction model indicates that the increases demonstrated at noise levels lower than  $\sim 0.003$  a.u. are within the variance. Hence, there is little benefit to decreasing the noise levels below  $\sim 0.003$  a.u. for this data set, or to increasing the SNR beyond  $\sim 150$ . It must be emphasized that the model, prediction algorithm and discriminant function are intimately linked in a non-linear manner. While this makes it impossible to predict the behavior generally of all classification approaches, this simple exercise may be conducted to determine the optimal data acquisition parameters. For our selected metrics and model, it appears that the data acquisition time can be decreased by a factor of  $\sim 3$  without significant degradation in accuracy.

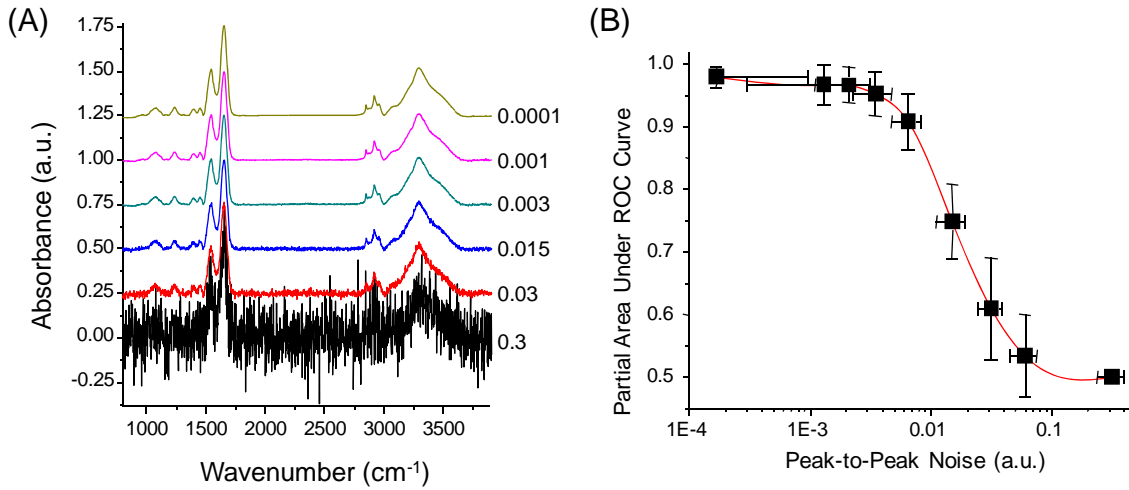


**Figure 7. (a) Noise in the data set as a function of added random noise. (b) Effect of spectral noise on the accuracy of classification as measured by AUC values.**

*Spectral Resolution:* We next examined the effect of spectral resolution on the results that would be obtained using the developed algorithm. As in the previous section, the data were not re-acquired but were downsampled from acquired data using a neighbor binning procedure. Spectra from the same epithelial class pixel, at different resolutions (Figure 8(a)), demonstrate the effect of downsampling on feature definition. Figure 8(b) demonstrates, first, that the peak-to-peak noise levels over the region remain the same with spectral resolution. As previously observed, noise is an important control in comparing spectra; the peak-to-peak noise over the same number of data points was preserved by neighbor binning. In practice, the constant throughput spectrometer would provide a SNR (or noise level, in this case) that decreases linearly with resolution. Since most array detectors can be operated with higher integration times, it is fair to assume that the time advantage in decreasing resolution would be linear. Second, the performance of the classifier is very nearly the same for finer spectral resolutions and degrades only significantly for  $32 \text{ cm}^{-1}$ . While the results may appear to be surprising, a closer analysis of the basis of the algorithms provides insight into the trends.

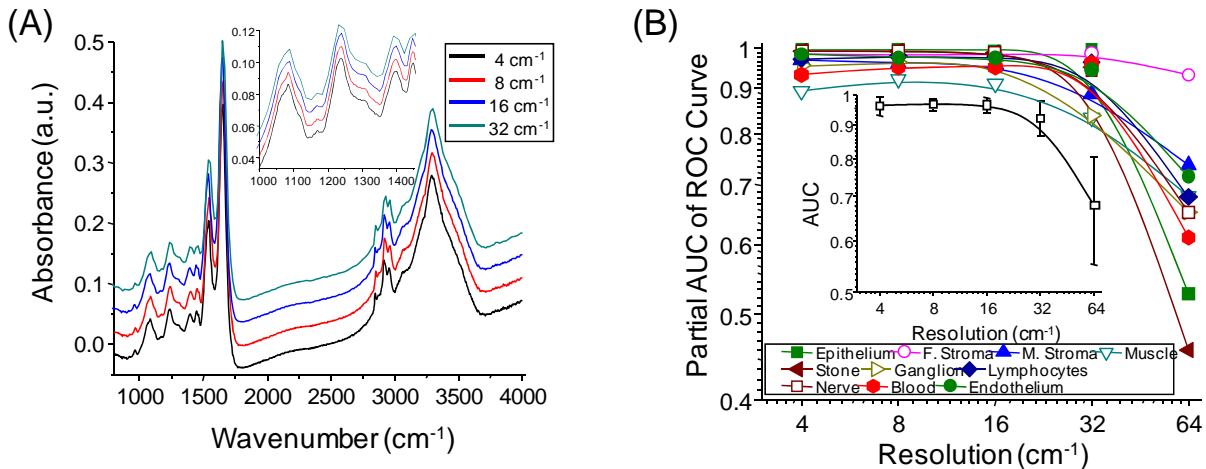


**Figure 8.(a)** Spectra obtained by downsampling acquired data to different resolutions using a neighbor binning procedure. The inset demonstrates the effect of resolution on narrower features in the spectrum. **(b)** AUC values for each class and average AUC values as a function of spectral resolution demonstrate a decrease only for coarse spectral resolution.

The classifier is based on absorbance and center of gravity measures of the peaks. It is well-established that absorbance is measured accurately, provided that the FWHH of the peak is not significantly smaller than the resolution. The Ramsay resolution parameter,  $\sigma$ , is a useful measure that was originally developed for monochromators but has been shown to be applicable to FTIR spectrometers as well.<sup>29</sup> While most bands are broad and peak absorbance lower than  $\sim 0.7$ , absorbance values are not expected to be adversely impacted from the measurement process. With decreasing resolution, however, broadening within complex peaks shapes may lead to observed changes in the apparent absorption at a specific wavenumber. The change itself may not have a significant influence on the classifier performance as it depends on several such metrics. A second type of metric calculates the area under the curve. This is not expected to be impacted significantly for most peaks. The third type of metric we have used is the center of gravity of a spectral region. While spectral analyses ordinarily attempt to locate the peak position and use it as a metric, we chose the center of gravity for its sensitivity to both position and asymmetrical shape changes in complex spectral envelopes observed in biological samples. Since the classifier is based on center of gravity of a feature and not on the wavenumber of the peak maximum, it is a very robust measure that is relatively unaffected by spectral resolution or noise.

#### Generalization of developed algorithms to instruments and practical approaches

The characterization of classification with regard to spectrometer performance (SNR) and spectral resolution provides information to optimize parameters on one spectrometer. It is unclear, however, if the calibration would transfer to another spectrometer. We contend that the potential for a successful transfer is high as the classification process is relatively insensitive to resolution, implying that it would only be weakly sensitive to apodization or to small inaccuracies in wavelength scale. Similarly, if the SNR of acquired data is used as control, perturbations due to fixed pattern noise in focal plane array detectors or the different use of electronic filters by different manufacturers is likely to be insignificant in classifying tissue

correctly. Various instrument manufacturers also set the nominal optical resolution differently in their instruments. The issue of spatial resolution, of course, is more complex. Nevertheless, any resolution setting around the wavelength limited case will likely provide consistent results. To our knowledge, there has been no comparison yet of classifier performance across mid-IR FTIR imaging spectrometers using algorithms developed on one specific instrument. The developed protocol provides for such a framework and detailed results are awaited from on-going work.<sup>30</sup> The analysis of spectral SNR and resolution, however, are critical first steps in ensuring that the results from different instruments can be compared. The optimization of detection (as demonstrated here) is accomplished and we image tissues at the optimal parameters with sufficient SNR.

**Goal:** Data will be acquired from samples identified in Task 2, sub-task a. 4 cm<sup>-1</sup> spectral resolution data, imaging ~6 micrometer of sample per pixel will be acquired with a signal to noise ratio of greater than 1000:1. At least 375 samples will be imaged to provide an estimated 40 million spectra. Data will continuously be available for analysis in this period. (Months 8-18)

**Activities:** Over 4 million spectra have been acquired from approx. 460 samples. Data handling and analysis is on-going. The data were acquired using a tissue microarray with no restrictions on age or prior PSA reading. The samples organized into a tissue microarray format.

## **Task 2. Analyze spectroscopic imaging data for biochemical markers of tumor and develop numerical algorithms for grading cancer**

**Goal:** Study is anticipated to be exempt and appropriate permissions will be obtained from the IRBs involved. (Month 1)

**Activities:** Appropriate permissions were obtained and the work was initiated.

**Goal:** Identify samples to be imaged by examining stained slides with collaborators. Samples spanning the range of pathologic conditions and outcome will be identified for use in the study. A compilation of anonymized cases and samples will be available. (Months 1-3)

**Activities:** A cohort of almost 400 samples has been identified and imaging has begun. The samples are all archival tissue samples from which tissue microarrays have been constructed. Thus, we are able to access both a representative and a diverse group of patients. All patients have undergone radical prostatectomy. The samples themselves are formalin-fixed and paraffin embedded. The samples were obtained by microtoming a thin slice of tissue and depositing it on a substrate. We used two substrates, a BaF2 one for optimal IR transmission and a reflective slide for reflective IR imaging. The samples were subsequently de-paraffinized using gentle washing in hexane for 24 hours and used as is.

**Goal:** Obtain unstained samples to be imaged and define regions for calibration and validation. A set of samples for training and for validation will be available. (Months 4-7)

**Activities:** A cohort of almost 400 samples has been identified and imaging has been begun. Using the optimized version of the algorithms in task 1 was used to image tissue and classify histology. The results are shown in Figure 9. This is a subset of a total of 460 patients. The lower yield of 400 is due to damage and destruction during processing of some tissue samples.

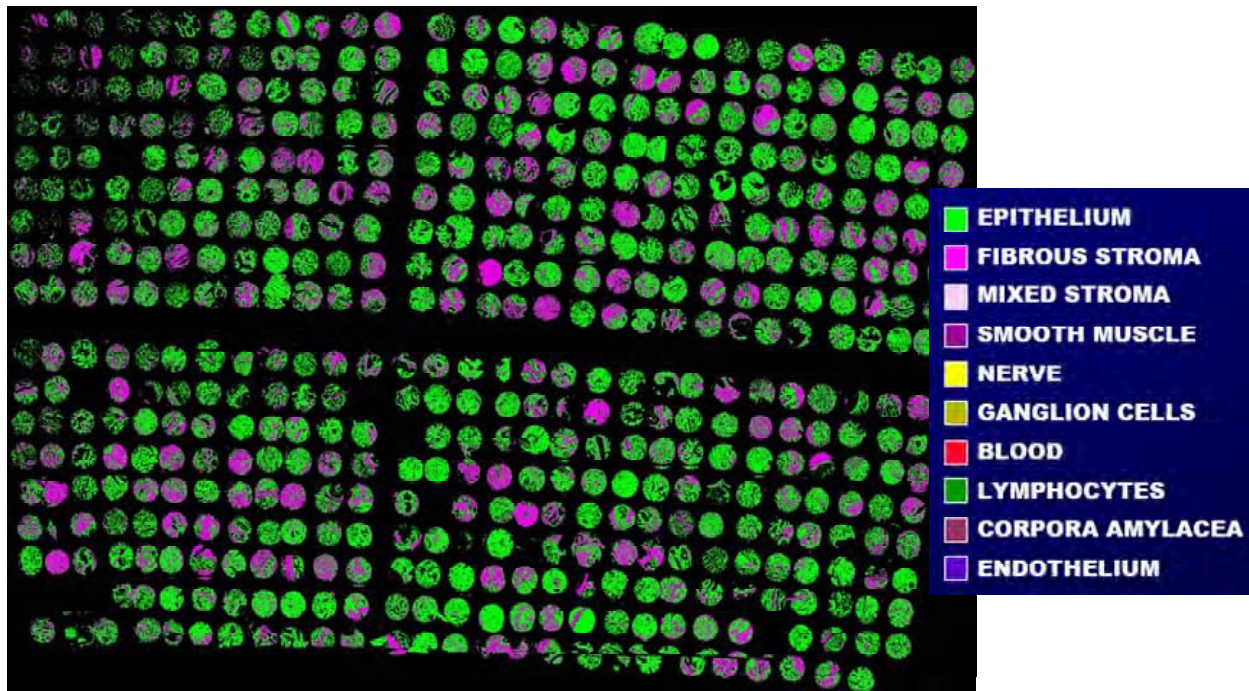


**Figure 9. Optimized classification of a tissue microarray incorporating normal and at least 400 lesions of varying grades.**

The availability of this data is augmented by the availability of clinical data associated with the samples. All patients underwent radical prostatectomy (RP) and have varying outcomes over a period of 15 years. Simple Bayesian methods, as used for classification of previous tissue samples, could not be used to predict outcome in this case. The primary challenge is that there are no specific peaks or markers in the spectrum that correlate with outcome. It is also not easy to analyse 2000 data points in the spectrum to correlate with outcome. Hence, we turned to methods that will help extract the key spectral quantities that can be used to predict outcome. These methods are based on genetic algorithms and are described next.

**Goal:** Perform histologic identification on prostate samples and validate. We will apply previously developed protocols and carefully verify that accurate histologic segmentation is achieved using receiver operating characteristic (ROC) curves and confusion matrices. Histological images will be available for malignancy analysis. (Months 8-10)

**Activities:** A number of other data dimensionality reduction strategies may be used but make the dependence of classification on spectral parameters rather opaque, for example, neural networks. Hence, a new classification procedure based on Genetic Algorithms was developed and shown to be very effective.<sup>31</sup> The new method's advantage over previous methods is the ability to explicitly choose spectral indices that are correlated with histopathology and to explicitly see which indices influence classification accuracy. The method was tested on histologic segmentation and is now being adapted for cancer segmentation. A major challenge in implementing this method was the large data set (typically 100 GB) that needed to be panned for spectral indices and the large possible space of spectral index combinations that provides the optimal classification.

Hence we undertook development to demonstrate how genetics-based machine learning (GBML) tools can achieve such a goal. Interpretability of the learned models and efficient processing of very large data sets have lead us to rule-based models—easy to interpret—and genetics-based machine learning—*inherent* massively parallel methods with the required scalability properties to address very large data sets. We present the method and the efficiency enhancement techniques proposed to address automated tissues classification. When pushed beyond the relatively small problems traditionally used to test such methods, a need for efficient and scalable implementations becomes a key research topic that needs to be addressed. This is a major challenge as canned analysis programs do not provide the capability to handle such large sets efficiently. Hence, we designed the technique described next with such constraints in mind. A modified version of an incremental genetics-based rule learner that exploits massive parallelisms—via the message passing interface (MPI)—and efficient rule-matching using hardware-oriented operations. We name this system NAX and compared the implementation first to traditional and genetics-based machine learning techniques on an array of publicly available data sets. We report below the major points of development and initial results achieved using NAX when classifying prostate tissue.

Another important issue in real-world problems is the histologic class distribution. For example, a lot of epithelial cells are encountered and significantly fewer endothelial cells may be encountered. Usually most real problems have a clear class imbalance. Recently, GBML techniques were used by other groups to successfully learn and maintain proper descriptions for those minority classes. If not designed properly, descriptions of majority classes will tend to govern the learned models, starving the description of minority classes. Prostate tissue classification is a clear example of extreme class imbalance. Figure 10 presents the tissue type class distribution. The smaller tissue type (endothelial cells) has 64 records, where as the larger classes have several tens of thousands records. Hence, the developed approaches must account for class size variation. This is a major challenge in any classification approach and is especially relevant here as endothelial cells provide clues to microvessel density (MVD). MVD is a critical parameter shown to have relevance in the growth of cancers. We propose to use it later as an index in classifying poor from good outcome tumors. Hence, it was crucial to examine the results from our GBML methods.

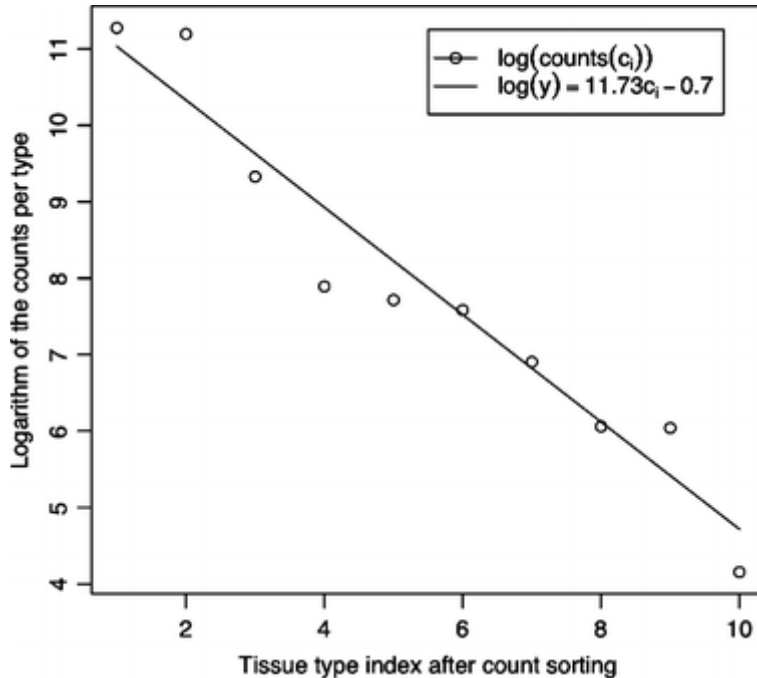


**Figure 10. Histologic class distribution in prostate tissue.** Once the classes are reordered according to their frequency in the data set, we can easily appreciate the extreme imbalance—the smaller tissue type has 64 records, where as the larger classes have several tens of thousands records

We describe the steps we took to design a GBML method (**HAX**) able to deal with very large data sets with class imbalance: **HAX** evolves, one at a time, maximally general and maximally accurate rules. Then, the covered instance are removed and another maximally general and maximally general rule is evolved and added to the previously stored one forming a decision list. This process continues until no uncovered instances are left—this process is also referred as the sequential covering procedure. Llorà et al. showed that maximally general and maximally accurate rules could also be evolved using Pittsburgh-style Learning Classifier Systems. Later, Llorà et al. showed that competent genetic algorithms evolve such rules quickly, reliably, and accurately. Hence, we explored next efficient implementation techniques to deal with very large data sets, the impact of class imbalance, and the **HAX** algorithm proposed.

As introduced earlier, when dealing with very large data sets, and regardless of the flavor of the GBML technique used, we may spend up to 98% of the computational cycles trying to match rules to the original data set. Each solution evaluation is independent of each other and, hence, it can be computed in parallel. Moreover, even the matching nature of a rule—the representation we will use from now on—is highly parallel, since conditions require performing simultaneous checks against different attributes per record. Thus, efficient implementation can take advantage of parallelizing both elements. Recently, multimedia and scientific applications have pushed CPU manufacturers to include support for vector instructions again in their processors. Both applications areas require heavy calculations based on vector arithmetic. Simple vector operations such as *add* or *product* are repeated over and over. During 1980s and 1990s supercomputers, such as Cray machines, were able to issue hardware instructions that enabled basic vector arithmetics. A more constrained scheme, however, has made its way into general-

purpose processors thanks to the push of multimedia and scientific applications. Main chip manufacturers—IBM, Intel, and AMD—have introduced vector instruction sets—AltiVec, SSE3, and 3DNow<sup>+</sup>—that allow vector operations over packs of 128 bits by hardware. We took advantage of these developments by focusing on a subset of instructions that are able to deal with floating point vectors. This subset of instructions manipulate groups of four floating-point numbers. These instructions are the basis of the fast rule matching mechanism proposed.

Using a knowledge representation based on rules allows us to inspect the learned model, gaining insight into the biological problem as well. All the attributes of the domain are real-value and the conditions of the rules need to be able to express conditions in a  $\mathbb{R}^n$  spaces. We use a similar rule encoding to the one proposed by Wilson previously — and widely used in the GBML community. Rules express the conjunction of tests across attributes. Each test may be defined in multiple flavors but, without loss of generality, we picked a simple interval based one. A simple example of an *if-then* rule, could be expressed as follows:

$$1.0 \leq a_0 \leq 2.3 \wedge \dots \wedge 10.0 \leq a_n \leq 23 \rightarrow c_1 \quad (1)$$

Where the condition is the conjunction of the different attribute tests and the outcome is the predicted class—a tissue type. We also allow a special condition— ***don't care***—which just always returns **true**, allowing condition generalization. The rule below illustrates an example of a generalized rule.

$$1.0 \leq a_0 \leq 2.3 \wedge -3.0 \leq a_3 \leq 2 \rightarrow c_1 \quad (2)$$

All attributes except  $a_0$  and  $a_3$  were marked as ***don't care***.

Each condition can be encoded using 2 floating-point numbers per condition, where  $\alpha_i$  contains the lower bound of the condition and  $\omega_i$  its upper bound. Thus, the condition  $\alpha_i \leq a_0 \leq \omega_i$  just requires to store the two floating-point numbers. For efficiency reasons we store them in two separate vectors, one containing the lower bounds and the other containing the upper bounds. The position in a vector indicates the attribute being tested. The ***don't care*** condition is simply encoded as  $\alpha_i > \omega_i$ ; and, hence, we do not need to store any extra information.

Matching a rule requires performing the individual condition tests before the final *and* operation can be computed. Vector instruction sets improve the performance of this process by performing four operations at once. Actually, this process may be regarded as four parallel running pipelines. The process can be further improved by stopping the matching process when one test fails—since that will turn the condition into false. Figure 11 presents a C implementation the proposed hardware-supported rule matching. The code assumes that the two vectors containing the upper and lower bounds are provided and records are stored in a two dimensional matrix. We found that exploiting the hardware available can speed between 3 and 3.5 times the matching process.

---

```

1. void match_seq_rule_set ( RuleSet * rs, InstanceSet is, int iDim, int iRows ) {
2.     int i,j,k,iCnt,iClsIdx,iGround,iPred;
3.     register int iMatchable;
4.     Instance ins;
5.
6.     iClsIdx = rs->iCorrectedDim;
7.     clean_fitness_rules_set(rs);
8.     for ( i=0 ; i<iRows ; i++ ) {
9.         ins = is[i];
10.        iPred=-1;
11.        for ( j=0 ; iPred== -1 && j<rs->iLen ; j++ ) {
12.            iMatchable = 1;
13.            for ( iCnt=0,k=j*(rs->iCorrectedDim+VBSIF) ;
14.                  iMatchable && k<j*(rs->iCorrectedDim+VBSIF)+rs->iDim ;
15.                  k++,iCnt++ ) {
16.                iMatchable = iMatchable &&
17.                      !( (rs->pfLB[k]<=rs->pfUB[k]) &&
18.                        ( ins[iCnt]<rs->pfLB[k] || ins[iCnt]>rs->pfUB[k]));
19.            }
20.            if ( iMatchable )
21.                iPred = rs->pfLB[j*(rs->iCorrectedDim+VBSIF)+rs->iCorrectedDim];
22.        }
23.        iPred = (iPred== -1)?rs->iClasses:iPred;
24.        iGround=(int)ins[iClsIdx];
25.        rs->pConfMat[iGround][iPred]++;
26.    }
27. }
```

**Figure 11.** sequential implementation of the rule matched process in C. A rule set is match against a data set. Lines 16, 17, and 18 implement the condition test for one attribute. The implementation also computes the confusion matrix that contains the ground truth versus predicted class

Since most of the time is spent on the evaluation of candidate rules when dealing with large data sets, our next goal was to find a parallelization model that could take advantage of this peculiarity. Due the quasi embarrassing parallel nature of the candidate rule evaluation, we designed a coarse-grain parallel model for distributing the evaluation load. The importance of the trade-off between computation time and time spent communicating needed to be evaluated but in this case was assumed to be fairly low given the intrinsic parallel nature of the data. When designing the parallel model, we focused on minimizing the communication cost. Usually, a feasible solution could be a master/slave one—the computation time is much larger than the communication time. However, GBML approaches tend to use rather large populations, forcing us to send rule sets to the evaluation slaves and collect the resulting fitness. These schemes also increment the sequential sections that cannot be parallelized, threatening the overall speedup of the parallel implementation as a result of Ambdhals law.

To minimize such communication cost, each processor runs an identical ~~HAX~~ algorithm. They are all seeded in the same manner, hence, performing the same genetic operations and only differing in the portion of the population being evaluated. Thus, the population is treated as collection of chunks where each processor evaluates its own assigned chunk, sharing the fitness of the individuals in its chunk with the rest of the processors. Fitness can be encapsulated and

broadcasted maximizing the occupation of the underlying packing frames used by the network infrastructure. Moreover, this approach also removes the need for sending the actual rules back and forth between processors—as a master/slave approach would require—thus, minimizing the communication to the bare minimum—the fitness. Figure 12 presents a conceptual scheme of the parallel architecture of **MAX**.

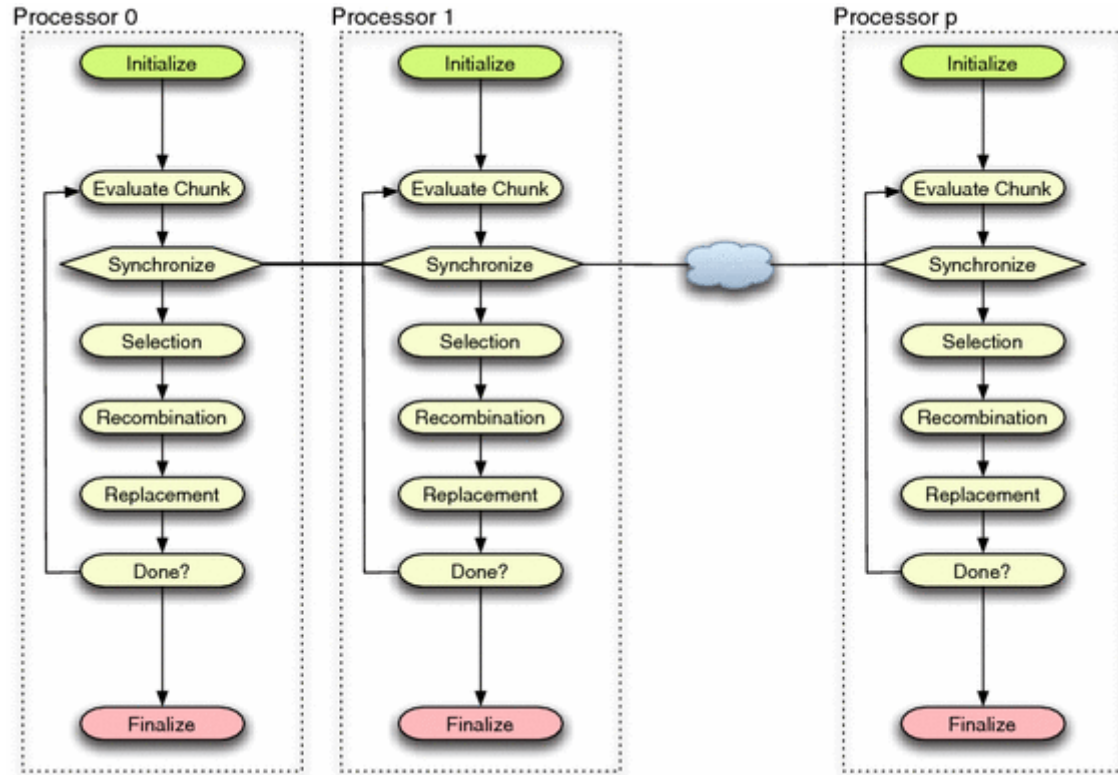


**Figure 12.** The parallel model implemented. Each processor is running the same identical **MAX** algorithm. They only differ in the portion of the population being evaluated. The population is treated as collection of chunks where each processor evaluates its own assigned chunks sharing the fitness of these individuals with the rest of the processors. This approach minimizes the communication cost

To implement the model presented above, we used C and a *message passing interface* (MPI)—we used the OpenMPI implementation. Figure 13 shows the code in charge of the parallel evaluation. Each processor computes which individuals are assigned to it. Then it computes the fitness and, finally, it just broadcast the computed fitness. The rest of the process is left untouched, and besides the cooperative evaluation, all the processors end generating the same evolutionary trace. The same program can be readily tweaked to parallelize the classification of tumor or grading in prostate tissue. The drawback in this method, however, is that the spatial structure in the tissue is not taken into account. This is an on-going concern and methods to address this need are being developed.

---

```

1. void evaluate_population ( Population * pp, InstanceSet is, int iDim, int iRows )
2. {
3.     int i;
4.
5.     /* Compute the fragments of this processor */
6.     int iFrag = pp->iLen/FCS_processes;
7.     int iInit = FCS_process_id*iFrag;
8.     int iLast = (FCS_process_id+1==FCS_processes)?
9.                 pp->iLen:
10.                (FCS_process_id+1)*iFrag;
11.    int iCnt = 0;
12.    int j,k,l;
13.
14.    /* Create the bucket for the broadcast */
15.    float faFit[2*iFrag];
16.    float faTmp[2*iFrag];
17.
18.    /* Evaluate the given chunk assigned to the processor */
19.    for ( i=iInit,iCnt=0 ; i<iLast ; i++,iCnt++ ) {
20.        match_rule_set(pp->prs[i],is,iDim,iRows );
21.        compute_raw_accuracy_fitness_rule_set(pp->prs[i]);
22.        faFit[iCnt] = pp->prs[i]->fFitness;
23.    }
24.
25.    /* Broadcast each of the chunks */
26.    for ( i=0 ; i<FCS_processes ; i++ ) {
27.        MPI_Bcast((i==FCS_process_id)?faFit:faTmp,iCnt,MPI_FLOAT,i,MPI_COMM_WORLD);
28.        if ( i!=FCS_process_id )
29.            for ( l=0,j=i*iFrag, k=(i+1)*iFrag ; j<k ; j++,l++ )
30.                pp->prs[j]->fFitness = faTmp[l];
31.    }
32. }

```

---

**Figure 13.** An implementation of the proposed parallel evaluation scheme using C and MPI. The piece of code presented below is the only one modified to provide such parallelization capabilities. Each processor computes which individuals are assigned to it (lines 6–10), then it computes the fitness (lines 10–23), and then it just broadcast the computed fitness (lines 26–31)

We conducted stratified 10-fold cross-validation experiments to measure the generalization capabilities of **HAX** for histologic classification of the prostate and compared results to previously published data. Since the problem was rather small—larger data set are being prepared to be run at the supercomputing facilities provided by the National Center for Supercomputing Applications—we ran the ten-fold cross-validation runs in a 3GHz dual core Pentium D computer with 4 GB of RAM. **HAX** took advantage of the hardware support to speedup the matching process and uses two MPI processes to parallelize the evaluation of the overall population. Each fold took about one hour to complete, with the entire classification lasting less than half a day. We conducted a simple test of adding a second computer with an identical configuration. The overall time for cross-validation was reduced to half. Rough estimates—which will better measured when larger experiments are conducted on NCSA super computers—show that the sequential portion is around 1:1000 for this small data set. Numbers get better as data set increases, which demonstrates that we will be able to process very large data sets and efficiently exploit larger numbers of processors.

We proposed another measure of effectiveness, namely how many records can be processed per second. Using a single processor with the hardware acceleration mechanisms built into **NAX**, and the evolved rule set formed by 1,028 rules, the average throughput was around 60,000 pixels per second. For the prostate tissue classification, it took less than three seconds to classify the entire data set. Once the rule set is learnt, the classification problem falls again into the category of parallel problems. Since no communication is needed, the speedup grows linearly with the number of processors added—with the proper rule set replication and data set chunking. Thus, with the dual core box used we were able to just double the throughput (120,000 pixels per second) by chunking the data set and use both processors.

The previous results show the benefits of hardware acceleration and parallelization, but **NAX** was also able to achieve very competitive classification accuracy in generalization, correctly classifying  $97.09 \pm 0.09$  of the records (pixels) during the stratified ten-fold cross-validation. Most of the mistakes by the rule set involve similar tissues with few training records available. This trend was also shown elsewhere and our approach does not provide any statistically significant improvement (only a marginal, not statistically significant, 0.7%) and provided large decision trees with more than 5,000 leaves—not to mention the lack of scalability when compared to **NAX**.

The rule set assembled by **NAX** represents an incremental assembling of maximally general and maximally accurate rules. Thus, we can compute how the accuracy of such ensemble improves as new rules are added. Figure 14 presents the overall accuracy as rules are added. It shows an interesting behavior for classifying prostate tissue. Using only 20 rules out of the 1,028 evolved ones, the overall accuracy is 90%, the incorrectly classified 1.3% pixels, and 8.7% were left unclassified. After inspecting the misclassified pixels most of them belongs to borders between tissues and mislabeling arises from the image discretization—one pixel containing different tissue types. Such results are relevant, not only for their accuracy, but also because of the insight they provide to the spectroscopist about the problem structure. In summary, the development and application of NAX is a major step in allowing us to handle large data sets and efficiently extract information from them. Hence, we are now convinced that we can handle very large data sets and the considerably more complex problem of determining cancer and grades using the implementation of NAX.

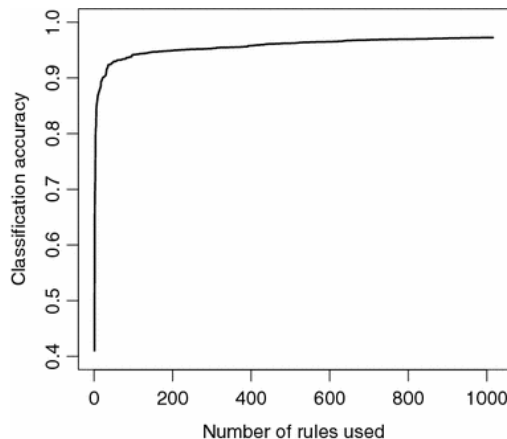


**Figure 14. The rule set as a decision list.** The figure presents the classification accuracy as we keep adding rules to the decision list. The first 20 initial rules are able to cover 91% of

**the records with a classification accuracy of 98.5–90% overall accuracy presented in the figure**

**Goal:** Develop algorithm for malignancy recognition. Spectral metrics will be identified in a manner similar to 2d (above) and reduced to those useful in identifying atypia. Models will be constructed and optimized using Genetic Algorithms operating on identified metrics. Models will be tested and validated using ROC curves with pathologist marking as the ground truth. A protocol for segmenting benign from atypical condition will be available. (Months 11-18)

**Activities:** Efforts are underway and preliminary tests of the algorithms are being undertaken. The initial results did not provide effective classification and we discovered that there is a strong sample to sample variability in the data. Hence, two avenues are being pursued. First, can we use a normal sample from the same patient to normalize for the effect of inter-person variance. Second, can there be a transformation that will scale spectra such that this variation is reduced. An effort is also underway to understand the relative variance offered by measurement noise, by person-to-person variance and by within sample variance. Quantification of these factors and their relative importance will help understand the source of variance leading to poor classification accuracy. For example, if the dominant variance is found to be measurement noise, we will re-acquire the data at higher SNR. If the variance is largely person-to-person, then a normalization strategy would have to be considered.

## **Key Research Accomplishments**

- Optimization of experimental parameters for spectroscopic imaging experiments. The optimization provides an understanding of the classification process and allows ~40 fold decrease in data acquisition time.
- Classification of prostate histology using Genetic Algorithms. The work explicitly identifies spectroscopic biomarkers needed to classify tissue correctly.
- A new method is introduced to reduce noise by nearly an order of magnitude. The method is based on post-processing to reduce non-correlated signals in images using the covariance of the recorded data. The method enables a ~7 fold higher signal to noise ratio, which translates into a 50-fold faster data acquisition rate.

## **Reportable Outcomes.....**

### ***Manuscripts***

#### *Peer reviewed manuscripts published*

1. R. Bhargava "Practical FTIR chemical imaging for cancer pathology" *Anal. Bioanal. Chem.*, **389**, 1155-1169 (2007)
2. X. Llora, A. Priya, R. Bhargava "Observer-Invariant Histopathology using Genetics-Based Machine Learning" *Nat. Computing*, In press (2007)
3. G. Srinivasan, R. Bhargava "Fourier transform infrared spectroscopic imaging: the emerging evolution from a microscopy tool to a cancer imaging modality" *Spectroscopy*, **22**, 40-51 (2007)

#### *Book Chapters*

1. R. Bhargava, I.W. Levin "Prostate Cancer Diagnosis by FTIR Imaging", M. Diem, P.R. Griffiths and J. Chalmers, eds (2008-anticipated)

### ***Published abstracts***

1. F. Keith, R.K. Reddy and R. Bhargava, "Practical protocols for ultrafast histopathology by Fourier transform infrared imaging," *SPIE Photonics West* (2008)
2. X. Llora, R.K. Reddy, B. Matesic, R. Bhargava "Towards Better than Human Capability in Diagnosing Prostate Cancer Using Infrared Spectroscopic Imaging", Genetic and Evolutionary Computation conference (GECCO) (2007)
3. F.N. Keith, R. Kong, A. Priya, R. Bhargava "Data Processing for Tissue Histopathology Using Fourier Transform Infrared Spectral Data" Proceedings of the 29th Asilomar Conference on Signals, Systems and Computers, IEEE (2007)

### ***Presentations***

#### **Invited conference presentations**

First author is the presenting author; First author is also the invited author unless indicated by \*

1. R. Bhargava, R.K. Reddy, R. Kong, G. Srinivasan "Engineering practical protocols for histopathology of human tissues and models using infrared spectroscopic imaging", Pittcon08, New Orleans, March 2008
2. R. Bhargava, R.K. Reddy, R. Kong, F. N. Keith, G. Srinivasan "Automated Cancer Histopathology by Practical Infrared Spectroscopic Imaging: Progress and Potential" The International Conference on Perspectives in Vibrational Spectroscopy (ICOPVS), Thiruvananthapuram, Kerala , India, February 2008
3. R. Bhargava, F.N. Keith, G. Srinivasan, R.K. Reddy, R. Kong "FTIR Imaging for pathology", EAS 07, Somerset, November 2007
4. R. Bhargava, F.N. Keith, G. Srinivasan, R.K. Reddy, R. Kong "Practical Aspects of Automated Histopathology using FTIR Imaging", FACSS 07, Memphis, October 2007

5. X. Llora, R.K. Reddy, B. Matesic, R. Bhargava\* "Towards Better than Human Capability in Diagnosing Prostate Cancer Using Infrared Spectroscopic Imaging", Human-Competitive Awards Symposium, Genetic and Evolutionary Computation conference (GECCO07, London, July 2007)
6. R. Bhargava, F.N. Keith, G. Srinivasan, R.K. Reddy, R. Kong "Mid-infrared Spectroscopic Imaging for Automated Cancer Pathology", ECI conferences, Naples, June 2007
7. IW Levin, R. Bhargava "Fourier-Transform Infrared Histopathologic Imaging: A Practical Protocol", ICAVS-4 Greece, June 2007

***Other invited presentations***

- Laser Science Center, Indian Institute of Technology, Kanpur, 2008
- National Center for Supercomputing Applications, UIUC, 2007
- Department of Pathology, University of Illinois, Chicago, 2007

***Contributed presentations***

*First author is the presenting author, unless indicated by \**

1. F.N. Keith, R.K. Reddy, R. Bhargava "Practical protocols for ultrafast histopathology by FTIR imaging", SPIE Photonics West, January 2008
2. R. Bhargava, R.K. Reddy, X. Llora "Histopathology without Human Supervision", BMES annual meeting, Los Angeles, September 2007

***Informatics such as databases***

Databases of spectra and spectral data sets have been combined for a new website –metaspectra.org

***Funding applied for based on work supported by this award***

Title of Grant Automated and Objective Laser Microdissection Using Infrared Microspectroscopy		RFA-RR-06-004 Role and % LOE	PI and Months Supporting Agency (including name and address of grants officer)	1.1 Academic Year
Grant ID				
Performance Period 1/1/08 - 12/31/10		Amount of Funding \$494,000		National Institutes of Health

Description (Include the goals and specific aims of the project)

The goal is to construct a laser capture microdissection instrument that does not require any human supervision or staining. The specific aims are to:

1. Develop an IR imaging device that is compatible with laser capture microdissection
2. Demonstrate IR-recognition guided microdissection of prostate tissue
3. Compare the gene expression profile of normal, cancer and adjacent normal prostate tissue using microdissected cells

Title of Grant

Quantifying stromal transformations for detecting lethal prostate cancer.

Grant ID

Idea Development Award

Role and % LOE

PI and 1 Summer Month Supporting Agency (including name and address of grants officer)

Performance Period

3/1/08 - 2/28/11

Amount of Funding  
\$308,000

Department of Defense

Description (Include the goals and specific aims of the project)

The goal is to measure the changes in prostate stromal tissue as a function of different pathologic conditions to predict onset of lethal disease. The specific aims are to:

1. Determine stromal components of prostate tissue without staining or human input
2. Correlate changes in stromal tissue with disease progression
3. Provide a model that incorporates both stromal and epithelial changes in predicting risk of cancer recurrence

***Employment or research opportunities applied for and/or received based on experience/training supported by this award.***

Dr. Gokulakrishnan Srinivasan, a post-doctoral fellow working on this project obtained employment with Bruker Optics.

## **Conclusion.....**

The work accomplished is a critical first step in establishing FT-IR imaging for pathology applications. Parameters were optimized and a fast data acquisition method is developed.

## ***So What Section***

If the reported progress is sustained, an automated method for prostate pathology will be available.

## References.....

<sup>1</sup> A Jemal, R Siegel, E Ward, T Murray, J Xu, C Smigal, MJ Thun Cancer statistics, 2006 *CA Cancer J Clin* **56**, 106-130 (2006).

<sup>2</sup> SM Gilbert, CB Cavallo, H Kahane, FC Lowe Evidence suggesting PSA cutpoint of 2.5 ng/mL for prompting prostate biopsy: Review of 36,316 biopsies. *Urology* **65**, 549-553 (2005).

<sup>3</sup> PF Pinsky, GL Andriole, BS Kramer, RB Hayes, PC Prorok, JK Gohagan, Prostate, Lung, Colorectal and Ovarian Project Team Prostate Biopsy Following a Positive Screen in the Prostate, Lung, Colorectal and Ovarian Cancer Screening Trial *J Urol* **173**, 746-750 (2005). discussion 750-751.

<sup>4</sup> PA Humphrey *Prostate Pathology* American Society of Clinical Pathology, Chicago (2003).

<sup>5</sup> EN Lewis, PJ Treado, RC Reeder, GM Story, AE Dowrey, C Marcott, IW Levin Fourier transform spectroscopic imaging using an infrared focal-plane array detector *Anal. Chem.* **67**, 3377-3384 (1995).

<sup>6</sup> R Bhargava, SQ Wang, JL Koenig Processing FTIR Imaging Data for Morphology Visualization *Appl. Spectrosc.* **54**, 1690-1706 (2000).

<sup>7</sup> DC Fernandez, R Bhargava, SM Hewitt, IW Levin Infrared spectroscopic imaging for histopathologic recognition *Nat. Biotechnol.* **23**, 469-474 (2005).

<sup>8</sup> Snively C M, Koenig J L. Characterizing the performance of a fast FT-IR imaging spectrometer. *Appl. Spectrosc.* 1999; **53** :170-177.

<sup>9</sup> Bhargava R, Levin, I W. Fourier transform infrared imaging: Theory and practice. *Anal. Chem.* 2001; **73** :5157 -5167.

<sup>10</sup> Bhargava R, Rebar T, Koenig J. Towards faster FT-IR imaging by reducing noise. *Appl. Spectrosc.* 1999; **53** :1313–1322.

<sup>11</sup> Bhargava R, Wang S, Koenig J. Route to higher fidelity FT-IR imaging. *Appl. Spectrosc.* 2000; **54** :486–495.

<sup>12</sup> Snively C, Katzenberger S, Oskarsdottir G, Lauterbach. Fourier-transform infrared imaging using a rapid-scan spectrometer. *Opt. Lett.* 1999; **24** :1841–1843.

<sup>13</sup> Green A, Berman M, Switzer P, Craig, M. A Transformation For Ordering Multispectral Data In Terms Of Image Quality With Implications For Noise Removal. *IEEE T. Geosci. Remote* 1988; **26** :65–74.

<sup>14</sup> Boardman J, Kruse F. Automated spectral analysis: a geological example using AVIRIS data, north Grapevine Mountains, Nevada. *Proceedings, ERIM Tenth Thematic Conference on Geologic Remote Sensing* 1994; 407–418.

<sup>15</sup> Wentzell P, Andrews D, Hamilton D, Faber K, Kowalski B. Maximum likelihood principal component analysis. *J. Chemometr.* 1997; **11** :339–366.

<sup>16</sup> Qin, S, Dunia, R. Determining the number of principal components for best reconstruction. *J. Process Contr.* 2000; **10** :245–250.

<sup>17</sup>. Cattell R B. The Screen Test For The Number Of Factors 1. *Multivar. Behav. Res.* 1966; **1** :245–276.

<sup>18</sup>. Wold S. Cross-Validatory Estimation Of Number Of Components In Factor And Principal Components Models. *Technometrics* 1978; **20** :397–405.

<sup>19</sup>. Valle, S, Li,W, Qin, S. Selection of the number of principal components: The variance of the reconstruction error criterion with a comparison to other methods. *Ind. Eng. Chem. Res* 1999; **38** :4389–4401.

---

<sup>20</sup>. Gonzalez R, Woods R, Eddins S. *Digital image processing using MATLAB*. Prentice Hall: USA, 2003., 378-425.

<sup>21</sup>. Canny J. A computational approach to edge detection. *IEEE T. Pattern Anal.* 1986; **8** :679–698.

<sup>22</sup>. Savitzky A, Golay M. Smoothing and Differentiation of Data by Simplified Least Squares Procedures. *Anal. Chem.* 1964; **36** :1627–1639.

<sup>23</sup>. Bhargava R, Levin I W. Gram-Schmidt orthogonalization for rapid reconstructions of Fourier transform infrared spectroscopic imaging data . *Appl. Spectrosc.* 2004; **58** :995-1000.

<sup>24</sup>. Gordon C. A generalization of the maximum noise fraction transform. *IEEE T. Geosci. Remote* 2000; **38** :608–610.

<sup>25</sup> R. Bhargava “Practical FTIR chemical imaging for cancer pathology” *Anal. Bioanal. Chem.*, **389**, 1155-1169 (2007)

<sup>26</sup> It is noteworthy that we are examining trends in the absorbance spectra. Strictly, SNR should be measured in single beam spectra to relate rigorously to theory. It can be shown, however, that the trend will hold approximately for the absorbance spectra as well. Many practitioners advocate the use of rms SNR. We are employing peak-to-peak fluctuations over the same spectral range. Hence, the noise values we obtain will be higher but will follow the same trend.

<sup>27</sup> Bhargava R, Wang SQ, Koenig JL *Appl. Spectrosc.* **54**, 486-495 (2000).

<sup>28</sup> Bhargava R, Wang SQ, Koenig JL *Appl. Spectrosc.* **54**, 1690-1706 (2000).

<sup>29</sup> RJ Anderson, PR Griffiths, *Anal. Chem.* **47**, 2339 (1975)

<sup>30</sup> X. Llora, R.K. Reddy, R. Bhargava, Under preparation

<sup>31</sup> X. Llora, A. Priya, R. Bhargava “Observer-Invariant Histopathology using Genetics-Based Machine Learning” *Nat. Computing*, In press (2007)

---

**Appendices.....**

# Towards a practical Fourier transform infrared chemical imaging protocol for cancer histopathology

Rohit Bhargava

Received: 30 May 2007 / Revised: 9 July 2007 / Accepted: 12 July 2007 / Published online: 5 September 2007  
© Springer-Verlag 2007

**Abstract** Fourier transform infrared (FTIR) chemical imaging is a strongly emerging technology that is being increasingly applied to examine tissues in a high-throughput manner. The resulting data quality and quantity have permitted several groups to provide evidence for applicability to cancer pathology. It is critical to understand, however, that an integrated approach with optimal data acquisition, classification, and validation is necessary to realize practical protocols that can be translated to the clinic. Here, we first review the development of technology relevant to clinical translation of FTIR imaging for cancer pathology. The role of each component in this approach is discussed separately by quantitative analysis of the effects of changing parameters on the classification results. We focus on the histology of prostate tissue to illustrate factors in developing a practical protocol for automated histopathology. Next, we demonstrate how these protocols can be used to analyze the effect of experimental parameters on prediction accuracy by analyzing the effects of varying spatial resolution, spectral resolution, and signal to noise ratio. Classification accuracy is shown to depend on the signal to noise ratio of recorded data, while depending only weakly on spectral resolution.

**Keywords** Fourier transform infrared spectroscopy · FTIR imaging · Infrared microscopy · Prostate · Histopathology · Microspectroscopy

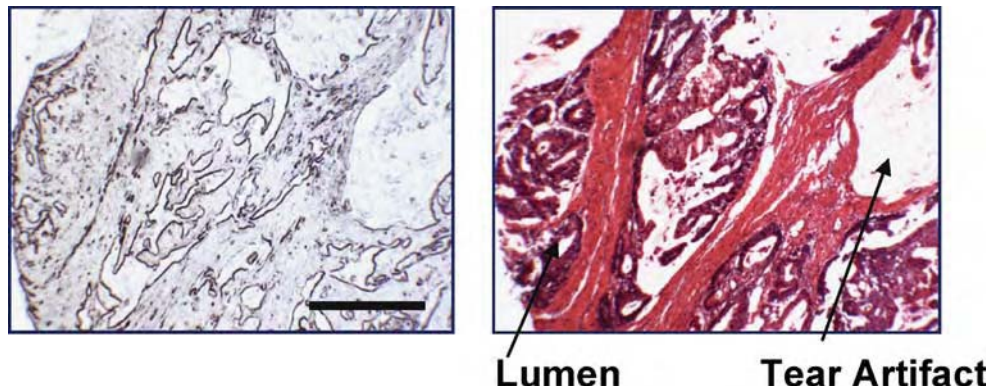
## Introduction

Cancer is one of the leading causes of death in the western world and is becoming increasingly prevalent worldwide. It is well established that appropriate therapy for cancers diagnosed early generally leads to improved prognosis and longer survival. Consequently, population screening tests to detect disease are increasingly being deployed. The emphasis in screening populations is on obtaining a high sensitivity through simple diagnostic tests. For example, the prostate-specific antigen (PSA) assay [1] helps triage persons at risk for prostate cancer. A cutoff level (typically  $4 \text{ ng mL}^{-1}$ ) or increase in PSA velocity implies that the screened person should be at heightened surveillance and typically undergoes a biopsy to confirm disease. Morphologic structures in biopsied tissue, as diagnosed by a pathologist, are the only definitive indicator of disease and form the gold standard of diagnosis [2]. Along with clinical history, stage, and PSA values, pathologic diagnoses form a cornerstone of clinical therapy and serve as a basis for a vast majority of research activity [3].

Typically, multiple samples are withdrawn from the organ during biopsy. Extracted tissue samples are fixed, embedded, and sectioned (typically to 1- to 5- $\mu\text{m}$  thickness) onto a glass slide for review. By itself, tissue does not have much useful contrast in optical brightfield microscopy. Hence, the prepared slide is stained with dyes. A mixture of hematoxylin and eosin (H&E) is commonly employed, staining protein-rich regions pink and nucleic acid-rich regions of the tissue blue, for example, as shown in Fig. 1. Using the contrast, a trained person can recognize specific cell types and alterations in local tissue morphology that are indicative of disease. In prostate tissue, epithelial cells line three-dimensional ducts. In two-dimensional thin sections, thus, the cells appear to line empty circular regions (lumen).

R. Bhargava (✉)  
Department of Bioengineering and Beckman Institute for Advanced Science and Technology,  
University of Illinois at Urbana-Champaign,  
Urbana, IL 61801, USA  
e-mail: rxb@uiuc.edu

**Fig. 1** Brightfield microscopy images of unstained (left) and stained (right) prostate tissue sections. Hematoxylin and eosin (H&E) stains provides contrast, allowing a trained person to recognize epithelial cells and ductal structure (lumen), while ignoring artifacts and confounding morphologies. A trained human can also learn to robustly recognize patterns within lumen that indicate cancer. The scale bar corresponds to 100  $\mu$ m



Distortions in normal lumen appearance provide evidence of cancer and characterize its severity (grade). The process is fundamentally a manual pattern recognition that seeks to match observations to known healthy or diseased morphologies.

Manual examination of biopsies is very powerful in that humans can not only recognize disease generally but can also overcome confounding preparation artifacts, detect unusual cases, and recognize deficiencies in diagnostic quality. This capability of considering and neglecting features based on prior knowledge is crucial for accurate and robust diagnoses. The process, however, is time consuming, allows for limited throughput and, frequently, leads to variance in subjective judgments about the disease severity, i.e., grade [4]. As an alternative, computer-based pattern recognition approaches to diagnose disease may provide more accurate, reproducible, and automated approaches that could reduce variance in diagnosis while proving economically favorable. Hence, attempts have been made to characterize morphology using H&E image analysis as well as biomarkers to stain for specific molecular features. Automated approaches that can rival human performance in usual clinical settings, however, are still unavailable. Specifically, the attributes of high accuracy and robust applicability are lacking.

The information content of H&E-stained images is limited and attempts to automatically recognize structural patterns indicative of prostate cancer, unfortunately, have not led to clinical protocols. Similarly, probe-based molecular imaging can provide exquisite information regarding the location and content of specific epitopes but is limited by complex diseases not expressing universally the same epitopes or panels of markers. Stains used can generally detect one feature that may aid diagnosis (e.g., AMACR) but do not provide entire diagnostic information in themselves. An exciting alternative is emerging in the form of chemical imaging and microscopy [5]. As opposed to conventional dye-assisted imaging or probe-assisted molecular imaging, chemical imaging [6] seeks to directly measure the identity and/or concentration of chemical species in the sample using spectroscopy. Hence, no

molecular probes (MPs) are needed to see the presence of specific epitopes; instead computer algorithms are used to extract information from the data (instead of MP hybridization) and statistical methods are used to provide confidence (as opposed to brown tints for MPs). The approach is limited only by the ability of the technology to sense specific types of molecules or otherwise resolve chemical species and morphologic structures. Among the prominent approaches are vibrational spectroscopic imaging, both Raman and infrared (IR), as well as mass spectroscopic imaging (MSI) [7, 8] and magnetic resonance spectroscopic imaging (MRSI) [9]. While each technology promises a specific measurement (e.g., proteins or metabolic products) for specific situations (e.g., *in vivo* or *ex vivo*), IR spectroscopic imaging [10] is particularly attractive for the analysis of tissue biopsies in that it permits a rapid and simultaneous fingerprinting of inherent biologic content, extraneous materials, and metabolic state [11–14].

IR spectroscopic imaging, generally practiced using interferometry and termed Fourier transform infrared (FTIR) spectroscopic imaging or, succinctly, FTIR imaging, offers a particular combination of spatial, spectral, and chemical detail [15]. Limitations of FTIR imaging include coarser spatial resolution compared to Raman imaging or high powered optical microscopy and lack of specific molecular detail compared to MSI. Tissue biopsies are examined as thin sections on a solid substrate. The tissue is dehydrated and is stable due to fixation. Typically, structures of pathologic interest are several to hundreds of micrometers in size, requiring fairly moderate magnifications for decision making. These conditions imply that the need to image *in vivo*, at exceptionally high spatial resolution, or in aqueous environments is not critical and that standard pathologic laboratory processing can be employed for IR imaging. Due to the linear absorption process being utilized, the signal from IR spectroscopy is large and readily obtained, promising relatively simple instrumentation. Hence, the technology provides a platform that is potentially useful for clinical practice in pathology. It must be emphasized that no particular technology is ideally suited to all applications but a careful matching of the

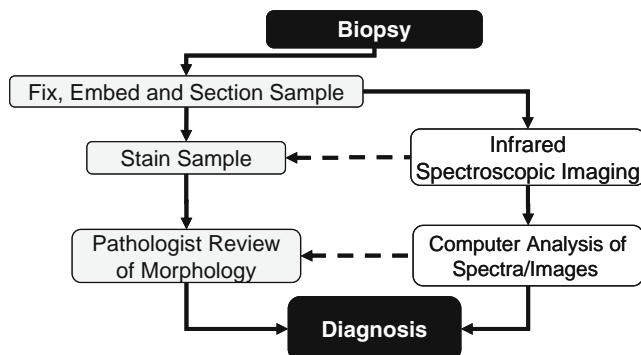


**Fig. 2** Potential application of FTIR imaging for pathology. The current paradigm of cancer diagnosis and grading upon biopsy involves sample processing, staining, and pathologist review (*left, shaded boxes*). To implement the paradigm of automated analysis (*right, unshaded boxes*), IR chemical imaging is followed by computer analysis for diagnosis. Since IR imaging is label-free and non-perturbing, the sample can be stained, providing the pathologist with both IR chemical and conventional stained images

technique to the application can lead to useful protocols. While the potential advantages of FTIR imaging for examining tissue biopsies is high, practical protocols for clinical deployment are being developed by many groups.

Numerous recent reviews are available to address biomedical applications of FTIR spectroscopy and imaging [16–20], especially related to diseases and cancer. These reviews address instrumentation, the applicability to various

systems, spectroscopic bases and classification algorithms for decision making, and controversial aspects in the backdrop of the evolution of the field. The commercial availability of high-fidelity FTIR imaging instruments, advances in computers and data analysis algorithms, and increasing interest have combined to generate an increasing volume of studies. At the same time, there is considerable debate emerging on various aspects of the process. Reports study a variety of organs that may not correlate in behavior, utilize different sample acquisition and processing techniques, employ different instrumentation, data acquisition, or handling protocols, and apply a variety of decision-making algorithms. While this has led to a lively community of practitioners and exploration of various facets such as resolution, biological diversity, and chemometric or statistical methods, studies have generally focused on one aspect. Many excellent studies have developed each of these aspects to the point of routine use in advanced laboratory. The focus in the field is now on understanding biochemical signals and developing protocols from high quality data that can actually lead to clinical acceptance. We contend that the development of clinical protocols is necessarily integrative and, in this manuscript, review first the salient aspects in developing a practical, integrative approach to spectroscopic imaging for cancer histopathology. Second, we discuss the issues of spatial selectivity, sample size calculations,

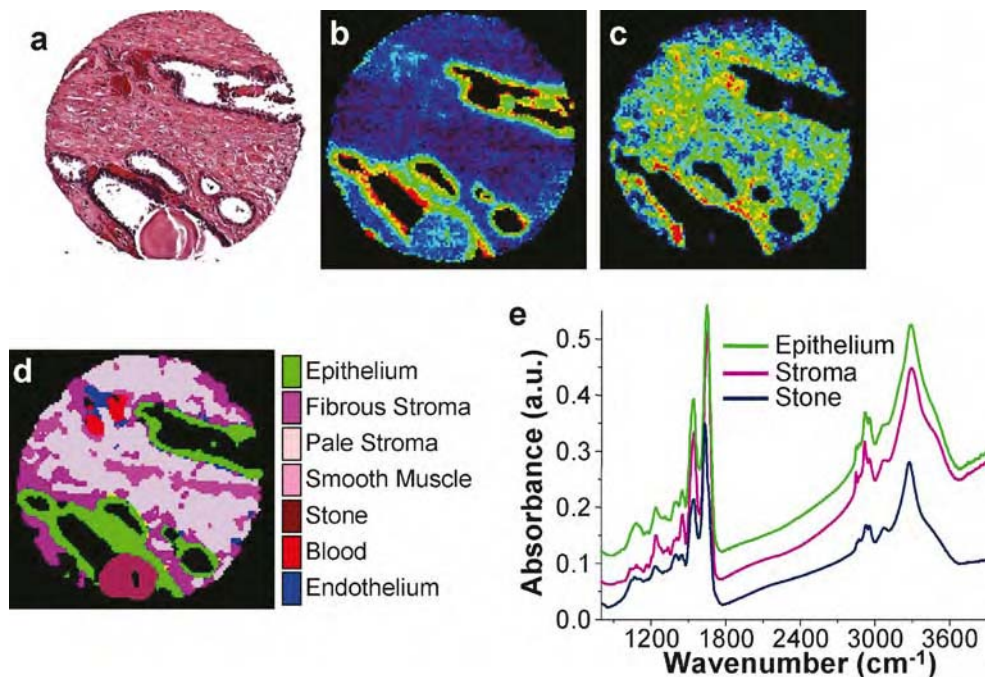


**Fig. 3** Correspondence of conventionally stained and FTIR chemical images for pathology applications. **a** Hematoxylin and eosin (H&E)-stained image of prostate tissue section. Hematoxylin stains negatively charged nucleic acids (nuclei & ribosomes) *blue*, while eosin stains protein-rich regions *pink*. The diameter of the sample is ca. 500  $\mu\text{m}$ . Simple univariate plots of specific vibrational modes provides for enhancement or suppression of specific cell types. **b** Absorption at

$1,080 \text{ cm}^{-1}$  commonly attributed to nucleic acids, highlights nucleic-rich epithelial cells in the manner of hematoxylin. **c** Spatial distribution of a protein-specific peak (ca.  $1,245 \text{ cm}^{-1}$ ) highlights differences in the manner of eosin. The entire spectrum can be analyzed for a series of markers that provide more information than H&E or univariate images, as shown in **d** where specific cells are color coded based on their spectral features (**e**)

optimization considerations, and potential improvements in algorithms that can provide faster results. Tests to determine performance and limits of accuracy are reported as a function of experimental parameters. We focus here on prostate histology as an illustrative test case, but emphasize that the approach is applicable and similar insight is gained with other tissues [21]. Further, exciting results have recently been reported for diagnosis, grading, and classification of prostate cancer [22–26], including the effects of zonal anatomy [27] and cytokinetic activity on spectra [28]. An extension of the methodology here to pathology will help formulate better protocols and allow a better understanding of the performance of classifiers.

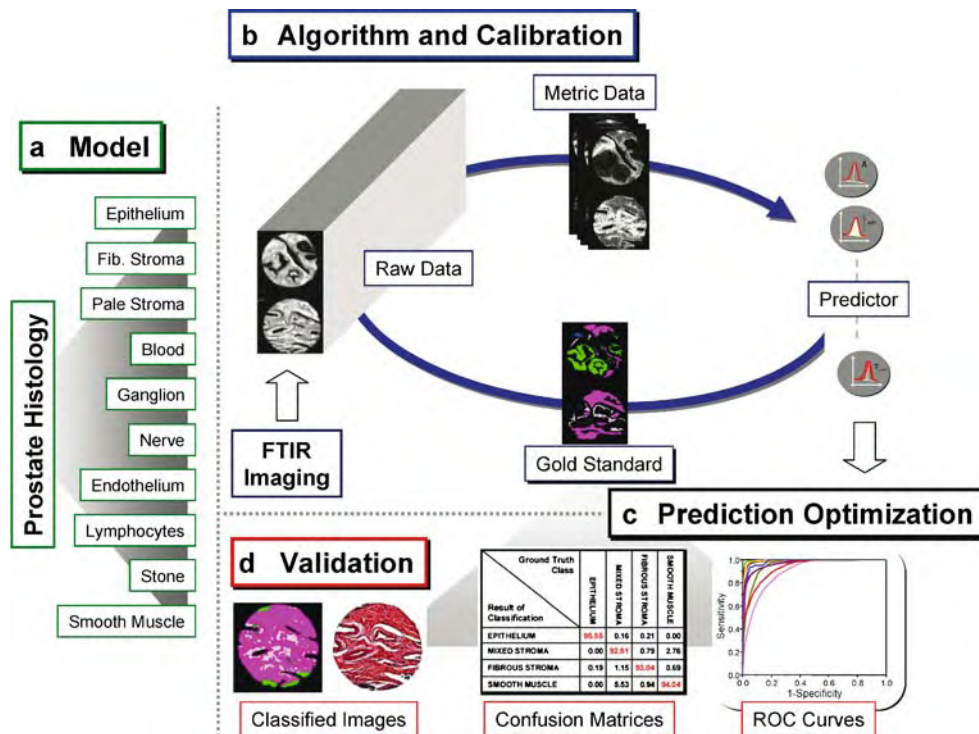
### Approach and essentials

The promise of chemical imaging for pathology is illustrated in Fig. 2. Our approach has been to attempt integration of our developments with current clinical practice. Hence, we employ tissues that have been biopsied, fixed, embedded, and sectioned as per usual clinical protocols. We differ in the de-paraffinization step, suggesting a gentle wash with hexane and do not stain the tissue. Additionally, as IR chemical imaging only employs benign light, it is non-perturbing and entirely compatible with all downstream pathology processes. Hence, the sample may be stained as usual (Fig. 2, dashed arrow, top). Visualizations similar to those observed in conventional pathology are possible without staining the tissue. For example,

Fig. 3 correlates H&E and infrared spectral images. Visualizations similar to H&E images may be “dialed-in” by utilizing specific spectral features indicative of tissue chemistry. Although, the IR data only demonstrate univariate representations in the images, automated mathematical algorithms can determine the cell types and their locations within the image, while providing quantitative measures of accuracy and statistical confidence in results [29]. These data may be employed to directly provide diagnoses or to inform the pathologist (Fig. 2, dashed arrow, bottom), helping them make better decisions. Since the results are images, information exchange between spectroscopists and clinicians is facilitated. Spectroscopic analyses can potentially be fully automated; thus, no additional users need to be trained or knowledge base acquired by current clinicians.

A major challenge in the field is the development of robust algorithms that employ spectral data to provide histopathologic information. Both supervised and unsupervised approaches have been employed. We believe that unsupervised methods are more suited to research and discovery. Supervised methods are preferred when the data need to be related to known conditions, e.g., clinical diagnoses. The development of supervised classification of IR chemical imaging data for histopathology is fairly straightforward [30]. The process is shown in Fig. 4. First, a model for classification is selected. The model comprises all possible outcomes for any pixel in the images and is, hence, bounded by definition. We term each histologic constituent of the model a class to denote that it may not correspond to specific cell types or entities corresponding

**Fig. 4** Process for relating pathologic or physiologic state to FTIR chemical imaging data. A model is chosen for supervised classification (**a**). **b–d** Training data is reduced in size and optimized into a prediction algorithm using gold standard data. The developed algorithm is validated against a second, independent data set and the accuracy is measured using three different methods: ROC curves, confusion matrices, and image comparisons



to morphology-based pathology. While this allows for simplifications and allows the user to focus on specific cells relevant in disease, it is also likely to prove useful in the discovery of different chemical entities that appear morphologically identical.

Next, data from a large number of tissue samples is recorded. A set of pixels are specifically marked (gold standard) by different colors to correspond to known regions of tissue, usually by comparison with an H&E-stained image or with immunohistochemically stained images [21]. The recorded data set is reduced to a smaller set of measures that capture the classification capability of the entire data set. We termed these measures metrics. There are numerous means of obtaining the metric data set: manual selection of large spectral regions, principal components analysis, genetic algorithms, or a sequential forward selection algorithm. A numerical algorithm is then chosen, for example, a linear discriminant analysis, neural network, SIMCA, or modified Bayesian classifier [31]. The classifier is optimized iteratively, if needed, to optimally predict the training data set. Subsequently, the algorithm is applied to a second data set (independent validation) that has been independently marked for each class. A comparison of the gold standard marking with the computationally predicted class provides a measure of the accuracy. We have employed three measures of accuracy: receiver operating characteristic (ROC) curves [32] that represent the sensitivity and specificity trade-off of the classifier, confusion matrices that provide the fraction of pixels of each class classified as pixels of all classes, and classified images that can be compared pixel-for-pixel to other images. Additionally, it is often instructive to drill into the classifier to obtain the basis for classification or the distribution of confidence intervals for various samples. The last two factors are generally not apparent in previous studies.

There are three key developments that are needed for this approach to be successful: (a) high-fidelity FTIR imaging instrumentation, (b) high-throughput sampling, and (c) robust classification that provides statistically significant results in a manner that can be appreciated by non-experts in spectroscopy. We briefly review the three developments next.

## FTIR imaging

### Need for spatially resolved data

The need for spatially resolved data has been recognized [33], but the effect of limited resolution data on classification is not entirely clear. The primary complication of coarse spatial resolution, obviously, arises from boundary

pixels. These can be defined as pixels that are assigned to one class but would likely yield more classes, to their physical limits, were finer resolution available. As a consequence, the spectral content of the boundary pixel is likely to be mixed and will likely lead to errors in classification. For example, the confounding contribution of stromal spectra to cancerous epithelial cells in breast tissue has been proposed [34]. As the resolution becomes coarser, the fraction of pixels in an image that belong to boundary pixels increases. Inclusion of these pixels has been shown to be a primary contributor to error rates in data [29], while their exclusion in accounting for accuracy necessarily implies that not all pixels are included. We sought to examine the effect of spatial resolution on the prevalence of boundary pixels.

We binned data acquired at 6.25- $\mu\text{m}$  pixel size from 148 samples in a validation data set ( $\approx$ 7000 pixels/sample) to 10-, 15-, 20-, 30-, and 50- $\mu\text{m}$  pixel sizes. There is an important distinction between pixel size and spatial resolution. The pixel size denotes the best possible optical resolution, which may be limited by longer wavelengths in the spectrum and optical effects to yield a poorer measured resolution [35–38]. For each dataset, we classified the tissue and determined neighbors of each pixel that did not belong to the class of the pixel. Some pixels that have no neighbors of other classes may still have empty pixels as neighbors. Since neighboring empty pixels can only provide optical distortion [39] but do not affect spectral content; we do not consider them further. The number of neighbors for epithelial pixels for different spatial resolutions may be seen in Fig. 5. The first observation is that a large majority of pixels have the same class pixels as all eight neighbors. The fraction of pixels with all neighbors of the same class

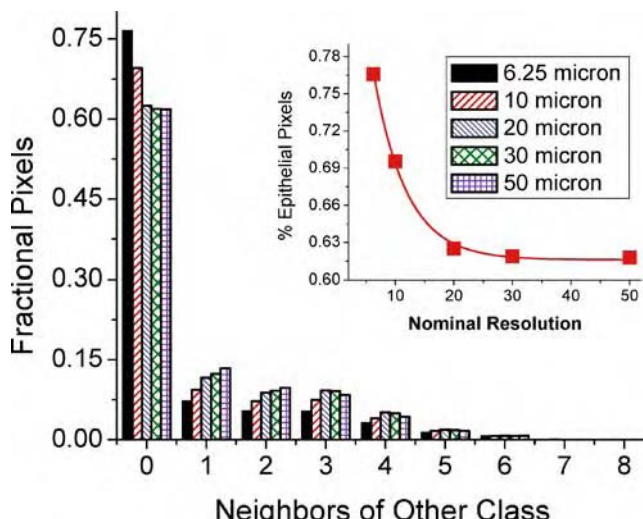


**Fig. 5** Neighbors of cell types other than epithelium or empty space for different spatial resolutions. The *inset* shows the decrease in percent epithelial pixels that do not have any other cell types as neighbors

decreases rapidly with decreasing resolution and stabilizes at ca. 20  $\mu\text{m}$ . Hence, a spatial resolution coarser than 20  $\mu\text{m}$  is unlikely to have an effect on the classification but is expected to lead to about 25% more epithelial pixels being contaminated compared to 6.25- $\mu\text{m}$  pixel sizes. The precise effect on a specific sample is very dependent on the sample morphology and is generally associated weakly with pathologic state. While in itself, the statistic does not imply that results from coarser resolution studies will be invalid, practitioners must recognize that error rates may be higher and that this contribution may be mitigated by using commonly available imaging systems.

One danger of classifying mixed composition pixels is whether they may be classified as an entirely different class or disregarded from the data set as belonging to no class. We simulated pixels of composition ranging from 0 to 100% for pairs of each class. We also added noise to simulate different data acquisition conditions. An example of the data can be seen in Fig. 6. Average spectra, one each from the two classes, are baselined and added in ratios varying linearly from 0 to 100%. Figure 6b demonstrates the classification of the gradient data set. In general, the classifier works well, favoring the class with higher concentration. The classifier is also stable at the noise levels examined. A surprising result is that pixels between epithelium and fibroblast-rich stroma are classified as mixed stroma. This drawback, however, is the only example of two classes mixing to yield an entirely different one. The reason also stems from the definition of the mixed stroma class. While the class was designed to handle those

stromal cells that were not clearly fibroblasts or smooth muscle in origin but appeared mixed, a mix of epithelium and fibroblast-type stroma also leads to the classification as mixed stroma. Noise seems to have little effect on this behavior.

The full simulation of all classes (not shown) reveals that mixed pixels generally can be classified as the constituent classes with the higher concentration. Clearly, boundary pixels at epithelial fibroblast-rich regions must be handled with care. The increase in boundary pixels at lower resolution also implies that this type of systematic misassignment may arise more frequently. The rate of occurrence of boundary pixels may be even lower for synchrotron-based imaging that is conducted at higher pixel density or in emerging approaches that utilize synchrotron-based interferometers and array detectors. The simulated example above, however, demonstrates that simply oversampling a spatial region to increase pixel density may allow for better definition of the interface and assignment of pixels, though it will not address spectral purity. Hence, for analyses based on spectral discrimination, mixture models will have to be developed based on entire spectra. For example, multivariate curve resolution techniques hold promise.

A further complication arises in using data from histologic classification for pathologic diagnoses. For example, the boundary epithelial pixels classified above may disproportionately contribute to classification errors. We have found evidence for the same in studies for both cancer pathology and for histology in tissue from different organs. For example, the boundary pixels in benign tissue get

**Fig. 6** Mixture models and classification for prostate histology. **a** Absorbance at 1,080  $\text{cm}^{-1}$  for three classes and their mixtures. The first column contains mixtures of epithelial cell spectra with the average spectrum from fibroblast-rich stroma and mixed stroma. The second and third columns contain mixtures with fibroblast-rich and mixed stroma, respectively. The concentration changes from 0 to 100% linearly along the *y*-direction as indicated by the color bar in **c**. **b** Along the *x*-axis of the composite image, the noise in each cell increases linearly. Error bars are standard deviations of noise in the spectra. **c** Classified image for the data, demonstrating the effect of composition and noise on classification. **d** Probability profiles of the three cell types at columns 1 and 25, demonstrating the effect of noise

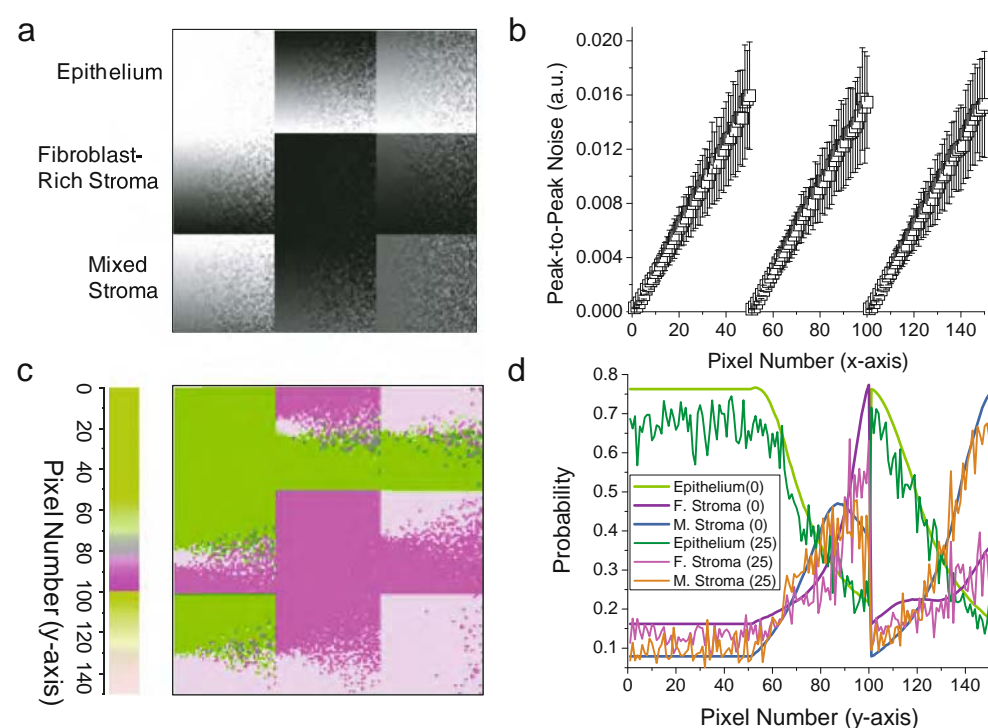


**Table 1** Correlation of composition for samples between 6.25-mm pixel sizes and other pixel sizes

Pixel size (micron)	Epithelium	Fibroblast-rich stroma	Mixed stroma
10	0.9913x(0.9976)	0.9847x(0.9923)	1.0300x(0.9957)
20	1.0156x(0.9906)	0.9671x(0.9775)	1.0473x(0.9787)
25	1.0404x(0.9896)	0.9768x(0.9624)	1.0262x(0.9617)
30	1.0720x(0.9773)	0.9683x(0.9507)	1.0175x(0.9363)
50	1.1180x(0.9459)	0.9410x(0.8947)	1.0390x(0.8723)

The first row in each cell denotes the composition factor for that pixel size and class. For example, for every  $100 \mu\text{m}^2$ , the area of epithelial pixels at  $10\text{-}\mu\text{m}$  pixel size is 99.13% of that at  $6.25\text{-}\mu\text{m}$  pixel size. Increasing/decreasing numbers represent pixels being increasingly/decreasingly classified as that class. The ratios are not uniform for every sample and the regression coefficient of the best fit line passing through the origin is provided in the second row of the each table cell. Increasing pixel sizes reflect greater variance from the fit line

misclassified as cancerous, leading to the major source of error in applying this approach to pathology. At this time, the evidence is anecdotal and needs further investigation to quantify the extent of the error and its mitigation by advanced numerical processing. The last interesting aspect of lower spatial resolution is that it tends to over-predict certain classes. For example, Table 1 demonstrates the regression results of each samples composition against that obtained at  $6.25 \mu\text{m}$  for three classes. While the regression coefficient is high, it is clear that epithelial and mixed stroma fractions are overestimated and fibroblast-rich stroma is underestimated with decreasing pixel size. There are differences based on underlying pathology. For example, normal epithelium is generally encountered in  $10\text{-}$  to  $40\text{-}\mu\text{m}$ -wide strips, while high grade tumor may be hundreds of micrometers to millimeters in size. Individual sample variability reflected in the regression coefficient decreases with increasing pixel size. In spectroscopic models to predict diseases that include morphological units but are based on average spectra, mixed pixels may lead to estimates with large errors. For example, a 1:1 mixed region of epithelial and fibroblast pixels at  $6.25\text{-}\mu\text{m}$  pixel size increases to ca. 1.19:1 for  $50\text{-}\mu\text{m}$  pixel size. Hence, the use of histologic mixture models at limited spatial resolution may not be estimated correctly, providing evidence that the percentage content of cell types in a limited field of view is likely to be a less robust measure of tissue histopathology.

#### *Evolution and capabilities of current instrumentation*

To overcome confounding by mixing, as discussed above, microscope spectroscopy was proposed as an alternative [40]. Single spectra (non-FTIR) have been recorded from microscopic samples for over 50 years [41] by restricting light incident on the sample through an aperture. More than one point, however, is required for tissue analysis. Hence, sequentially rastering the point at which spectra are recorded, termed mapping or point microscopy, was proposed [42]. A practical instrument obtained by coupling an interferometer, a microscope, and automated stage in the

late 1980s [43] helped in numerous materials science [44], forensic [45], and biomedical [46, 47] studies. Unfortunately, the mapping approach has a number of drawbacks in realizing the goal of an FTIR microscopy analog to optical microscopy [48].

More than 85% of cancer arises in epithelial cells, which often form surface layers that are  $10\text{-}$  to  $100\text{-}\mu\text{m}$  wide. As we demonstrated in the previous section, however, a resolution higher than ca.  $10 \times 10 \mu\text{m}$  is preferable. Consequently, the illuminated spot at the sample has to be made smaller, throughput decreases proportionally, which in turn decreases the signal to noise ratio (SNR) of acquired spectra. Orders of magnitude brighter sources, e.g., synchrotrons, may be employed to recover the lost SNR. Unfortunately, synchrotron or free electron lasers [49] are prohibitively expensive and no laboratory lasers exist for the wide spectral region. An alternative is to average successive measurements (co-adding) to increase statistically the SNR. Since the SNR increases only as the square root of the number of averaged spectra, long averaging periods are required. The situation may be mitigated by using higher condensing optics, sources at higher temperatures, slightly faster scanning than used here,<sup>1</sup> gain ranging [50], or ultra-sensitive detectors [51]. Even if a hypothetical instrument with all these advances were constructed, ca. 10- to 20-fold reduction in time would be obtained. Furthermore, this calculation underestimates the time required by not considering losses due to diffraction or stage movement.

In prostate tissue, for example, the situation is similar to Fig. 1. Epithelial cells form  $10\text{-}$  to  $35\text{-}\mu\text{m}$ -wide foci around the cross-sections of ducts. Ducts appear as white circles in Fig. 1b, surrounded by epithelial cells that are depicted in blue. To analyze this morphology, aperture dimensions of ca.  $6 \mu\text{m} \times 6 \mu\text{m}$  ( $\approx$  cell size) are proposed [31]; for this case, the mapping approach would require ca. 1,028 h for a

<sup>1</sup> There is no advantage to faster scanning once the modulation frequency has reached optimum level for MCT detectors (1 MHz). The reduced time to observe signal then decreases the SNR.

500  $\mu\text{m} \times 500 \mu\text{m}$  sample [31]. Hence, mapping is not a viable option. In contrast to point mapping using apertures, large fields of view are measured in FTIR imaging. Contributions from different sample areas in imaging are separated by an array of mid-IR-sensitive detection elements in the manner of imaging with CCD devices for optical microscopy. By coupling the multichannel detection of focal plane array (FPA) detectors with the spectral multiplexing advantage of interferometry, an entire sample field of view is spectroscopically imaged in a single interferometer scan [52]. Depending on the microscopy configuration, thousands of moderate resolution spectra can be acquired at near-diffraction-limited spatial resolution in minutes [53, 54]. The time advantage over mapping is nominally the number of pixels in the FPA (16- to 65,000-fold) but the noise characteristics of FPAs are poorer than sensitive single point detectors [55]. Hence, the SNR-normalized advantage is lower [56]. Faster detectors are being used for imaging and promise significantly higher SNR in the same time. For example, we have employed a 128  $\times$  128 element MCT array operating at ca. 16 kHz to acquire a full data set in ca. 0.07 s [unpublished]. These rates of data acquisition are approximately a factor of 10 higher than commercially available, but are required for practical data acquisition times. Increase in data acquisition speed remains a bottleneck for applications of IR imaging to routine clinical studies. Coupled with the complexity and cost of instrumentation, present technology provides preliminary capability but is likely to prove a barrier to practical clinical translation.

## High-throughput sampling and statistical pitfalls

### Quantitative analyses of results

The best imaging instruments (which employ sensitive detectors and a small multichannel advantage) can acquire data in about 0.1% of the time required for mapping for equivalent parameters. Hence, point mapping studies in pathology typically exceed numbers in only one of these categories: spatial resolution (ca. 15–20  $\mu\text{m}$ ), numbers of patients (ca. 50) or recorded small numbers of spectra per patient (ca. 100). These numbers may typically be improved an order of magnitude with imaging. For example, a recent report analyzed ca. ten million spectra from ca. 1,000 samples at a spatial resolution of 6.25  $\mu\text{m}$  [26]. This quantitative validation is necessary for any automated biomarker approach (*vide infra*) [57]. Studies are underway in our and other laboratories to correlate spectral patterns with other physiologic and pathologic conditions; recent published studies verify the robustness and potentially wide applicability of FTIR microscopy [58, 59].

### Sample size

Though these studies demonstrate potential, [60, 61] considerable debate exists on reproducibility and accuracy measures for larger studies [29]. The first response of many practitioners to new data is a question of validity based in limited statistical confidence. A detailed understanding is emerging from the work of several groups regarding appropriate sample control [62] and confounding factors due to biology [63]. Inherent differences between patient cohorts, effects of sample preparations and measurement noise are topics that can be addressed with the available imaging technology but are yet to be fully explored. Hence, validating robust spectral markers for large sample populations [64, 65] is exceptionally challenging and the chance for chance and bias influencing results exists.

Most importantly, the fundamental question of sample size required has remained open. There are two major concerns: first, the optimal sample size in forming calibration sets and a prediction algorithm. Second, investigators must determine whether the results shown can be supported by statistical considerations. While the first problem is essentially one of optimizing a model and prediction algorithm, the second impacts the quality of results and claims of applicability directly. In this manuscript, we examine only the second aspect. Determining the optimal sample size to form robust models is a more involved problem and is discussed elsewhere. The statistical validity of obtained results and dependence on data acquisition parameters are discussed later in this manuscript. Specifically, we estimate sample size based on the standard error for the area under the curve for an ROC curve.

### Gold standard

The selection of pixels as gold standards needs great care. It must be done independently of any classifier training or validation, thus ensuring a blinded study design. Once the gold standard set is determined, it must not be changed. This will ensure that there is no bias in the process. Care must be taken to avoid pixels that do not lie on the tissue or those that are at the boundary as these may artificially inflate the error. The use of all pixels in an image has been suggested and their exclusion has been proposed to contribute selection bias. Selection bias, however, does not arise in pixels that are chosen independent of validation algorithms. The exclusion of boundary pixels is necessary in both training (to avoid spurious probability distribution functions) and validation (to prevent introduction of errors). There are major technological difficulties in relating stained visible to IR images from unstained tissue due to changes during staining, leading to errors. Hence, it has been proposed that the exclusion of boundary pixels in akin to

the performance of a classifier with a reject option for the boundary.

#### *Sampling, archiving, and consistency*

While it is unclear what an optimal sample size would be, it is clear that a large number of tissue samples are needed for effective validation. While it may theoretically be possible to train on a single sample, validation of a protocol is required on more samples. We recognized that one does not need to observe the full surgically resected tumor for validating IR protocols, but would need a representative small section. Hence, we employed tissue microarrays (TMAs) [66] as a platform for high-throughput sampling. TMAs consist of a large number of small tissue samples arranged in a grid and deposited on the same substrate. They are typically manufactured by embedding cylindrical cores in a receiving block and sectioning the block perpendicular to the long axis of the core. Thin sections are then floated on to a rigid substrate for analysis. The technique facilitates rapid visualization of results of any classification protocol, while revealing localization and prevalence of any errors. Sample processing times may easily be increased 100-fold, valuable tissues are optimally utilized, and consecutive TMA sections can be used to correlate with staining results. Construction and analysis of TMAs has been automated, further increasing the throughput. For spectroscopists, TMAs provide a ready source of tissue to test hypothesis and develop prediction models.

The validity of employing TMAs for prostate cancer research and, especially, for cancer grading has been addressed by a number of authors [67]. For example, a study of genitourinary pathologists [4] with images from TMA cores assesses that ca. 90% considered this approach useful for resident training and for pathology teaching. Further, Gleason score was easily assigned to each TMA spot of a 0.6-mm-diameter prostate cancer sample. Hence, the utility of TMAs is not only in providing numerous samples in a compact manner for the advantages above, but also in consistency of the diagnoses and precision in analyzing similar areas. Virtual tissue microarrays could be constructed from different areas of large samples, thus providing many sub-samples for within-patient and among-patient comparisons. This approach has not yet been reported but is likely a useful extension of the TMA concept.

#### **Prediction algorithms and high-throughput data analysis**

##### **Univariate algorithms**

The major technological advances of fast FTIR microscopy and high-throughput tissue sampling have been addressed

by imaging and TMAs respectively. There is still some confusion and widespread disagreement, however, about the “best” approach to extract histopathologic information from FTIR imaging data. Several early manuscripts employ univariate correlations to disease states [68]. While the results were exciting, it is now realized that they were statistically flawed and did not necessarily contain a fundamental basis in cancer biology. To our knowledge, there is no manuscript that has expressly demonstrated, using statistics arguments, why univariate analyses are likely to fail. There is widespread consensus and anecdotal evidence, however, among practitioners that argues against the approach. Consider the distributions for a univariate measure (absorbance at  $1,080\text{ cm}^{-1}$  that is normalized to the amide I peak height) for benign and malignant cases as shown in Fig. 7.

The normalized histograms reveal that for specific, single samples the distribution of absorbance at pixels is such that it clearly indicates the metric to be a good one for cancer discrimination. When the distribution from all samples is considered, however, there is little difference in the distributions. Hence, many univariate measures described in the literature do not hold up in wide population testing. A TMA-based, high-throughput validation can easily prove that the measure is not a good one but does discriminate some samples. In Fig. 7, a cutoff value can generally be found that distinguishes disease, leading to the erroneous conclusion that the feature is universally indicative of disease state. Since a typical infrared spectrum has numerous frequencies and even non-chemically specific features that can provide discrimination, a small number of samples increases the probability of finding such discrimination by chance alone. Univariate measures that appar-

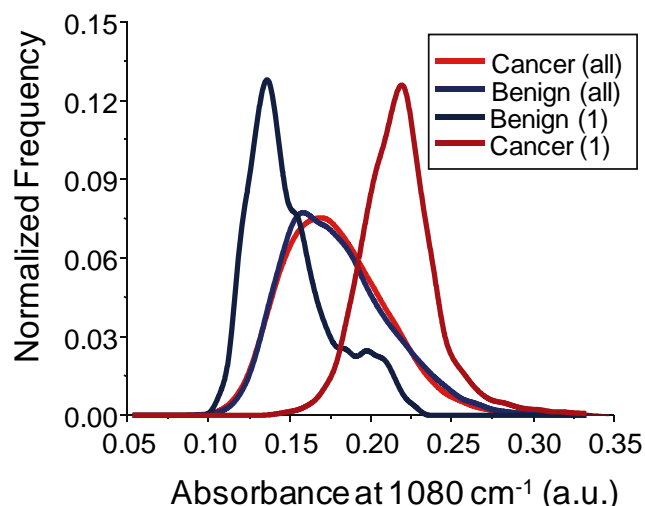


**Fig. 7** Distribution of absorbance for individual spots and all pixels from each class, normalized by the total number of pixels in the class, demonstrates that the examination at patient level and at a global level may not correspond

ently provide discrimination when none exists can be equated to the false discovery rate (FDR) [69] of metrics. The FDR is very different from the *p*-value for determining that a metric separates two distributions; a much higher FDR can be tolerated than can a *p*-value. Similarly, a false negative rate has been proposed [70], which is not critical for our case as we have observed high accuracy without use of any erroneously left out metrics. While detailed calculations and their underlying concepts are too lengthy to reproduce here, for the sake of completeness, it suffices to say that for the expected number of metrics demonstrating discrimination, the FDR tends to zero for larger than ca. 30 samples. While correlations due to chance can be minimized by this approach, there is potential for unknown bias or error in prediction for small numbers of samples. Hence the algorithm must be integrated with sampling considerations.

#### Multivariate algorithms

It was argued in the previous section that univariate analysis may not provide a good measure of the population distribution. It can alternatively be argued that the individual differences in univariate measures are masked if population measures of the same are employed. Similarly, multivariate techniques may mask the individual measures in population testing. Hence, our philosophy has been to employ a multivariate, supervised classification in which the metrics are derived from univariate analyses. This enables us to carefully examine each metric for both population as well as individual sample relevance. While unsupervised clustering approaches provide good insight into spectral similarity, a supervised method forces a relation to common clinical knowledge. For example, as shown in Fig. 4 for prostate tissue, we consider a ten-class model to determine histology. The drawback is that the sensitivity of the approach to individual samples is lost at the expense of generality. One could potentially combine clustering and supervised classification. Clustering information on the training data set would emphasize individual sample distributions, which would allow for supervised classification tailored to each cluster type. Such an approach has not been implemented yet but is being attempted in our laboratories to classify samples optimally.

#### Dimensionality reduction

It is well recognized that the spectrum at each pixel needs to be reduced to a smaller set of useful descriptors that capture the essential information inherent in the spectrum. The reduction of full spectral information to essential measures helps eliminate from consideration those spectral features that have no information (non-absorbing frequen-

cies), little biochemical significance (e.g., apparent absorption at non-chemically specific frequencies), inconsistent measures that may degrade classification, and those with redundant information. The number of useful measures is significantly smaller than the number spectral resolution elements and, hence, the process is also termed dimensionality reduction. Dimensionality reduction and further refinement (*vide infra*) also helps reduce the incidence of prediction by chance alone, reduce computation time and storage requirements. Potential measures of a spectrum's useful features are termed metrics and are defined manually in our scheme.

It may be argued that the metrics are not selected in an objective manner due to a human performing this task and some computer routines must be employed. While the use of an automated computer program is most certainly objective and reproducible, the algorithm that drives such programs is generated from spectroscopy knowledge. A well-trained spectroscopist can recognize spectral features and assign them to appropriate their biochemical basis. While a computer algorithm may be able to enhance subtle features in the spectrum, automated peak-picking algorithms run the risk of substantial error as they are based on some very specific criteria that may not be universally valid. We believe that computer algorithms are more suited to finding correlations and patterns that a human cannot for the sheer size and complexity of data. Hence, the process of determining which spectral features to consider is entirely manual in our approach. It must be emphasized that the universal set of metrics is selected manually but that the data reduction step to a set of metrics to be used in algorithms is entirely based on objective algorithms. Manual refinement of metrics for classification is, obviously, not recommended for possibilities of overlooking specific features, biasing the selection to specific feature sets, or in determining the optimal set of metrics for a classifier. Dimensionality reduction is also intimately linked to the data quality and classification algorithm employed.

#### Classification algorithm

A number of supervised algorithms have been applied to dimensionally reduced data, including those based on linear discriminant analysis, neural networks, decision trees, and modified Bayesian Classifiers. An intermediate step in some of these algorithms provides for a fuzzy result in which every pixel has a probability of belonging to every class. For example, in our approach, each pixel can have a probability (between zero and one) of belonging to each class. A discriminant function then assigns each pixel to a class based on a decision rule. The pre-discriminant data set, termed rule imaging set, contains important information. In our algorithm, it is a direct measure of the

probability of the pixel belonging to the class. Hence, the probability value may be used to compare the potential of two protocols to distinguish a cell type or to quantify confidence in results for tissue classified by different methods.

#### *Measures of accuracy and optimization*

We prefer the use of the AUC for both optimizing algorithms and for validating results. Confidence in the value of the AUC, hence, is the primary test for the validity of developed algorithms and is characterized by the standard error of the value. For example, in validating the discrimination of epithelial from stromal pixels in a blinded validation set, the cumulative distribution of AUC in a TMA is shown in Fig. 8. More than 20% of the spots had an AUC >95% and no AUC value below 0.8 was recorded. One drawback of using ROC curves and AUC values is that the results are valid for one at a time classification. Hence, we have analyzed here the segmentation of epithelium from all other cell types. The tissue is classified into ten classes as before but the results are lumped into epithelial and non-epithelial pixels. Further, not all TMA cores have all types of cells. Hence, the two-class model also allows us to examine a large number of samples. Last, we excluded cores that did not contain at least 100 pixels of each class to leave 103 cores for the analysis.

Quantitative measures of performance and accuracy are perhaps the weakest portion of reports using IR spectroscopy for cancer pathology. Typically, sensitivity and specificity have been employed as summary measures. While these are indeed very relevant, we demonstrate that they are insufficient and classification analysis must utilize more measures to understand the process. Specifically, the use of

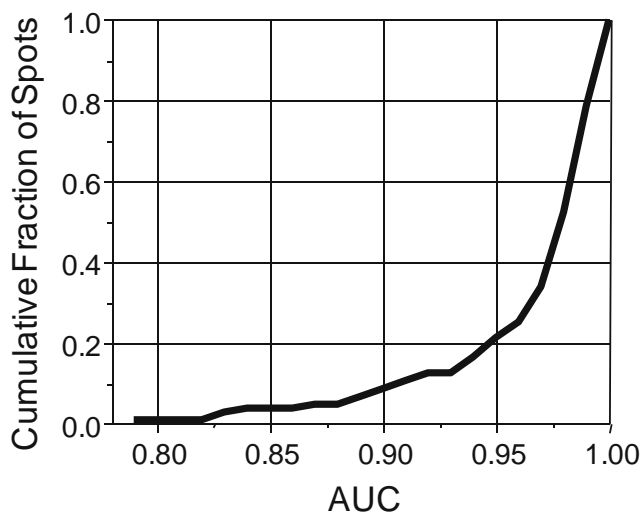


**Fig. 8** Distribution of AUC values in a TMA for discriminating epithelium from stroma using the ten-class model

receiver operating characteristic (ROC) curves [71] is an excellent direction. The area under the ROC curve is a further summary measure that provides both a quantitative understanding of the discrimination potential of the model and a convenient measure to compare multiple classification models. The third tool we introduced was the confusion matrix. While ROC curves provide the potential for correct classification of a binary rule at a time, confusion matrices correspond to a particular point on the ROC curve under the constraints of accuracy measures of other classes. These also directly correspond to the final segmentation of the rule image under an optimization condition. The optimization condition may simply be the maximization of the accuracy or may be the minimization of certain types of errors.

#### *Discriminant and class assignment*

In a multi-class analysis, our approach to evaluating ROC curves for a class is one at a time, i.e., all other classes are essentially lumped in the rule data and the highest probability of the lumped ensemble is compared to the class whose ROC curve is being built. Hence, the AUC values must be regarded as a potential for classification. They are best suited to answer the binary question of whether a pixel is correctly identified or not when considering a single class. This method is ideally suited to a cascaded classifier one at a time. Such a classifier has not been reported yet but would provide a means to explicitly determine the error for any given classification scheme.

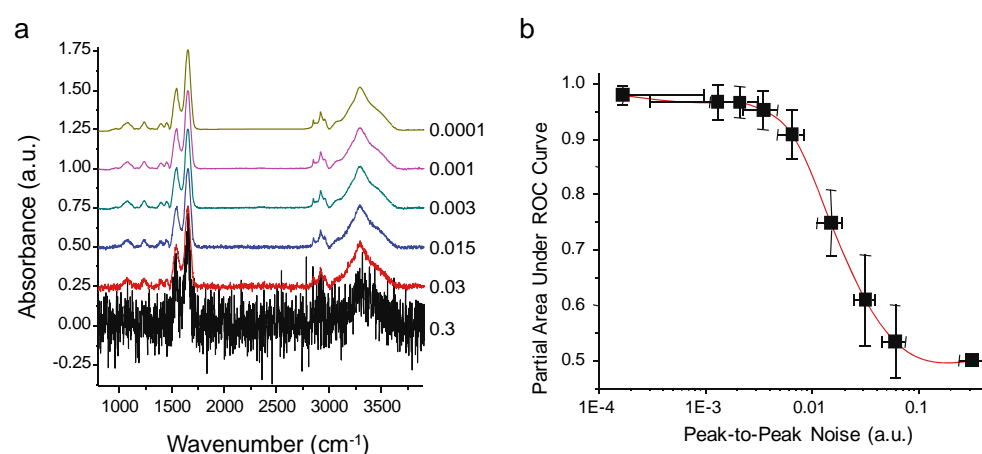
#### **Experimental parameters and classification**

Here, we take advantage of the trading rules of FTIR spectroscopy and imaging to model the effects of the experimental parameters on the classification process. While the signal to noise ratio (SNR) and resolution are generally arbitrarily fixed in most studies, we demonstrate their importance in classification.

##### *Effect of signal to noise ratio*

There are two issues: what is the “best” SNR to formulate algorithms and second, provided an algorithm, what is the least SNR that would provide adequate classification. Only the latter issue is examined here. As with conventional FTIR spectrometers, imaging spectrometers obey the trading rules of IR spectroscopy. Hence, if an  $n$ -fold reduction in SNR provides the same results, data acquisition will be  $n^2$ -fold faster. Thus, in addition to an interesting fundamental behavior of the classifier, the role of SNR has a direct bearing on the speed at which data is acquired.

**Fig. 9** **a** Noise in the data set as a function of added random noise. **b** Effect of spectral noise on the accuracy of classification as measured by AUC values



We examined classification accuracy as a function of average spectral noise. To strictly examine the effect of noise, data must be acquired at different co-added spectral numbers. The time required for imaging an array multiple times, however, is prohibitive. Hence, we computationally added random, Gaussian noise to the original spectral data. Peak-to-peak and root mean square (rms) noise were measured in the 1,950- to 2,150- $\text{cm}^{-1}$  region adjacent to the amide I peak.<sup>2</sup> Representative single pixel spectra from the data sets are shown, as a function of noise, in Fig. 9a. We additionally plotted the observed noise levels against the added noise to verify linearity (plot not shown). The linear relationship conforms to the expected result and provides a scaling factor to express the equivalent reduction in data acquisition time (co-addition) that would be realized at that noise level. For example, the addition of 0.005 a.u. of noise raises the peak-to-peak noise from 0.0013 to 0.015 a.u., corresponding to a decrease in data acquisition time by a factor of ca. 100 for this data set. In addition to increasing noise, we employed an algorithm based on an MNF transform [72, 73] to mathematically eliminate noise. The observed peak-to-peak noise was 0.00017 a.u., corresponding to an increase in data acquisition time by a factor greater than ca. 100. Hence, the data examined span about 5 orders in magnitude of collection time.

The average height of the amide I peak was 0.42 a.u. in all cases, providing a SNR of 2,500 (MNF-corrected data) to 1.5 for the data sets. Accuracy as a function of the noise level is shown in Fig. 9b. While the x-error bars indicate the standard deviation of noise levels in pixels, the y-error bars indicate the standard deviation in AUC values of all ten

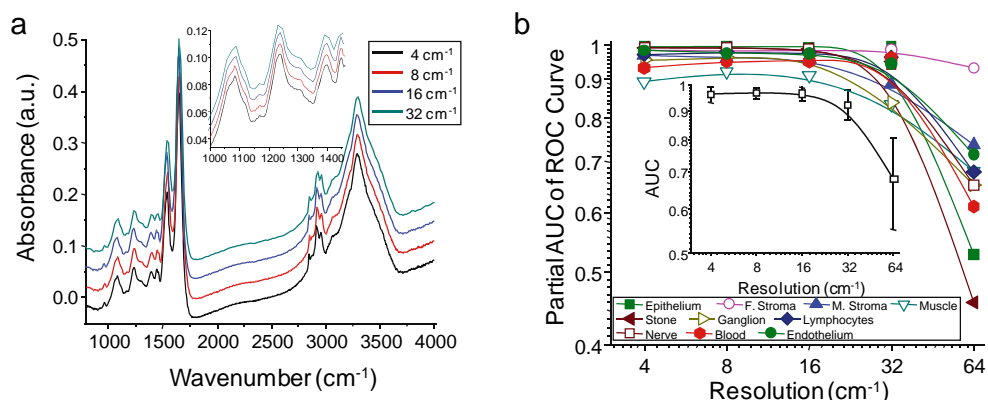
classes. As a general rule, the classification improves with lower noise levels. We first note that the classification does not become perfect for any noise level and there is a significantly diminishing return in increasing the SNR beyond a level. At the other end, the ability to distinguish classes is entirely lost at levels of ca. 0.1. Performance across multiple data sets observed using our prediction model indicates that the increases demonstrated at noise levels lower than ca. 0.003 a.u. are within the variance. Hence, there is little benefit to decreasing the noise levels below ca. 0.003 a.u. for this data set, or to increasing the SNR beyond ca. 150. It must be emphasized that the model, prediction algorithm, and discriminant function are intimately linked in a non-linear manner. While this makes it impossible to predict the behavior generally of all classification approaches, this simple exercise may be conducted to determine the optimal data acquisition parameters. For our selected metrics and model, it appears that the data acquisition time can be decreased by a factor of ca. 3 without significant degradation in accuracy.

#### Spectral resolution

We next examined the effect of spectral resolution on the results that would be obtained using the developed algorithm. As in the previous section, the data were not re-acquired but were downsampled from acquired data using a neighbor binning procedure. Spectra from the same epithelial class pixel, at different resolutions (Fig. 10a), demonstrate the effect of downsampling on feature definition. Figure 10b demonstrates, first, that the peak-to-peak noise levels over the region remain the same with spectral resolution. As previously observed, noise is an important control in comparing spectra; the peak-to-peak noise over the same number of data points was preserved by neighbor binning. In practice, the constant-throughput spectrometer would provide a SNR (or noise level, in this case) that decreases linearly with resolution. Since most array

<sup>2</sup> It is noteworthy that we are examining trends in the absorbance spectra. Strictly, SNR should be measured in single beam spectra to relate rigorously to theory. It can be shown, however, that the trend will hold approximately for the absorbance spectra as well. Many practitioners advocate the use of rms SNR. We are employing peak-to-peak fluctuations over the same spectral range. Hence, the noise values we obtain will be higher but will follow the same trend.

**Fig. 10** **a** Spectra obtained by downsampling acquired data to different resolutions using a neighbor binning procedure. The inset demonstrates the effect of resolution on narrower features in the spectrum. **b** AUC values for each class and average AUC values as a function of spectral resolution demonstrate a decrease only for coarse spectral resolution



detectors can be operated with higher integration times, it is fair to assume that the time advantage in decreasing resolution would be linear. Second, the performance of the classifier is very nearly the same for finer spectral resolutions and degrades only significantly for  $32\text{ cm}^{-1}$ . While the results may appear to be surprising, a closer analysis of the basis of the algorithms provides insight into the trends.

The classifier is based on absorbance and center of gravity measures of the peaks. It is well established that absorbance is measured accurately, provided that the FWHH of the peak is not significantly smaller than the resolution. The Ramsay resolution parameter,  $\sigma$ , is a useful measure that was originally developed for monochromators but has been shown to be applicable to FTIR spectrometers as well [74]. While most bands are broad and peak absorbance lower than ca. 0.7, absorbance values are not expected to be adversely impacted from the measurement process. With decreasing resolution, however, broadening within complex peaks shapes may lead to observed changes in the apparent absorption at a specific wavenumber. The change itself may not have a significant influence on the classifier performance as it depends on several such metrics. A second type of metric calculates the area under the curve. This is not expected to be impacted significantly for most peaks. The third type of metric we have used is the center of gravity of a spectral region. While spectral analyses ordinarily attempt to locate the peak position and use it as a metric, we chose the center of gravity for its sensitivity to both position and asymmetrical shape changes in complex spectral envelopes observed in biological samples. Since the classifier is based on center of gravity of a feature and not on the wavenumber of the peak maximum, it is a very robust measure that is relatively unaffected by spectral resolution or noise.

#### Generalization of developed algorithms to instruments and practical approaches

The characterization of classification with regard to spectrometer performance (SNR) and spectral resolution

provides information to optimize parameters on one spectrometer. It is unclear, however, if the calibration would transfer to another spectrometer. We contend that the potential for a successful transfer is high as the classification process is relatively insensitive to resolution, implying that it would only be weakly sensitive to apodization or to small inaccuracies in wavelength scale. Similarly, if the SNR of acquired data is used as control, perturbations due to fixed pattern noise in focal plane array detectors or the different use of electronic filters by different manufacturers is likely to be insignificant in classifying tissue correctly. Various instrument manufacturers also set the nominal optical resolution differently in their instruments. The issue of spatial resolution, of course, is more complex. Nevertheless, any resolution setting around the wavelength-limited case will likely provide consistent results. To our knowledge, there has been no comparison yet of classifier performance across mid-IR FTIR imaging spectrometers using algorithms developed on one specific instrument. The developed protocol provides for such a framework and detailed results are awaited from on-going work [75].

#### Outlook and prospects

An exciting period in imaging tissues spectroscopically with low power, optical microscopy-comparable resolution is emerging. Considerable work, however, needs to be accomplished before this idea can become a clinical reality. An ultimate goal of such studies is to provide a key technology for emerging molecular pathology. The approach promises greatly reduced error rates, automation, and economic benefits in current pathology practice. Looking to the future, chemical imaging approaches will be employed for diagnosing cancers in pre-malignant stages prior to their apparent changes observable by conventional means, predicting the prognosis of the lesion and intraoperative imaging in real-time. Fundamental studies in drug discovery and mechanisms of molecular interactions are further examples that would be enabled by progress in this

area. Doubtless, exciting applications lie ahead and progress is rapidly being made towards practical applications but much work needs to be done to carefully apply this powerful technology to multiple aspects of pathology. Success in this endeavor promises to change the practice of pathology radically and alter the clinical management of cancer patients.

**Acknowledgement** The author would like to acknowledge collaborators over the years, especially Dr. Stephen M. Hewitt and Dr. Ira W. Levin of the National Institutes of Health, for numerous useful discussions and guidance. Discussions and help from Dr. Daniel Fernandez during the formative years of this work are also appreciated. Funding for this work was provided in part by University of Illinois Research Board and by the Department of Defense Prostate Cancer Research Program. This work was also funded in part by the National Center for Supercomputing Applications and the University of Illinois, under the auspices of the NCSA/UIUC faculty fellows program.

## References

- Woolf SH (1995) *N Engl J Med* 333:1401–1405
- Humphrey PA (2003) Prostate pathology. American Society for Clinical Pathology, Chicago
- Partin AW, Mangold LA, Lamm DM, Walsh PC, Epstein JI, Pearson JD (2001) *Urology* 58:843–848
- De La Taille A, Viellefond A, Berger N, Boucher E, De Fromont M, Fondimare A, Molinié V, Piron D, Sibony M, Staroz F, Triller M, Peltier E, Thiouarn N, Rubin MA (2003) *Hum Pathol* 34:444–449
- Levin IW, Bhargava R (2005) *Annu Rev Phys Chem* 56:429–474
- Navratil M, Mabbott GA, Arriaga EA (2006) *Anal Chem* 78:4005–4019
- Caprioli RM, Farmer TB, Gile J (1997) *Anal Chem* 69:4751–4760
- Chaurand P, Schwartz SA, Billheimer D, Xu BGJ, Crecelius A, Caprioli RM (2004) *Anal Chem* 76:1145–1155
- Kurhanewicz J, Vigneron DB, Hricak H, Narayan P, Carroll P, Nelson S (1996) *Radiology* 198:795–805
- Lewis EN, Gorbach AM, Marcott C, Levin IW (1996) *Appl Spec* 50:263–269
- Diem M, Romeo M, Boydston-White S, Miljkovic M, Matthaus C (2004) *Analyst* 129:880–885
- Mendelsohn R, Paschalas EP, Boskey AL (1999) *J Biomed Opt* 4:14–21
- Kidder LH, Kalasinsky VF, Luke JL, Levin IW, Lewis EN (1997) *Nat Medicine* 3:235–237
- Ellis DI, Goodacre R (2006) *Analyst* 131:875–885
- Bhargava R, Levin IW (eds) (2005) Spectrochemical analysis using infrared multichannel detectors. Blackwell, Oxford
- Petrush W (2001) *Appl Spectrosc Rev* 36(2):181–237
- Andrus PG (2006) *Tech Cancer Res Treat* 5:157–167
- Krafft C, Sergo V (2006) *Spectroscopy* 20:195–218
- Petibois C, Deleris G (2006) *Trends Biotechnol* 24:455–462
- Walsh MJ, German MJ, Singh M, Pollock HM, Hammiche A, Kyrgiou M, Stringfellow HF, Paraskevaidis E, Martin-Hirsh PL, Martin FL (2007) *Cancer Lett* 246:1–11
- Keith FN, Bhargava R (2007) *Tech Cancer Res Treat* (submitted)
- Gazi E, Dwyer J, Gardner P, Ghanbari-Siakhali A, Wade AP, Myan J, Lockyer NP, Vickerman JC, Clarke NW, Shanks JH, Hart C, Brown M (2003) *J Pathology* 201:99–108
- Gazi E, Baker M, Dwyer J, Lockyer NP, Gardner P, Shanks JH, Reeve RS, Hart C, Clarke NW, Brown M (2006) *Eur Urol* 50:750–761
- Harvey TJ, Henderson A, Gazi E, Clarke NW, Brown M, Faria EC, Snook RD, Gardner P (2007) *Analyst* 132:292–295
- Paluszewicz C, Kwiatek WM, Banas A, Kisiel A, Marcelli A, Piccinini A (2007) *Vib Spectrosc* 43:237–242
- Fernandez DC, Bhargava R, Hewitt SM, Levin IW (2005) *Nat Biotechnol* 23:469–474
- German MJ, Hammiche A, Ragavan N, Tobin MJ, Cooper LJ, Matanhelia SS, Hindley AC, Nicholson CM, Fullwood NJ, Pollock HM, Martin FL (2006) *Biophys J* 90:3783–3795
- Gazi E, Dwyer J, Lockyer NP, Myan J, Gardner P, Hart CA, Brown MD, Clarke NW (2005) *Vib Spectrosc* 38:193–201
- Bhargava R, Hewitt SM, Levin IW (2007) *Nat Biotechnol* 25:31–33
- Srinivasan G, Bhargava R (2007) *Spectroscopy* 22:30–43
- Bhargava R, Fernandez DC, Hewitt SM, Levin IW (2006) *Biochim Biophys Acta Biomembr* 1758:830–845
- Swets JA (1988) *Science* 240:1285–1293
- Lasch P, Naumann D (2006) *Biochim Biophys Acta* 1758:814–829
- Jackson M, Choo LP, Watson PH, Halliday WC, Mantsch HH (1995) *Biochim Biophys Acta* 1270:1–6
- Sommer AJ, Katon JE (1991) *Appl Spectrosc* 45:1633–1640
- Carr GL (2001) *Rev Sci Inst* 72:1613–1619
- Bhargava R, Wang SQ, Koenig JL (1998) *Appl Spectrosc* 52:323–328
- Budevska BO (2000) *Vib Spectrosc* 24:37–45
- Romeo M, Diem M (2005) *Vib Spectrosc* 38:129–132
- Jackson M (2004) *Faraday Discuss* 126:1–18
- Norris KP (1954) *J Sci Inst* 31:284–287
- Rousch PB (ed) (1985) The design, sample handling, and applications of infrared microscopes. ASTM STP 949, American Society for Testing and Materials, Philadelphia
- Kwiatkoski JM, Reffner JA (1987) *Nature* 328:837–838
- Koenig JL (1999) Spectroscopy of polymers, 2nd edn. Elsevier, New York
- Bartik EG, Tungol MW, Reffner JA (1994) *Anal Chim Acta* 288:35–42
- Wetzel DA, LeVine SM (1999) *Science* 285:1224–1225
- Gremlich H-U, Yan B (eds) (2000) Infrared and Raman spectroscopy of biological materials (practical spectroscopy). Marcel Dekker, New York
- Bhargava R, Wall BG, Koenig JL (2000) *Appl Spectrosc* 54:470–474
- Vobornik D, Margaritondo G, Sanghera JS, Thielen P, Aggarwal ID, Ivanov B, Miller JK, Haglund R, Tolk NH, Congiu-Castellano A, Rizzo MA, Piston DW, Somma F, Baldacchini G, Bonfigli F, Marolo T, Flora F, Montereali RM, Faenov A, Pikuz T, Longo G, Mussi V, Generosi R, Luce M, Perfetti P, Cricenti A (2004) *Infrared Phys Tech* 45:409–416
- Hirschfeld T (1979) *Appl Spectrosc* 33:525–527
- Wetzel DL (2002) *Vib Spectrosc* 29:183–189
- Carter MR, Bennett CL, Fields DJ, Hernandez J (1995) *Proc SPIE* 2480:380–386
- Lewis EN, Treado PJ, Reeder RC, Story GM, Dowrey AE, Marcott C, Levin IW (1995) *Anal Chem* 67:3377–3381
- Colarusso P, Kidder LH, Levin IW, Fraser JC, Arens JF, Lewis EN (1998) *Appl Spectrosc* 52:106A–120A
- Snively CM, Koenig JL (1999) *Appl Spectrosc* 53:170–177
- Bhargava R, Levin IW (2001) *Anal Chem* 73:5157–5167
- Ransohoff DF (2004) *Nat Rev Cancer* 4:309–314
- Bhargava R, Levin IW (eds) (2005) Spectrochemical analysis using infrared multichannel detectors. Blackwell, Oxford, pp 56–84
- Various contributors (2006) *Biochim Biophys Acta Biomembr* 1758

60. Wood BR, Chiriboga L, Yee H, Quinn MA, McNaughton D, Diem M (2004) *Gynecol Oncol* 93:59–68
61. Malins DC, Polissar NL, Nishikida K, Holmes EH, Gardner HS, Gunselman SJ (1995) *Cancer* 75:503–517
62. Boydston-White S, Gopen T, Houser S, Bargonetti J, Diem M (1999) *Biospectroscopy* 5:219–227
63. Shaw RA, Guijon FB, Paraskevas V, Ying SL, Mantsch HH (1999) *Anal Quant Cytol* 21:292–302
64. Mansfield JR, McIntosh LM, Crowson AN, Mantsch, HH, Jackson, M (1999) *Appl Spectrosc* 53:1323–1333
65. McIntosh LM, Jackson M, Mantsch HH, Stranc MF, Pilavdzic D, Crowson AN (1999) *J Invest Dermatol* 112:951–956
66. Kononen J, Bubendorf L, Kallioniemi A, Barlund M, Schraml P, Leighton S, Torhorst J, Mihatsch MJ, Sauter G, Kallioniemi OP (1998) *Nat Med* 4:844–847
67. Camp RL, Charette LA, Rimm DL (2000) *Lab Invest* 80:1943–1949
68. Paluszakiewicz C, Kwiatek WM, Banas A, Kisiel A, Marcelli A, Piccinini M (2007) *Vib Spectrosc* 43(1):237–242
69. Benjamini Y, Hochberg Y (1995) *J R Stat Soc Ser B* 57:289–300
70. Pawitan Y, Michiels S, Koscielny S, Gusnanto A, Ploner A (2005) *Bioinformatics* 21:3017–3024
71. Stone N, Kendall C, Smith J, Crow P, Barr H (2004) *Faraday Diss* 126:141–157
72. Bhargava R, Wang SQ, Koenig JL (2000) *Appl Spectrosc* 54:486–495
73. Bhargava R, Wang SQ, Koenig JL (2000) *Appl Spectrosc* 54:1690–1706
74. Anderson RJ, Griffiths PR (1975) *Anal Chem* 47:2339–2347
75. Llora X, Reddy RK, Bhargava R (in preparation)

# Observer-invariant histopathology using genetics-based machine learning

Xavier Llorà · Anusha Priya · Rohit Bhargava

© Springer Science+Business Media B.V. 2007

**Abstract** Prostate cancer accounts for one-third of noncutaneous cancers diagnosed in US men and is a leading cause of cancer-related death. Advances in Fourier transform infrared spectroscopic imaging now provide very large data sets describing both the structural and local chemical properties of cells within prostate tissue. Uniting spectroscopic imaging data and computer-aided diagnoses (CADx), our long term goal is to provide a new approach to pathology by automating the recognition of cancer in complex tissue. The first step toward the creation of such CADx tools requires mechanisms for automatically learning to classify tissue types—a key step on the diagnosis process. Here we demonstrate that genetics-based machine learning (GBML) can be used to approach such a problem. However, to efficiently analyze this problem there is a need to develop efficient and scalable GBML implementations that are able to process very large data sets. In this paper, we propose and validate an efficient GBML technique—NAX—based on an incremental genetics-based rule learner. NAX exploits massive parallelisms via the message passing interface (MPI) and efficient rule-matching using hardware-implemented operations. Results demonstrate that NAX is capable of performing prostate tissue classification efficiently, making a compelling case for using GBML implementations as efficient and powerful tools for biomedical image processing.

---

X. Llorà (✉)

National Center for Supercomputing Applications, University of Illinois at Urbana-Champaign,

1205 W. Clark Street, Urbana, IL 61801, USA

e-mail: xllora@uiuc.edu

A. Priya · R. Bhargava

Department of Bioengineering, University of Illinois at Urbana-Champaign, 1304 W. Springfield Ave., Urbana, IL 61801, USA

A. Priya

e-mail: priya@uiuc.edu

R. Bhargava

e-mail: rxb@uiuc.edu

R. Bhargava

Beckman Institute for Advanced Science and Technology, University of Illinois at Urbana-Champaign, 405 N. Mathews Ave., Urbana, IL 61801, USA

**Keywords** Observer-invariant histopathology · Genetics-based machine learning · Learning Classifier Systems · Hardware acceleration · Vector instruction · SSE2 · MPI · Massive parallelism

## 1 Introduction

Pathologist opinion of structures in stained tissue is the definitive diagnosis for almost all cancers and provides critical input for therapy. In particular, prostate cancer accounts for one-third of noncutaneous cancers diagnosed in US men. Hence, it is, appropriately, the subject of heightened public awareness and widespread screening. If prostate-specific antigen (PSA) or digital rectal screens are abnormal, a biopsy is needed to definitively detect or rule out cancer. Pathologic status of biopsied tissue not only forms the definitive diagnosis but constitutes an important cornerstone of therapy and prognosis. There is, however, a need to add useful information to diagnoses and to introduce new technologies that allow economical cancer detection to focus limited healthcare resources. In pathology practice, widespread screening results in a large workload of biopsied men, in turn, placing a increasing demand on services. Operator fatigue is well documented and guidelines limit the workload and rate of examination of samples by a single operator. Importantly, newly detected cancers are increasingly moderate grade tumors in which pathologist opinion variation complicates decision-making.

For the reasons above, there is an urgent need for automated and objective pathology tools. We have sought to address these requirements through novel Fourier transform infrared (FTIR) spectroscopy-based, computer-aided diagnoses for prostate cancer and develop the required microscopy and software tools to enable its application. FTIR spectroscopic imaging is a new technique that combines the spatial specificity of optical microscopy and the biochemical content of spectroscopy. As opposed to thermal infrared imaging, FTIR imaging measures the absorption properties of tissue through a spectrum consisting of (typically) 1024–2048 wavelength elements per pixel. Since IR spectra reflect the molecular composition of the tissue, image contrast arises from differences in endogenous chemical species. As opposed to visible microscopy of stained tissue that requires a human eye to detect changes, numerical computation is required to extract information from IR spectra of unstained tissue. Extracted information, based on a computer algorithm, is inherently objective and automated (Lattouf and Saad 2002; Fernandez et al. 2005; Levin and Bhargava 2005; Bhargava et al. 2006).

Uniting spectroscopic imaging data and computer-aided diagnoses (CADx), we seek to provide a new approach to pathology by automating the recognition of cancer in complex tissue. This is an exciting paradigm in which disease diagnoses are objective and reproducible; yet do not require any specialized reagents or human intervention. The first step toward the creation of such CADx tools requires mechanisms for reliable and automated tissue type classification. In this paper we demonstrate how genetics-based machine learning tools can achieve such a goal. Interpretability of the learned models and efficient processing of very large data sets have lead us to rule-based models—easy to interpret—and genetics-based machine learning—inherent massively parallel methods with the required scalability properties to address very large data sets. We present the method and the efficiency enhancement techniques proposed to address automated tissues classification. When pushed beyond the relatively small problems traditionally used to test such methods, an need for efficient and scalable implementations becomes a key research topic

that needs to be addressed. We designed the proposed a technique with such constraints in mind. A modified version of an incremental genetics-based rule learner that exploits massive parallelisms—via the message passing interface (MPI)—and efficient rule-matching using hardware-oriented operations. We name this system NAX. NAX is compared to traditional and genetics-based machine learning techniques on an array of publicly available data sets. We also report the initial results achieved using the proposed technique when classifying prostate tissue.

The remainder of the paper is structured as follows. We present an overview of the problem addressed in Sect. 2, paying special attention to tissue classification. We discuss in Sect. 3 the hurdles that traditional genetics-based machine learning implementations face when applied to very large data sets. Section 4 presents our solution to those hurdles. We also describe the incremental rule learner proposed for tissue classification. Last, we summarize results on publicly-available data sets and the preliminary results for tissue classification on a prostate tissue microarray in Sect. 5. Finally, in Sect. 6, we present conclusions and further work.

## 2 Biomedical imaging and data mining

This section presents an overview of the problem addressed in this paper. We first introduce infrared spectroscopic imaging as a potentially powerful tool for cancer diagnosis and prognosis. Then, we explore the protocols that provide raw high-quality data that for data mining. Finally, we conclude by focusing on the key task, tissue classification, by focusing on prostate tissue.

### 2.1 Infrared spectroscopy and imaging for cancer diagnosis and prognosis

Infrared spectroscopy is a well-established molecular technique and is widely used in chemical analyses. The fundamental principle governing the response of any material is that the vibrational modes of molecules are resonant in energy with photons in the mid-infrared region (2–14 mm) of the electromagnetic spectrum. Hence, when photons of energy that are resonant with the material’s molecular composition are incident, a number are absorbed. The number absorbed is directly proportion to the number of chemical species that are excited. Hence, any material has a characteristic frequency-dependent absorption profile called a spectrum. An infrared spectrum is often termed the “optical fingerprint” of a material as it can help uniquely identify molecular composition—see Fig. 1.

Researchers, including us, have contributed to develop an imaging version of spectroscopy that is essentially similar to an optical microscope. In this mode of spectroscopy, images are acquired in the manner of optical microscopy with one important difference. Instead of measuring the intensity of three colors for a visible image, several thousand intensity values are acquired at each pixel in the image as a function of wavelength (spectrum at each pixel). The resulting data set is three dimensional (2 spatial and 1 spectral indices) consisting typically of a size  $256 \times 256 \times 1024$ , but extending to sizes such as  $3500 \times 3500 \times 2048$ . Since each data point is stored as a 16-bit number, the data size typically runs into several tens to hundreds of gigabytes.

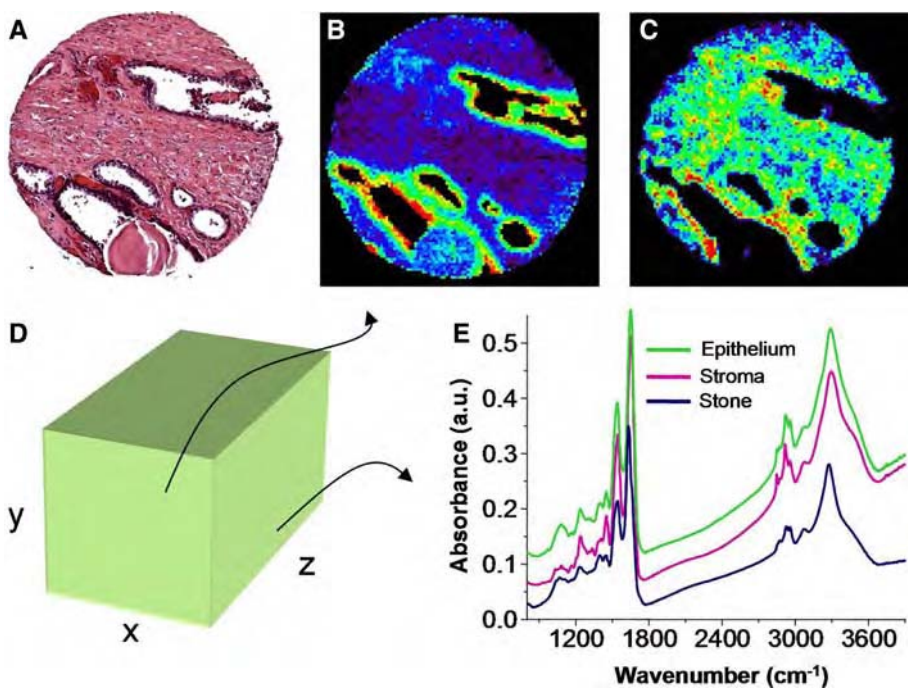


**Fig. 1** Conventional staining and automated recognition by chemical imaging. (A) Typical H&E stained sample, in which structures are deduced from experience by a human. Highlights of specific regions in the manner of H&E is possible using FTIR imaging without stains. (B) Absorption at  $1080\text{ cm}^{-1}$  commonly attributed to nucleic acids and (C) to proteins of the stroma. The data obtained is 3 dimensional (D) from which spectra (E) or images at specific spectral features may be plotted

## 2.2 Mining the spectra: Two sequential problems

Though the continued development of fast FTIR microspectroscopy represents an exciting opportunity for pathology, handling the resultant data and rapidly providing classifications remains a critical challenge. First, the sheer volume of data—potentially larger than 10 GB a day—represents an organizational and retrieval challenge. Next, extraction of useful information in short time periods requires the formulation of optimal protocols. Third, the automated cancer segmentation problem is very complex and offers a number of routes and levels of data that need to be analyzed to determine the optimal approach for application in a laboratory.

The typical application is the need to extract information from the data set such that it is clinically relevant. Hence, the output of the data mining algorithm to be developed is well-bounded and clearly defined. For example, in the prostate there are two levels of interest. In the first level, the pathologist examines the tissue to determine if there are any epithelial cells. Since more than 95% of prostate cancers arise in epithelial cells, transformations in this class of cells forms the diagnostic basis and a primary determinant of therapy. Other cell types of interest are lymphocytes that may indicate inflammation, blood vessel density that may indicate the development of new blood supply indicative of cancer growth and nerves that may be invaded by cancer cells. Hence, any automated approach to pathology must first identify cell types accurately. The second step in pathology follows. Once

epithelial cells are located, their spatial patterns are indicative of disease states. In our imaging approach, we can identify both spatial patterns as well as chemical patterns in epithelial cells. Hence, the task would be to use either or both to classify disease. In this paper, we focus only on the accurate identification/classification of tissue types as the first step of the path that leads to obtaining the correct pixels of epithelium.

### 2.3 Tissue classification for prostate arrays

Prostate tissue is structurally complex, consisting primarily of glandular ducts lined by epithelial cells and supported by heterogeneous stroma. This tissue also contains blood vessels, blood, nerves, ganglion cells, lymphocytes and stones (which are comprised of luminal secretions of cellular debris) that organize into structures measuring from tens to hundreds of microns. These structures are readily observable within stained tissue using bright-field microscopy at low to medium magnifications. Hence, in applying FTIR imaging (Levin and Bhargava 2005), we obtain the common structural detail employed clinically and, additionally, spectral information indicative of tissue biochemistry. As histologic classes contain identical chemical components, infrared vibrational spectra are similar but reveal small differences in specific absorbance features. The technique proposed by Fernandez et al. (2005) examines each cell types' spectra and transforms each spectrum into a vector of describing features—usually around the hundreds. A complete description of this process is beyond the scope of this paper and can be found elsewhere (Fernandez et al. 2005). Each pixel (cell present in the slice of micro array under analysis) has an assigned spatial position in the array while the tissue type is assigned by a highly experienced pathologist. Thus, the tissue classification can be cast into a supervised classification problem (Mitchell 1997), where all the attributes are real-valued and the class is the tissue type—ten classes: *epithelium, fibrous stroma, mixed stroma, muscle, stone, lymphocytes, endothelium, nerve, ganglion, and blood*. Figure 2 presents tissue types that can be assigned by examining a stained image obtained, after the FTIR microspectroscopy on unstained tissue, by the pathologist. Each marked pixel in the image becomes a training example; hence, the usual smallest data set is around hundreds of thousand records per array.

## 3 Larger, bigger, and faster genetics-based machine learning

Bernadó et al. (2001) presented a first empirical comparison between genetics-based machine learning techniques (GBML) and traditional machine learning approaches. The authors reported that GBML techniques were as competent as traditional techniques. Later, Bacardit and Butz (2006) repeated the analysis, obtaining similar results. Most of the experiments presented on both papers used publicly available data sets provided by the *University of California at Irvine* repository (Merz and Murphy 1998). Most of the data sets are defined over tens of features and up to few thousands of records—in the larger cases. However, a key property of GBML approaches is its intrinsic massive parallelism and scalability properties. Cantú-Paz (2000) presented how efficient and accurate genetics algorithms could be assembled, and Llorà (2002) presented how such algorithms can be efficiently used for machine learning and data mining. However, there are elements that need to be revisited when we want to efficiently apply GBML techniques to large data sets such as the one described in the previous section.

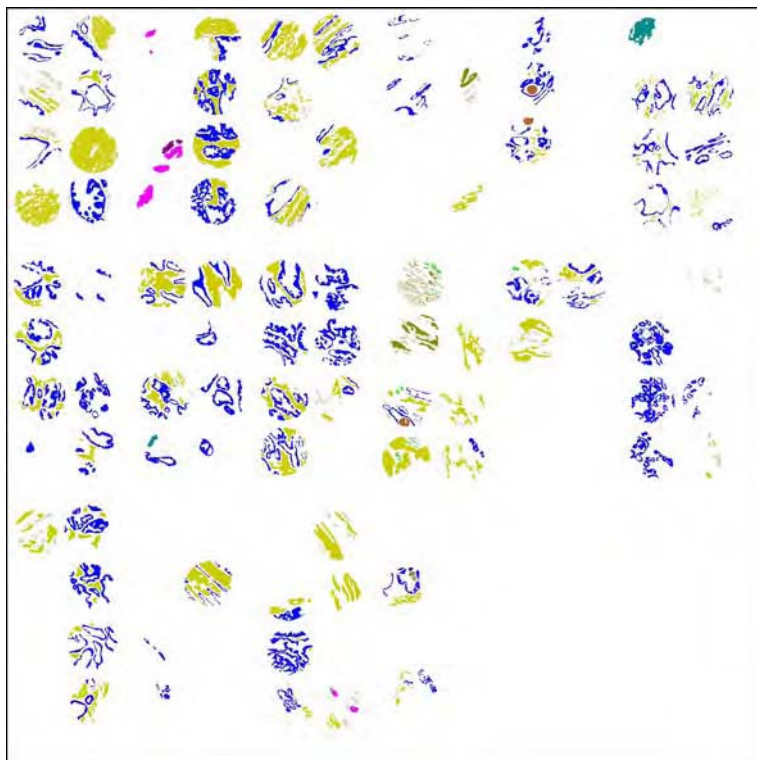


**Fig. 2** The figure presents the tissue labeling provided by a pathologist biopsy section of human prostate tissue. Each spot represents the section of a needle. Different colors represent different tissue types

The GBML techniques require evaluating candidate solutions against the original data set matching the candidate solutions (e.g., rules, decision trees, prototypes) against all the instances in the data set. Regardless of the flavor used, Llorà and Sastry (2006) showed that, as the problem grows, rule matching governs the execution time. For small data sets (teens of attributes and few thousands of records) the matching process takes more than 85% of the overall execution time marginalizing the contribution of the other genetic operators. This number increases to 98% and above, when we move to data sets with few hundreds of attributes and few hundred thousands of records. More than 98% of the time is spent evaluating candidate solutions. Each evaluation can be computed in parallel. Moreover, the evaluation process may also be parallelized on very large data sets by splitting and distributing the data across the computational resources. A detailed description of the parallelization alternatives of GBML techniques can be found elsewhere (Llorà 2002).

Currently available off-the-shelf GBML methods and software distributions (Barry and Drugowitsch 1997; Llorà 2006) do not usually target large data sets. The two main bottlenecks are large memory footprints and sequential-processing oriented processes. Generally speaking, they were designed to run on single processor machines with enough memory to fit the entire data set. Hence, designers did not pay much

attention to the memory footprint required to store the data set—usually completely loaded into memory and the population of candidate solutions. These large complex structures were geared to facilitate the programming effort, but they are not designed toward the efficient evaluation of the candidate solutions. However, efforts have been made to push GBML methods into domains which require processing large data sets. Three different works need to be mentioned here. Flockhart (1995) proposed and implemented GA-MINER, one of the earliest effort to create data mining systems based on GBML systems that scale across symmetric multi-processors and massively parallel multi-processors. Flockhart (1995) reviewed different encoding and parallelization schemes and conducted proper scalability studies. Llorà (2002) explored how fine-grained parallel genetic algorithms could become efficient models for data mining. Theoretical analysis of performance and scalability were developed and validated with proper simulations. Recently, Llorà and Sastry (2006) explored how current hardware can efficiently speed up rule matching against large data sets. These three approaches are the basis of the incremental rule learning proposed in the next section to approach very large data sets.

Another important issue in real-world problems is the class distribution. Usually most real problems have a clear class imbalance. Recently, Orriols-Puig and Bernadó-Mansilla (2006) have revisited this issue, showing how GBML techniques successfully learn and maintain proper descriptions for those minority classes. If not designed properly, descriptions of majority classes will tend to govern the learned models, starving the description of minority classes. Prostate tissue classification is a clear example of extreme class imbalance. Figure 3 presents the tissue type class distribution. The smaller tissue type has 64 records, where as the larger classes have several tens of thousands records. hence, the developed approaches must account for class size variation.

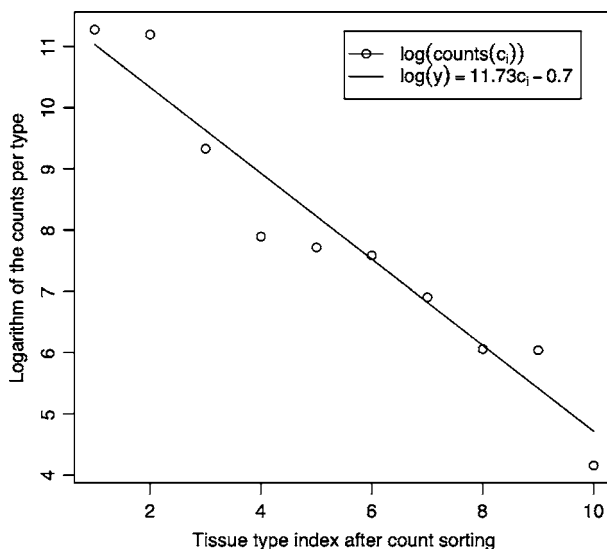


**Fig. 3** Figure shows the tissue class distribution. Once the classes are reordered according to their frequency in the data set, we can easily appreciate the extreme imbalance—the smaller tissue type has 64 records, where as the larger classes have several tens of thousands records

## 4 The road to tractability

We describe in this section the steps we took to design a GBML method (NAX) able to deal with very large data sets with class imbalance. NAX evolves, one at a time, maximally general and maximally accurate rules. Then, the covered instances are removed and another maximally general and maximally general rule is evolved and added to the previously stored one forming a decision list. This process continues until no uncovered instances are left—this process is also referred as the sequential covering procedure (Cordón et al. 2001). Llorà et al. (2005) showed that maximally general and maximally accurate rules (Wilson 1995) could also be evolved using Pittsburgh-style Learning Classifier Systems. Later, Llorà et al. (2007) showed that competent genetic algorithms (Goldberg 2002) evolve such rules quickly, reliably, and accurately. The rest of this section describes (1) efficient implementation techniques to deal with very large data sets, (2) the impact of class imbalance, and (3) the NAX algorithm proposed.

### 4.1 Efficient implementations

As introduced earlier, when dealing with very large data sets, and regardless of the flavor of the GBML technique used, we may spend up to 98% of the computational cycles trying to match rules to the original data set (Llorà and Sastry 2006). Each solution evaluation is independent of each other and, hence, it can be computed in parallel. Moreover, even the matching nature of a rule—the representation we will use from now on—is highly parallel, since conditions require performing simultaneous checks against different attributes per record. Thus, efficient implementation can take advantage of parallelizing both elements.

#### 4.1.1 Exploiting the hardware acceleration

Recently, multimedia and scientific applications have pushed CPU manufacturers to include support for vector instructions again in their processors. Both applications areas require heavy calculations based on vector arithmetic. Simple vector operations such as *add* or *product* are repeated over and over. During 1980s and 1990s supercomputers, such as Cray machines, were able to issue hardware instructions that enabled basic vector arithmetics. A more constrained scheme, however, has made its way into general-purpose processors thanks to the push of multimedia and scientific applications. Main chip manufacturers—IBM, Intel, and AMD—have introduced vector instruction sets—AltiVec, SSE3, and 3DNow<sup>+</sup>—that allow vector operations over packs of 128 bits by hardware. We will focus on a subset of instructions that are able to deal with floating point vectors. This subset of instructions manipulate groups of four floating-point numbers. These instructions are the basis of the fast rule matching mechanism proposed.

Our goal is to evolve a set of rules that correctly classifies the current data set from prostate tissue. Using a knowledge representation based on rules allows us to inspect the learned model, gaining insight into the biological problem as well. All the attributes of the domain are real-value and the conditions of the rules need to be able to express conditions in a  $\mathbb{R}^n$  spaces. We use a similar rule encoding to the one proposed by Wilson (2000b)—a variation of the original work proposed by Wilson (2000a) and later reviewed by Stone and Bull (2003)—and widely used in the GBML community. Rules express the conjunction of tests across attributes. Each test may be defined in multiple flavors but, without loss of

generality, we picked a simple interval based one. A simple example of an *if-then* rule, could be expressed as follows:

$$1.0 \leq a_0 \leq 2.3 \wedge \dots \wedge 10.0 \leq a_n \leq 23 \rightarrow c_1 \quad (1)$$

Where the condition is the conjunction of the different attribute tests and the outcome is the predicted class—a tissue type. We also allow a special condition—don't care—which just always returns `true`, allowing condition generalization. The rule below illustrates an example of a generalized rule.

$$1.0 \leq a_0 \leq 2.3 \wedge -3.0 \leq a_3 \leq 2 \longrightarrow c_1 \quad (2)$$

All attributes except  $a_0$  and  $a_3$  were marked as don't care.

Each condition can be encoded using 2 floating-point numbers per condition, where  $\alpha_i$  contains the lower bound of the condition and  $\omega_i$  its upper bound. Thus, the condition  $\alpha_i \leq a_0 \leq \omega_i$  just requires to store the two floating-point numbers. For efficiency reasons we store them in two separate vectors, one containing the lower bounds and the other containing the upper bounds. The position in a vector indicates the attribute being tested. The don't care condition is simply encoded as  $\alpha_i > \omega_i$  and, hence, we do not need to store any extra information.

Matching a rule requires performing the individual condition tests before the final *and* operation can be computed. Vector instruction sets improve the performance of this process by performing four operations at once. Actually, this process may be regarded as four parallel running pipelines. The process can be further improved by stopping the matching process when one test fails—since that will turn the condition into false.

Figure 4 presents a C implementation the proposed hardware-supported rule matching. The code assumes that the two vectors containing the upper and lower bounds are provided and records are stored in a two dimensional matrix. Figure 5 presents the vectorized implementation of the code presented in Fig. 4 using SSE2 instructions. Exploiting the hardware available can speed between 3 and 3.5 times the matching process, as also shown elsewhere (Llorà and Sastry 2006).

#### 4.1.2 Massive parallelism

Since most of the time is spent on the evaluation of candidate rules when dealing with large data sets, our next goal was to find a parallelization model that could take advantage of this peculiarity. Due the quasi embarrassing parallel (Grama et al. 2003) nature of the candidate rule evaluation, we designed a coarse-grain parallel model for distributing the evaluation load. Cantú-Paz (2000) proposed several schemes, showing the importance of the trade-off between computation time and time spent communicating. When designing the parallel model, we focused on minimizing the communication cost. Usually, a feasible solution could be a master/slave one—the computation time is much larger than the communication time. However, GBML approaches tend to use rather large populations, forcing us to send rule sets to the evaluation slaves and collect the resulting fitness. These schemes also increment the sequential sections that cannot be parallelized, threatening the overall speedup of the parallel implementation as a result of Amdahl law (Amdahl 1967).

To minimize such communication cost, each processor runs an identical NAX algorithm. They are all seeded in the same manner, hence, performing the same genetic operations and only differing in the portion of the population being evaluated. Thus, the population is

---

```

1. void match_seq_rule_set ( RuleSet * rs, InstanceSet is, int iDim, int iRows ) {
2.     int i,j,k,iCnt,iClsIdx,iGround,iPred;
3.     register int iMatchable;
4.     Instance ins;
5.
6.     iClsIdx = rs->iCorrectedDim;
7.     clean_fitness_rules_set(rs);
8.     for ( i=0 ; i<iRows ; i++ ) {
9.         ins = is[i];
10.        iPred=-1;
11.        for ( j=0 ; iPred== -1 && j<rs->iLen ; j++ ) {
12.            iMatchable = 1;
13.            for ( iCnt=0,k=j*(rs->iCorrectedDim+VBSIF) ;
14.                  iMatchable && k<j*(rs->iCorrectedDim+VBSIF)+rs->iDim ;
15.                  k++,iCnt++ ) {
16.                iMatchable = iMatchable &&
17.                    !( (rs->pflB[k]<=rs->pfUB[k]) &&
18.                      ( ins[iCnt]<rs->pflB[k] || ins[iCnt]>rs->pfUB[k]));
19.            }
20.            if ( iMatchable )
21.                iPred = rs->pflB[j*(rs->iCorrectedDim+VBSIF)+rs->iCorrectedDim];
22.        }
23.        iPred = (iPred== -1)?rs->iClasses:iPred;
24.        iGround=(int)ins[iClsIdx];
25.        rs->pConfMat[iGround][iPred]++;
26.    }
27. }
```

---

**Fig. 4** This figure presents a sequential implementation of the rule matched process in C. A rule set is match against a data set. Lines 16, 17, and 18 implement the condition test for one attribute. The implementation also computes the confusion matrix that contains the ground truth versus predicted class

treated as collection of chunks where each processor evaluates its own assigned chunk, sharing the fitness of the individuals in its chunk with the rest of the processors. Fitness can be encapsulated and broadcasted maximizing the occupation of the underlying packing frames used by the network infrastructure. Moreover, this approach also removes the need for sending the actual rules back and forth between processors—as a master/slave approach would require—thus, minimizing the communication to the bare minimum—the fitness. Figure 6 presents a conceptual scheme of the parallel architecture of NAX.

To implement the model presented in Fig. 6, we used C and a *message passing interface* (MPI)—we used the OpenMPI implementation (Gabriel et al. 2004). Figure 7 shows the code in charge of the parallel evaluation. Each processor computes which individuals are assigned to it. Then it computes the fitness and, finally, it just broadcast the computed fitness. The rest of the process is left untouched, and besides the cooperative evaluation, all the processors end generating the same evolutionary trace.

#### 4.2 Rule sets as individuals

One main characteristic of the so-called Pittsburgh-style learning classifier systems—a particular type of GBML—is that individuals encode a rule set (Goldberg 1989; Llorà and Garrell 2001; Goldberg 2002). Thus, evolutionary mechanisms directly recombine one rule set against another one. For classification tasks of moderate complexity, the rule sets are

---

```

1. #define VEC_MATCH(vecFLB,fLB,vecFUB,fUB,vecINS,fIN,vecTmp,vecOne,vecRes) { \
2.     vecFLB = _mm_load_ps(fLB); \
3.     vecFUB = _mm_load_ps(fUB); \
4.     vecINS = _mm_load_ps(fIN); \
5.     \
6.     vecRes = (_mm128i)_mm_cmplt_ps(vecFUB,vecFLB); \
7.     vecTmp = _mm_or_si128( \
8.         (_mm128i)_mm_cmplt_ps(vecFLB,vecINS), \
9.         (_mm128i)_mm_cmplt_ps(vecINS,vecFUB) \
10.    ); \
11.    vecRes = _mm_andnot_si128(_mm_and_si128(vecRes,vecTmp),vecOne); \
12. }
13.
14. void match_rule_set ( RuleSet * rs, InstanceSet is, int iDim, int iRows ) {
15.     int i,j,k,iCnt,iClsIdx,iGround,iPred;
16.     register int iMatchable;
17.     Instance ins;
18.
19.     __m128i vecRes,vecTmp,vecOne;
20.     __m128 vecFLB,vecFUB,vecINS;
21.
22.     vecOne = (__m128i){-1,-1};
23.
24.     iClsIdx = rs->iCorrectedDim;
25.     clean_fitness_rules_set(rs);
26.     for ( i=0 ; i<iRows ; i++ ) {
27.         // Classify the instance
28.         ins = is[i];
29.         iPred=-1;
30.         for ( j=0 ; iPred== -1 && j<rs->iLen ; j++ ) {
31.             iMatchable = 1;
32.             for ( iCnt=0,k=j*(rs->iCorrectedDim+VBSIF) ;
33.                   iMatchable && k<j*(rs->iCorrectedDim+VBSIF)+rs->iDim ;
34.                   k+=VBSIF,iCnt+=VBSIF ) {
35.                 VEC_MATCH(vecFLB,&(rs->pfLB[k]),
36.                           vecFUB,&(rs->pfUB[k]),
37.                           vecINS,&(ins[iCnt]),vecTmp,vecOne,vecRes);
38.                 iMatchable = 0xFFFF==_mm_movemask_epi8(vecRes);
39.             }
40.             if ( iMatchable )
41.                 iPred = rs->pfLB[j*(rs->iCorrectedDim+VBSIF)+rs->iCorrectedDim];
42.             iPred = (iPred== -1)?rs->iClasses:iPred;
43.             iGround=(int)ins[iClsIdx];
44.             rs->pConfMat[iGround][iPred]++;
45.         }
46.     }

```

---

**Fig. 5** This figure presents a vectorized implementation of the rule matching process presented in Fig. 4. Lines 1–12 implement the parallelized test against four attributes using vector instructions. The code is written using C intrinsics for SSE2 compatible architectures. This code runs on P4 or newer Intel processors and Opteron or Athlon 64 AMD processors

not large. However, for complex problems, the potential number of required rules to ensure proper classification may need large amounts of memory that become prohibitive. The requirements increase even further in the presence of noise (Llorà and Goldberg 2003).

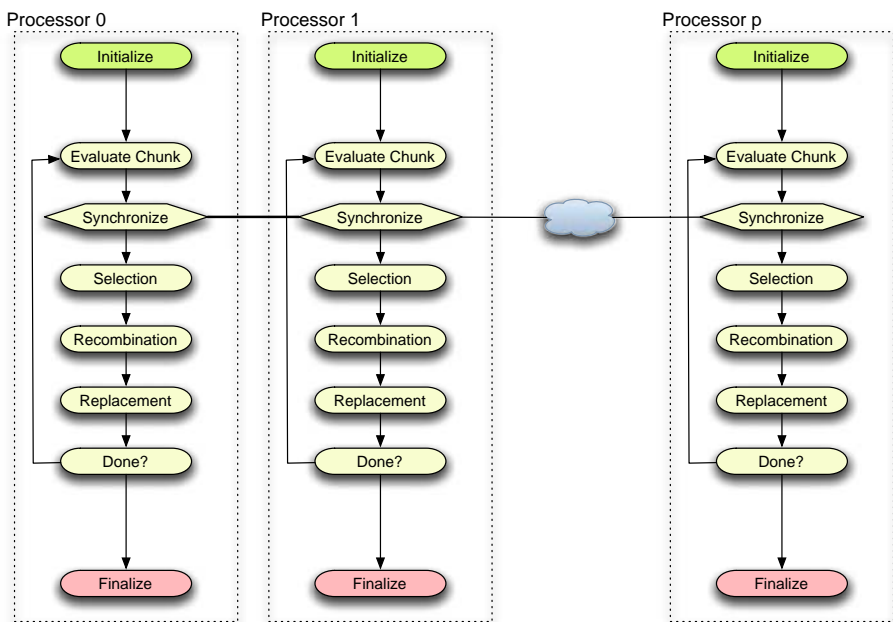


**Fig. 6** This figure illustrates the parallel model implemented. Each processor is running the same identical NAX algorithm. They only differ in the portion of the population being evaluated. The population is treated as collection of chunks where each processor evaluates its own assigned chunks sharing the fitness of these individuals with the rest of the processors. This approach minimizes the communication cost

Parallelization may not help much if we need to send large rule sets across the communication network. For such reasons, GBML techniques work very well on moderate complexity problems (Bernadó et al. 2001; Bacardit and Butz 2006). However, they need to be modified to deal with complex and large data set, and also avoid the boundaries imposed by the issues mentioned above.

#### 4.3 NAX: Incremental rule learning for very large data sets

An incremental rule learning approach may alleviate memory footprint requirements by evolving only one rule at a time, hence, reducing the memory requirements. However, one rule by itself cannot solve complex problems. For such a reason, each evolved rule is added to the final rule set, and the covered examples are removed from the current training set. The process is repeated until no instances are left in the training set. This approach already introduced by Cordón et al. (2001) and later also used by Bacardit and Krasnogor (2006) allows maintaining relatively small memory footprints, making feasible processing large data sets—as the prostate tissue classification data set. However, an incremental approach to the construction of the rule set requires paying special attention to the way rules are evolved. For each run of the genetic algorithm used to evolve a rule, we would like to obtain a maximally general and maximally accurate rule, that is, a rule that covers the maximum number of example without making mistakes (Wilson 1995).

---

```

1. void evaluate_population ( Population * pp, InstanceSet is, int iDim, int iRows )
2. {
3.     int i;
4.
5.     /* Compute the fragments of this processor */
6.     int iFrag = pp->iLen/FCS_processes;
7.     int iInit = FCS_process_id*iFrag;
8.     int iLast = (FCS_process_id+1==FCS_processes)?
9.                 pp->iLen:
10.                (FCS_process_id+1)*iFrag;
11.    int iCnt = 0;
12.    int j,k,l;
13.
14.    /* Create the bucket for the broadcast */
15.    float faFit[2*iFrag];
16.    float faTmp[2*iFrag];
17.
18.    /* Evaluate the given chunk assigned to the processor */
19.    for ( i=iInit,iCnt=0 ; i<iLast ; i++,iCnt++ ) {
20.        match_rule_set(pp->prs[i],is,iDim,iRows );
21.        compute_raw_accuracy_fitness_rule_set(pp->prs[i]);
22.        faFit[iCnt] = pp->prs[i]->fFitness;
23.    }
24.
25.    /* Broadcast each of the chunks */
26.    for ( i=0 ; i<FCS_processes ; i++ ) {
27.        MPI_Bcast((i==FCS_process_id)?faFit:faTmp,iCnt,MPI_FLOAT,i,MPI_COMM_WORLD);
28.        if ( i!=FCS_process_id )
29.            for ( l=0,j=i*iFrag, k=(i+1)*iFrag ; j<k ; j++,l++ )
30.                pp->prs[j]->fFitness = faTmp[l];
31.    }
32. }
```

---

**Fig. 7** This figure presents an implementation of the proposed parallel evaluation scheme using C and MPI. The piece of code presented below is the only one modified to provide such parallelization capabilities. Each processor computes which individuals are assigned to it (lines 6–10), then it computes the fitness (lines 10–23), and then it just broadcast the computed fitness (lines 26–31)

Llorà et al. (2007) have shown that evolving such rules is possible. In order to promote maximally general and maximally accurate rules à la XCS (Wilson 1995), we compute the *accuracy* ( $\alpha$ ) and the *error* ( $\varepsilon$ ) of a rule (Llorà et al. 2005). The *accuracy* is the proportion of overall examples correctly classified, and the *error* is the proportion of incorrect classifications issued. For simplicity reasons, we use the proportion of correctly issued classifications instead, simplifying the final fitness calculation. Let  $n_{t+}$  be the number of positive examples correctly classified,  $n_{t-}$  the number of negative examples correctly classified,  $n_m$  the number of times a rule has been matched, and  $n_t$  the number of examples available. Using these values, the *accuracy* and *error* of a rule  $r$  can be computed as:

$$\alpha(r) = \frac{n_{t+}(r) + n_{t-}(r)}{n_t} \quad (3)$$

$$\varepsilon(r) = \frac{n_{t+}(r)}{n_m(r)} \quad (4)$$

Once the *accuracy* and *error* of a rule are known, the fitness can be computed as follows.

$$f(r) = \alpha(r) \cdot \varepsilon(r)^\gamma \quad (5)$$

where  $\gamma$  is the error penalization coefficient. The above fitness measure favors rules with a good classification accuracy and a low error, or maximally general and maximally accurate rules. By increasing  $\gamma$ , we can bias the search towards correct rules. This is an important element because assembling a rule set based on accurate rules guarantees the overall performance of the assembled rule set. In our experiments, we have set  $\gamma$  to 18 to strongly bias the search toward maximally general and maximally accurate rules.

NAX's efficient implementation of the evolutionary process is based on the techniques described using hardware acceleration—Sect. 4.1.1—and coarse-grain parallelism—Sect. 4.1.2. The genetic algorithm used was a modified version of the *simple genetic algorithm* (Goldberg 1989) using tournament selection ( $s = 4$ ), one point crossover, and mutation based on generating new random boundary elements.

## 5 Experiments

This section present the results achieved using NAX. To allow the reader to compare with other techniques, we compare the results obtained using NAX on small data sets provided by the UCI repository (Merz and Murphy 1998) to other well-known supervised learning algorithms. Finally, we present the first results on the prostate tissue prediction obtained using NAX. Results focus on the viability of the NAX approach.

### 5.1 Some UCI repository data sets

The UCI repository (Merz and Murphy 1998) provides several data sets for different machine learning problems. These data sets have been widely used to test traditional machine learning and GBML techniques. Table 1 list the data sets used. Due to the nature of the prostate tissue type classification, we only chose data sets with numeric attributes. Three of these data sets are of relevant interest: (1) *son*, by far the one with larger dimensionality, (2) *gls*, the one with large number of classes, (3) *tao*, proposed by Llorà and Garrell (2001), having complex and non-linear boundaries.

**Table 1** Summary of the data sets used in the experiments

ID	Data set	Size	Missing values(%)	Numeric attributes	Nominal attributes	Classes
bre	<i>Wisconsin Breast Cancer</i>	699	0.3	9	–	2
bpa	<i>Bupa Liver Disorders</i>	345	0.0	6	–	2
gls	<i>Glass</i>	214	0.0	9	–	6
h-s	<i>Heart Stats-Log</i>	270	0.0	13	–	2
ion	<i>Ionosphere</i>	351	0.0	34	–	2
irs	<i>Iris</i>	150	0.0	4	–	3
son	<i>Sonar</i>	208	0.0	60	–	2
tao	<i>Tao</i>	1888	0.0	2	–	2
win	<i>Wine</i>	178	0.0	13	–	3

**Table 2** Experimental results: percentage of correct classifications and standard deviation from stratified ten-fold cross-validation runs

ID	0-R	C4.5	NAX
bre	65.52 ± 1.16	95.42 ± 1.69	96.43 ± 1.72
bpa	57.97 ± 1.23	65.70 ± 3.84	64.07 ± 8.36
gls	35.51 ± 4.49	65.89 ± 10.47	68.02 ± 8.69
h – s	55.55 ± 0.00	76.30 ± 5.85	75.56 ± 9.39
ion	64.10 ± 1.19	89.74 ± 5.23	89.19 ± 5.27
irs	33.33 ± 0.00	95.33 ± 3.26	94.67 ± 4.98
son	53.37 ± 3.78	71.15 ± 8.54	73.62 ± 9.72
tao	49.79 ± 0.17	95.07 ± 2.11	97.41 ± 0.92
win	39.89 ± 3.22	93.82 ± 2.85	94.34 ± 6.09

Paired *t*-test comparisons showed no statistically significant differences between C4.5 and NAX results  
0-R result are just provided as guiding base line

We could have chosen complex algorithms as baselines for NAX . However, we would not be able to use them to repeat the experimentation on the prostate tissue classification domain. The algorithms used in the comparison presented in Table 2 were 0-R (Holte 1993) (a simple base line based on majority class classification) and C4.5 (Quinlan 1993). Results show percentage of correct classifications and standard deviation from stratified ten-fold cross-validation runs. Paired *t*-test comparisons showed no statistically significant differences between the pruned tree produced by C4.5 and NAX results. This experiments also helped validate the distributed implementation proposed by NAX. Further results on empirical comparisons can be found elsewhere (Bernadó et al. 2001; Bacardit and Butz 2006).

## 5.2 Prostate tissue classification

With the previous results at hand, we ran NAX against the prostate tissue classification data set. The original data set is defined by 93 attributes. In this paper, however, we used the reduced version of this data set proposed by (Fernandez et al. 2005) which contains 20 selected attributes out of the 93 available. The dataset is form by 171,314 records. Our goal was to explore how well NAX could generalize over unseen tissue—this is the first step to be able to address the cancer prediction problem. The other reason that motivated such experimentation was to achieve similar accuracy results as the ones published earlier by Fernandez et al. (2005) using a modified Bayes technique. If NAX could perform at the same level, we will also obtain a set of rules of interest to the spectroscopist. The interpretation of the rules will provide insight on how to interpret the models provided by NAX —which could not be done with the models early used by Fernandez et al. (2005).

We conducted stratified 10-fold cross-validation experiments to measure the generalization capabilities of NAX for this problem. Since the problem was rather small—larger data set are being prepared to be run at the supercomputing facilities provided by the National Center for Supercomputing Applications—we run the ten-fold cross-validation runs in a 3GHz dual core Pentium D computer with 4 GB of RAM. NAX took advantage of the hardware support to speedup the matching process and uses two MPI processes to parallelize—as introduced in Fig. 6—the evaluation of the overall population. Each fold

took about one hour to complete, with the entire classification lasting less than half a day. We conducted a simple test of adding a second computer with an identical configuration. The overall time for cross-validation was reduced to half. Rough estimates—which will better measured when larger experiments are conducted on NCSA super computers—show that the sequential portion is around 1:1000 for this small data set. Numbers get better as data set increases, which demonstrates that we will be able to process very large data sets and efficiently exploit larger numbers of processors.

We proposed another measure of effectiveness, namely how many records can be processed per second. Using a single processor with the hardware acceleration mechanisms built into NAX, and the evolved rule set formed by 1,028 rules, the average throughput was around 60,000 records per second. For the prostate tissue classification, it took less than three seconds to classify the entire data set. Once the rule set is learnt, the classification problem falls again into the category of embarrassingly parallel problems (Grama et al. 2003). Since no communication is needed, the speedup grows linearly with the number of processors added—with the proper rule set replication and data set chunking. Thus, with the dual core box used we were able to just double the throughput (120,000 records per second) by chunking the data set and use both processors.

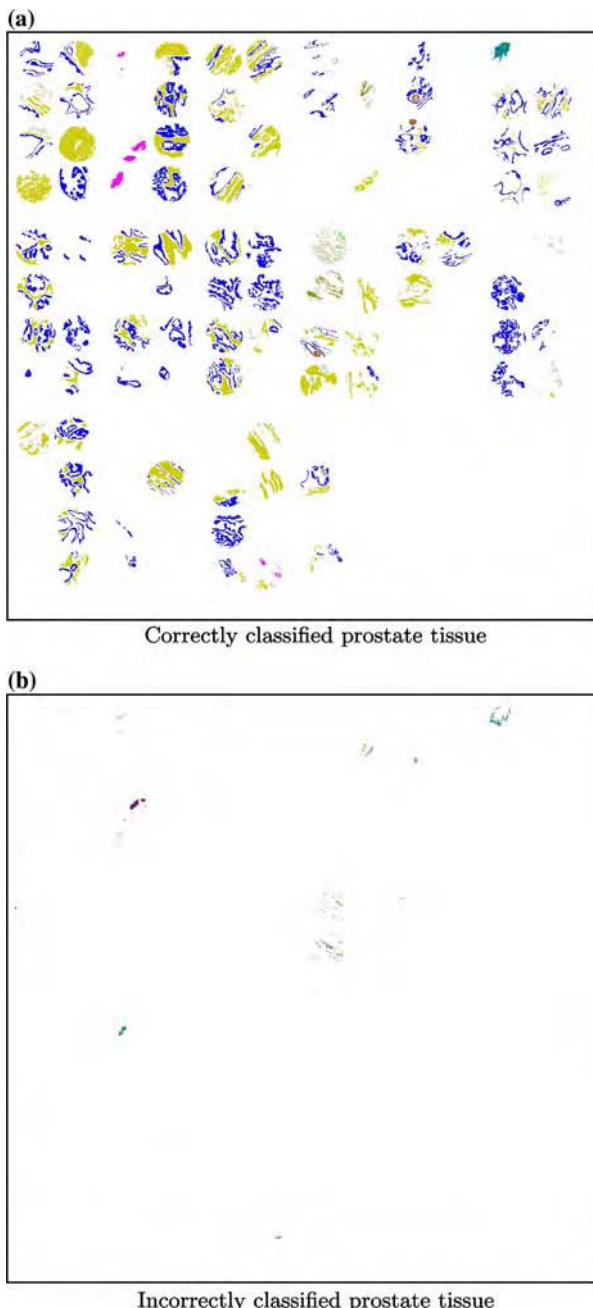
The previous results show the benefits of hardware acceleration and parallelization, but NAX was also able to achieve very competitive classification accuracy in generalization, correctly classifying  $97.09 \pm 0.09$  of the records (pixels) during the stratified ten-fold cross-validation. Figure 8 presents the regenerated prostate tissue classification image presented in Fig. 2 using a rule set assembled by NAX. Figure 8a presents the incorrectly classified pixels. Most of the mistakes by the rule set involve similar tissues with few training records available. This trend was also shown elsewhere (Fernandez et al. 2005). C4.5 does not provide any statistically significant improvement (only a marginal, not statistically significant, 0.7%) and provided large decision trees with more than 5,000 leaves—not to mention the lack of scalability when compared to NAX.

The rule set assembled by NAX represents an incremental assembling of maximally general and maximally accurate rules. Thus, we can compute how the accuracy of such ensemble improves as new rules are added. Figure 9 presents the overall accuracy as rules are added. It shows an interesting behavior for classifying prostate tissue. Using only 20 rules out of the 1,028 evolved ones, the overall accuracy is 90%, the incorrectly classified 1.3% pixels, and 8.7% were left unclassified. After inspecting the misclassified pixels most of them belongs to borders between tissues and mislabeling arises from the image discretization—one pixel containing different tissue types. Table 3 presents the initial four rules that covering 80% of the instances belonging to the two larger tissue types—epithelium and fibrous stroma. Such results are relevant, not only for their accuracy, but also because of the insight they provide to the spectroscopist about the problem structure.

## 6 Conclusions and further work

This paper has presented the initial results achieved in predicting prostate tissue type using GBML techniques. Being able to classify unseen tissue quickly, reliably, and accurately, is the first step towards the creation of CADx systems that may assist a pathologist diagnosing prostate cancer. We have proposed two main efficiency enhancement techniques for GBML—exploiting hardware parallelization via vector instructions and coarse-grain parallelism via the usage of MPI libraries—which allowed us to approach very large data sets. These techniques, together with an incremental genetics-based rule learning approach to

**Fig. 8** The figures presented above show the regenerated prostate tissue classification image presented in Fig. 2. (a) presents the correctly classified pixels. (b) presents the incorrectly classified pixels



assemble rule sets formed by maximally general and maximally accurate rules, have led to the creation of NAX, a system specialized on dealing with large data sets.

Results have shown accurate classification models for prostate tissue along with good scalability of the NAX implementation. Results also reveal peculiarities of the underlying problem structure. With very few rules—20—we were able to correctly classify up to 90%

**Fig. 9** The rule set as a decision list. The figure presents the classification accuracy as we keep adding rules to the decision list. The first 20 initial rules are able to cover 91% of the records with a classification accuracy of 98.5–90% overall accuracy presented in the figure

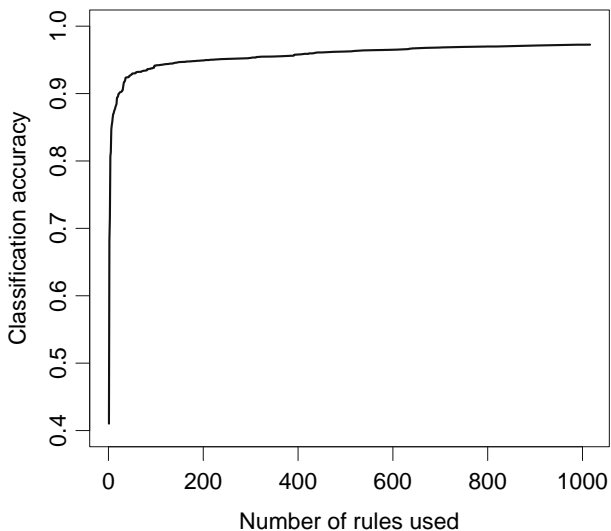


**Table 3** First top four maximally general and maximally accurate rules that compose the final rule set. The rule set is treated as a decision list, thus we can easily incrementally evaluate the value of the initial four ones

Rule	Rule condition	Tissue type	Accumulated accuracy (%)	Covered records (%)
1.	$0.10 \leq a_1 \leq 0.25 \wedge 0.00 \leq a_4 \leq 0.04 \wedge 1.07 \leq a_8 \leq 2.01 \wedge -0.07 \leq a_{16} \leq 0.16 \wedge 0.25 \leq a_{17} \leq 2.86 \wedge 0.11 \leq a_{18} \leq 0.21$	$\rightarrow Fibrous\ stroma$	41.32	41.96
2.	$0.03 \leq a_1 \leq 0.11 \wedge 0.05 \leq a_7 \leq 0.20 \wedge 1231.88 \leq a_{12} \leq 1247.90 \wedge 1.98 \leq a_{17} \leq 3.83 \wedge 0.13 \leq a_{18} \leq 0.20$	$\rightarrow Epithelium$	68.53	69.61
3.	$0.07 \leq a_0 \leq 0.16 \wedge 0.14 \leq a_1 \leq 0.41 \wedge 0.71 \leq a_{10} \leq 1.13 \wedge 1527.54 \leq a_{15} \leq 1533.80 \wedge 0.65 \leq a_{19} \leq 1.50$	$\rightarrow Fibrous\ stroma$	71.59	72.75
4.	$0.05 \leq a_2 \leq 0.09 \wedge 0.76 \leq a_4 \leq 1.29 \wedge 1.80 \leq a_6 \leq 2.08 \wedge 0.17 \leq a_7 \leq 0.24 \wedge 0.26 \leq a_{16} \leq 0.53 \wedge 2.79 \leq a_{17} \leq 7.01 \wedge 0.21 \leq a_{18} \leq 0.32$	$\rightarrow Epithelium$	80.78	82.08

of the tissue. Our current work is focused on analyzing the larger data sets containing all the available features and different tissue sources to test the parallelization scalability of NAX on NCSA supercomputers. Once accomplished, the procedure will provide confidence in creating a CADx system to generate a diagnosis based on the evolved models.

**Acknowledgments** We would like to thank David E. Goldberg for his continual support and encouragement, allowing us to have access to the IllIGAL resources. Thanks also to Kumara Sastry for hallway discussions and to the Automated Learning Group and the Data-Intensive Technologies and Applications at the National Center for Supercomputing Applications for hosting this joint collaboration. This work was sponsored by the Air Force Office of Scientific Research, Air Force Materiel Command, USAF, under grant

FA9550-06-1-0370, the National Science Foundation under grant IIS-02-09199, and the National Institute of Health. The US Government is authorized to reproduce and distribute reprints for Government purposes notwithstanding any copyright notation thereon. The views and conclusions contained herein are those of the authors and should not be interpreted as necessarily representing the official policies or endorsements, either expressed or implied, of the Air Force Office of Scientific Research, the National Science Foundation, or the US Government. Rohit Bhargava would like to acknowledge collaborators over the years, especially Dr. Stephen M. Hewitt and Dr. Ira W. Levin of the National Institutes of Health, for numerous useful discussions and guidance. Funding for this work was provided in part by University of Illinois Research Board and by the Department of Defense Prostate Cancer Research Program. This work was also funded in part by the National Center for Supercomputing Applications and the University of Illinois, under the auspices of the NCSA/UIUC faculty fellows program.

## References

Amdahl G (1967) Validity of the single processor approach to achieving large-scale computing capabilities. In Proceedings of the American federation of information processing societies conference (AFIPS). 30:483–485 AFIPS

Bacardit J, Butz M (2006) Advances at the frontier of Learning Classifier Systems. Chapter data mining in Learning Classifier Systems: Comparing XCS with GAssist, vol I. Springer

Bacardit J, Krasnogor N (2006) Biohel: Bioinformatics-oriented hierarchical evolutionary learning (Nottingham ePrints). University of Nottingham

Barry A, Drugowitsch J (1997) LCSWeb: the LCS wiki. <http://www.lcsweb.cs.bath.ac.uk/>

Bernadó E, Llorà X, Garrell J (2001) Advances in Learning Classifier Systems: 4th international workshop (IWLCS 2001). Chapter XCS and GALE: a comparative study of two Learning Classifier Systems with six other learning algorithms on classification tasks. Springer Berlin, Heidelberg, pp 115–132

Bhargava R, Fernandez D, Hewitt S, Levin I (2006) High throughput assessment of cells and tissues: Bayesian classification of spectral metrics from infrared vibrational spectroscopic imaging data. *Biochimica et Biophysica Acta* 1758(7):830–845

Cantú-Paz E (2000) Efficient and accurate parallel genetic algorithms. Kluwer Academic Publishers

Cordón O, Herrera F, Hoffmann F, Magdalena L (2001) Genetic fuzzy systems. Evolutionary tuning and learning of fuzzy knowledge bases. World Scientific

Fernandez D, Bhargava R, Hewitt S, Levin I (2005) Infrared spectroscopic imaging for histopathologic recognition. *Nat Biotechnol* 23(4):469–474

Flockhart I (1995) GA-MINER: parallel data mining with hierarchical genetic algorithms (final report). (Technical Report Technical Report EPCCAIKMS-GA-MINER-REPORT 1.0). University of Edinburgh

Gabriel E, Fagg G, Bosilca G, Angskun T, Dongarra J, Squyres J, Sahay V, Kambadur P, Barrett B, Lumsdaine A, Castain R, Daniel D, Graham R, Woodall T (2004) Open MPI: goals, concept, and design of a next generation MPI implementation. In Proceedings of the 11th European PVM/MPI Users' group meeting Springer

Goldberg D (1989) Genetic algorithms in search, optimization, and machine learning. Addison-Wesley Professional

Goldberg D (2002) The design of innovation: lessons from and for competent genetic algorithms. Springer

Grama A, Gupta A, Karypis G, Kumar V (2003) Introduction to parallel computing. Addison-Wesley

Holte R (1993) Very simple classification rules perform well on most commonly used datasets. *Mach Learn* 11:63–91

Lattouf J-B, Saad F (2002) Gleason score on biopsy: is it reliable for predicting the final grade on pathology? *BJU Int* 90:694–699

Levin I, Bhargava R (2005) Fourier transform infrared vibrational spectroscopic imaging: integrating microscopy and molecular recognition. *Annu Rev Phys Chem* 56: 429–474

Llorà X (2002) Genetics-based machine learning using fine-grained parallelism for data mining. Doctoral dissertation, Enginyeria i Arquitectura La Salle. Ramon Llull University, Barcelona, Catalonia, European Union

Llorà X (2006) Learning Classifier Systems and other genetics-based machine learning Blog. <http://www-illgal.ge.uiuc.edu/cs-n-gbml/>

Llorà X, Garrell J (2001) Knowledge-independent data mining with fine-grained parallel evolutionary algorithms. In Proceedings of the genetic and evolutionary computation conference (GECCO'2001). Morgan Kaufmann Publishers, pp 461–468

---

Llorà X, Goldberg D (2003) Bounding the effect of noise in multiobjective Learning Classifier Systems. *Evol Comput J* 11(3):279–298

Llorà X, Sastry K (2006) Fast rule matching for Learning Classifier Systems via vector instructions. In Proceedings of the 2006 genetic and evolutionary computation conference. ACM Press, pp 1513–1520

Llorà X, Sastry K, Goldberg D (2005) The compact classifier system: motivation, analysis and first results. In Proceedings of the congress on evolutionary computation, vol 1. IEEE press, (Also as IlliGAL TR No 2005019, pp 596–603)

Llorà X, Sastry K, Goldberg D, de la Ossa L (2007) The  $\chi$ -ary extended compact classifier system: linkage learning in Pittsburgh LCS. In Advances at the frontier of Learning Classifier Systems, vol II. IlliGAL report no 2006015. Springer, pp (in preparation)

Merz CJ, Murphy PM (1998) UCI repository for machine learning data-bases. <http://www.ics.uci.edu/~mlearn/MLRepository.html>

Mitchell T (1997) Machine learning. McGraw Hill

Orriols-Puig A, Bernadó-Mansilla E (2006) A further look at UCS classifier system. In Proceedings of the 8th annual conference on genetic and evolutionary computation workshop program. ACM Press

Quinlan JR (1993) C4.5: Programs for machine learning. Morgan Kaufmann

Stone C, Bull L (2003) For real! XCS with continuous-valued inputs. *Evol Comput J* 11(3):279–298

Wilson S (1995) Classifier fitness based on accuracy. *Evol Comput* 3(2):149–175

Wilson S (2000a) Get real! XCS with continuous-valued inputs. *Lect Notes Comput Sci* 1813:209–219

Wilson S (2000b) Mining oblique data with xcs. In Revised papers of the 3th international workshop on Learning Classifier Systems (IWLCS 2000). Springer, pp 158–176

# Towards Better than Human Capability in Diagnosing Prostate Cancer Using Infrared Spectroscopic Imaging

Xavier Llorà<sup>1</sup>, Rohith Reddy<sup>2,3</sup>, Brian Matesic<sup>2</sup>, and Rohit Bhargava<sup>2,3</sup>

<sup>1</sup>National Center for Super Computing Applications (NCSA)

<sup>2</sup>Department of Bioengineering

<sup>3</sup>Beckman Institute for Advanced Science and Technology

University of Illinois at Urbana-Champaign, Urbana IL 61801

xllora@uiuc.edu, rkreddy2@uiuc.edu, matesic2@uiuc.edu, rxb@uiuc.edu

## ABSTRACT

Cancer diagnosis is essentially a human task. Almost universally, the process requires the extraction of tissue (biopsy) and examination of its microstructure by a human. To improve diagnoses based on limited and inconsistent morphologic knowledge, a new approach has recently been proposed that uses molecular spectroscopic imaging to utilize microscopic chemical composition for diagnoses. In contrast to visible imaging, the approach results in very large data sets as each pixel contains the entire molecular vibrational spectroscopy data from all chemical species. Here, we propose data handling and analysis strategies to allow computer-based diagnosis of human prostate cancer by applying a novel genetics-based machine learning technique (NAX). We apply this technique to demonstrate both fast learning and accurate classification that, additionally, scales well with parallelization. Preliminary results demonstrate that this approach can improve current clinical practice in diagnosing prostate cancer.

## Categories & Subject Descriptors

I.2.6 [Artificial Intelligence]: Learning—Concept Learning.

I.5.4 [Pattern Recognition]: Applications.

J.3 [Life & Medical Science]: Medical Information Systems.

## General Terms

Algorithms, Design, Performance, Experimentation.

## Keywords

Genetics-Based Machine Learning, Learning Classifier Systems, Parallelization, Prostate Cancer.

Permission to make digital or hard copies of all or part of this work for personal or classroom use is granted without fee provided that copies are not made or distributed for profit or commercial advantage and that copies bear this notice and the full citation on the first page. To copy otherwise, to republish, to post on servers or to redistribute to lists, requires prior specific permission and/or a fee.

GECCO '07, July 7–11, 2007, London, England, United Kingdom.  
Copyright 2007 ACM 978-1-59593-697-4/07/0007 ...\$5.00.

## 1. INTRODUCTION

Pathologist opinion of structures in stained tissue is the definitive diagnosis for almost all cancers and provides critical input for therapy. In particular, prostate cancer accounts for one-third of noncutaneous cancers diagnosed in US men, and it is a leading cause of cancer-related death. Hence, it is, appropriately, the subject of heightened public awareness and widespread screening. If prostate-specific antigen (PSA) or digital rectal screens are abnormal, a biopsy is considered to detect or rule out cancer. Prostate tissue is extracted, or biopsied, from the patient and examined for structural alterations. The diagnosis procedure involves the removal of cells or tissues, staining them with dyes to provide visual contrast and examination under a microscope by a skilled person (pathologist).

The challenge in prostate cancer research and practice is to provide a novel Due to personnel, training, natural variability and biologic differences, the challenge in prostate cancer research and practice is to provide accurate, objective and reproducible decisions. Conventional optical microscopy followed by manual recognition has been demonstrated to be inadequate for this task. [18]. Hence, we have recently proposed developing a practical approach to this problem using chemical, rather than morphologic, imaging. [19]. In this approach, Fourier transform infrared imaging (FTIR) is employed to provide the entire vibrational spectroscopic information from every pixel of a sample's microscopy image. While the first steps of developing novel imaging and sampling technologies is now reliable, [7] the computational challenge of providing robust classification algorithms that can rapidly provide decisions remains. Due to the above advances in imaging and sampling, data from thousands of patients is available to train and validate algorithms for different disease states. While the application and type of data are unique, a further confounding factor required efficiently processing large volumes of data generated by FTIR imaging. The classification problem can be formulated as a supervised learning problem in which several million pixels (hundred of gigabytes) of accurately labeled data are available for model training and validation. The volume of tissue and (future) need for intra-operative diagnoses imply that rapid and accurate diagnoses are crucial to allow physicians to explore all possible courses of action. Under these conditions, traditional supervised learning ap-

proaches and implementations do not scale to provide diagnoses in an appropriate time frame. Hence, efficiently processing and learning models from gigabytes of FITR imaging data requires a careful design of the supervised learning algorithm. Moreover, the biological nature of the problem requires that such models be interpretable to provide fundamental new insight into the disease process. Genetics-based machine learning (GBML) techniques take advantage of the “*quasi embarrassing parallelism*” [17] to provide scaleable, fast, accurate, reliable, and interpretable models. In this paper we present an approach engineered to the desired solutiona and constraints of addressing this human task. A modified version of a sequential genetics-based rule learner that exploits massive parallelisms via the message passing interface (MPI) and efficient rule-matching using hardware-oriented operations is developed. We named this system NAX [24], and we have shown that its performance is comparable to traditional and genetics-based machine learning techniques on an array of publicly available data sets. We now show that NAX—taking advantage of both hardware and software parallelism—is able to provide prostate cancer diagnoses that are human-competitive. In this paper, we present preliminary results supporting this outcome.

The paper is structured as follows. Section 2 provides an overview of our approach towards computer-aided diagnoses for prostate cancer. Procedure and form of the data are summarized in section 3. NAX is introduced in section 4, where we describe the basic components and design decisions in this approach. In section 5 we present preliminary results indicating that the approach presented in this paper is human-competitive. Finally, section 6 summarizes some conclusions and further research.

## 2. PROBLEM DESCRIPTION

Prostate cancer is the most common non-skin malignancy in the western world. The American Cancer Society estimated 234,460 new cases of prostate cancer in 2006 [31]. Recognizing the public health implications of this disease, men are actively screened through digital rectal examinations and/or serum prostate specific antigen (PSA) level testing. If these screening tests are suspicious, prostate tissue is extracted, or biopsied, from the patient and examined for structural alterations. Due to imperfect screening technologies and repeated examinations, it is estimated that more than 1 million people undergo biopsies in the US alone.

### 2.1 Prostate Cancer Diagnosis

The removal of a small section of prostate is most often accomplished by core biopsy. A needle is inserted into the tissue and several (6-23) samples are obtained from different positions. Biopsy, followed by manual examination under a microscope is the primary means to definitively diagnose prostate cancer as well as most internal cancers in the human body. Pathologists are trained to recognize patterns of disease in the architecture of tissue, local structural morphology and alterations in cell size and shape. Specific patterns of specific cell types distinguish cancerous and non-cancerous tissues. Hence, the primary task of the pathologist examining tissue for cancer is to locate foci of the cell of interest and examine them for alterations indicative of disease.

The specific cells in which cancer arises in the prostate

are epithelial cells. While epithelial-origin cancers account for over 85% of all human cancers, they account for more than 95% of prostate cancers. In prostate tissue, epithelial line secretory ducts within the structural cells (collectively termed ‘stroma’) that allow the tissue to maintain its structure and function. Hence, a pathologist will first locate epithelial cells in a biopsy and, to examine for cancer, will mentally segment them from stroma.

Biopsy samples are prepared in a specific manner to aid in recognition of cells and disease. The sample is sliced thin ( $\sim 5\mu\text{m}$  thickness), placed on a glass slide and stained with a dye to provide contrast. The most common dye is a mixture of hematoxylin and eosin (H&E), which stains protein-rich regions pink and nucleic acid-rich regions blue. Empty space, lipids and carbohydrates are typically not stained and characterized by white color in images. Staining allows the pathologist to identify cells based on their nucleus and extra-nuclear regions. Patterns of the same cell type characterize structures. For example, epithelial cells arranged in a circular manner around empty space are characteristic of a duct and endothelial cells similarly arranged are characteristic of blood vessels. The empty space enclosed within a duct in pathology images is termed a lumen. The distortion of the circular pattern of epithelial cells around a lumen is characteristic of cancer.

In low severity cancers, lumens are only slightly distorted, while higher grades of cancer display a lack of lumen and simply consist of masses of epithelial cells supported by little stroma. The relative distortion and change in lumen shape is organized into a grading scheme to assess the severity of the disease, Gleason Scoring system, which is the primary measure of disease that defines diagnosis, helps direct therapy and helps predict those at danger of dying from the disease. Since prostate cancer is multi-focal and the disease quite variable, two dominant patterns of epithelial distortion are selected and each is independently graded on a scale of 1-5. The grades are then summed to provide a Gleason score ranging from 2 (low grade cancer) to 10 (maximum danger cancer). This scale has been widely used since its creation in the 1960s and currently forms the clinical standard of practice. Manual Gleason scoring, however, has severe limitations.

### 2.2 Limitations of Current Practice

Widespread screening for prostate cancer has resulted in a large workload of biopsied men [16], placing an increasing demand on services. Operator fatigue is well-documented and guidelines limit the workload and rate of examination of samples by a single operator (examination speed and throughput). Importantly, inter- and intra-pathologist variation complicates decision-making. The consistency in determining Gleason scores is rather poor. Intra-observer measurements show that a pathologist confirms their own score less than 50% of the time and are  $\pm 1$  score no more than 80% of cases [2]. Hence, the diagnoses for  $\sim 50\%$  of cases may change and may be significantly altered for  $\sim 20\%$  of cases ultimately leading to changes in therapy for a patient subset [30]. The numbers are decidedly cause for concern. For example, a recent study including 15 pathologists and 537 prostate cancer patients, 70.8% of Gleason scores were shown to be inaccurate when compared with the patient’s final outcome [18]. Second opinions [29] improve assessment and are cost-effective [10], not to mention their utility in mit-

igating the effects of healthcare costs, lost wages, morbidity, or potential litigation. In summary, the manual recognition of spatial patterns leaves much to be desired from a process perspective and has far-reaching social effects from a public health perspective.

For the reasons underlined above, there is an urgent need for high-throughput, automated and objective pathology tools. We believe that this need is best met by employing the power of computer algorithms and advanced processing to address prostate cancer diagnosis and grading.

The information content of conventionally stained images is limited, inherently non-specific and varies greatly within patient populations and processing conditions. Hence, the information derived from visible microscopy images is fundamentally limited and automated methods of analyzing stained images have failed to provide a sufficiently robust algorithm to diagnose disease. An alternative to morphology-based microscopy are molecular microscopy techniques to probe disease. Molecular technologies for disease diagnosis are an exciting venue for investigations as they promise better diagnostic capabilities through objective means and a multitude of chemicals to provide insight into the changes indicative of the disease process. In particular, spectroscopy tools allow for the measurement of many molecular species simultaneously. Spectroscopic techniques in imaging form, notably using optics, further enable the analysis to be conducted without perturbing the tissue [11]. In this manuscript, we present the analysis of prostate tissue with one such technique, Fourier transform infrared (FTIR) spectroscopic imaging.

### 2.3 Molecular Imaging

Infrared spectroscopy is a classical technique for measuring the chemical composition of specimens. At specific frequencies, the vibrational modes of molecules are resonant with the frequency of infrared light. By monitoring all frequencies in the region, a pattern of absorption can be created. This pattern, or spectrum, is characteristic of the chemical composition and is hypothesized to contain information that will help determine the cell type and disease state of the tissue. Recently, FTIR spectroscopy has been developed in an imaging sense. Hence, The data are similar to optical microscopy. The first difference is that no external dyes are needed and the contrast in images can be directly obtained from the chemical composition of the tissue. The second is that each pixel in the visible image contains RGB values but in IR imaging contains several thousand values across a bandwidth ( $2000 - 14000\text{nm}$ ) that is  $\sim 40$  times larger than the visible spectrum ( $400 - 700\text{nm}$ ) [7].

## 3. DATA AND METHODOLOGY

### 3.1 Experimental Details

Prostate tissues were obtained from Cooperative Human Tissue Network for the tissue array research program (TARP) laboratory. Using these tissues, tissue microarrays were prepared using a Beecher automated tissue arrayer containing a video overlap system and  $0.6\text{mm}$  needles. Appropriate institutional review board and National Institutes of Health (USA) guidelines for the protection of human subjects were followed.  $5\mu\text{m}$  sections of tissue were floated on an infrared transmissive optical window for FTIR spectroscopic imaging. Another  $5\mu\text{m}$  section obtained from the same point

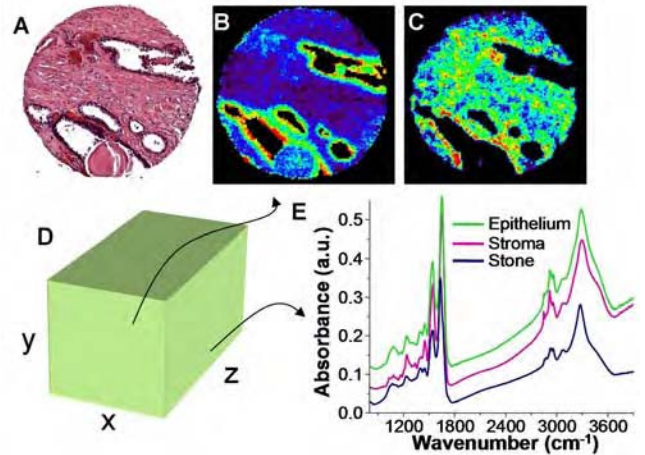


**Figure 1: Conventional Staining and Automated Recognition by Chemical Imaging.** (A) Typical H&E stained sample, in which structures are deduced from experience by a human. Highlights of specific regions in the manner of H&E is possible using FTIR imaging without stains. (B) Absorption at  $1080\text{ cm}^{-1}$  commonly attributed to nucleic acids and (C) to proteins of the stroma. The data obtained is 3 dimensional (D) from which spectra (E) or images at specific spectral features may be plotted.

on the tissue specimen was observed using traditional microscopy for comparison. Expert pathologists determined the tissue classification using these microscopy samples by staining with *H&E*. Pathologists' classification were used as the 'gold standard' for comparison with the results from the methods mentioned in this paper.

Tissues were analyzed using a Michelson interferometer attached to a microscope (Perkin-Elmer Spotlight 300) in transmission mode at a resolution of  $4\text{cm}^{-1}$ . The sample was then raster scanned to obtain images of the entire specimen. Typical specimen size is  $600\mu\text{m} \times 600\mu\text{m}$  with each pixel being  $6.25\mu\text{m} \times 6.25\mu\text{m}$  on the sample plane. Spectra are composed of 1,641 sample points of the spectral range  $4,000 - 720\text{cm}^{-1}$ . Data acquisition using these techniques required 40 minutes per cylindrical core of the tissue microarray to yield a root mean square signal to noise ratio of 500 : 1. A typical array was composed of approximately 2.5 million pixels and required 40 GB of storage space.

The data obtained from FTIR imaging is three-dimensional. The  $x$ - and  $y$ -dimensions locate pixels on the tissue-sample plane. The  $z$ -dimension values compose the IR spectrum for the corresponding pixel. The spectra can be analyzed to determine what type of tissue (epithelium, stroma, or muscle) the specimen is as well as whether the tissue is malignant or benign. We have developed this technology to provide data from tissue in minutes and employ a high-throughput sampling strategy using Tissue Microarrays (TMA) to obtain data.[19] Samples from multiple tissues, from multiple patients and multiple clinical settings are included in the data set to maximize the sampling of natural variability and ensure the development of robust analysis algorithms. These high-throughput imaging and

microarray technologies combine to provide very large data sets—see Figure 1. A typical single core consists of  $300 \times 300$  pixels on the  $x - y$  plane with 1641 bands on the  $z$ -axis. A tissue microarray consists of several hundred such cores and analysis of such large datasets (typically, tens of GB) is computationally expensive.

### 3.2 Data Format

Each pixel's  $z$ -dimension contains a spectrum characteristic of the chemical composition of that region of the specimen. Certain spectral quantities provide measures of chemistry. For example, the height of each feature is proportional to its abundance, the peak position is associated with the vibrational identity and peak shape often reflects the multitude of environments around the molecule. Therefore, differences in spectral characteristics can be used in classification and these exact spectral features are termed ‘metrics’. For example, the ratio of absorbance of the spectral peak at  $1080\text{cm}^{-1}$  to the spectral peak at  $1545\text{cm}^{-1}$  is commonly used to distinguish epithelial from stromal cells. Trained spectroscopists determine these metrics based upon examination of spectral patterns. Hence, the reduction of all spectra to descriptive metrics forms an intelligent dimensionality reduction strategy. Genetic algorithms form decision rules based upon these metrics to classify pixels by tissue type. Furthermore, the transparency of the genetic algorithms allows the scientist to correlate specific rules to biological features (tissue type and cancer classification) via metrics based upon spectral characteristics.

## 4. APPROACH

In this section we review related work on the GBML community, highlighting previous efforts to deal with large data sets. We also present the motivation and techniques that lead to the design of NAX. Special attention is paid to the description of the hardware and software techniques used, as well as to the design of a scalable GBML algorithm.

### 4.1 Related Background

Bernadó, Llorà & Garrell [6] presented a first empirical comparison between genetics-based machine learning techniques (GBML) and traditional machine learning approaches. The authors reported that GBML techniques were able to perform as well as traditional techniques. Later on, Bacardit & Butz [3] repeated the analysis again obtaining similar results. Most of the experiments presented on both papers were conducted using publicly available data sets provided by the *University of California at Irvine* repository [28]. Most of the data sets are defined over tens of features and up to few thousands of records. However, a key property of GBML approaches is its intrinsic massive parallelism and scalability properties. Cantú-Paz [8] presented how efficient and accurate genetics algorithms could be assembled, and Llorà [21] presented how such algorithms can be efficiently used as machine learning and data mining techniques.

GBML techniques require evaluating candidate solutions against the original data set matching the candidate solutions (e.g. rules, decision trees, prototypes) against all the instances in the data set. Regardless of the GBML flavor used, Llorà & Sastry [25] showed that as the problem grows, the matching process governs the execution time. For small data sets (teens of attributes and few thousands of records)

the matching process takes more than 85% of the overall execution time marginalizing the contribution of the other genetic operators. This number easily passes 99% when we move to data sets with few hundreds of attributes and few hundred thousands of records. Such results emphasize one unique facet of GBML approaches: scalability via exploiting massive parallelism. More than 99% of the time required is spent on evaluated candidate solutions. Each solution evaluation is independent of each other and, hence, it can be computed in parallel. Moreover, the evaluation process can also be parallelized further on large data sets by splitting and distributing the data across the computational resources. A detailed description of the parallelization alternatives of GBML techniques can be found elsewhere [21].

Currently available off-the-shelf GBML methods and software distributions [5, 20] do not usually target dealing with very large data sets. Three different works need to be mentioned here. Flockhart [12] proposed and implemented GA-MINER, one of the earliest effort to create data mining systems based on GBML systems that scale across symmetric multi-processors and massively parallel multi-processors. The work review different encoding and parallelization schemes and conducted proper scalability studies. Llorà [21] explored how fine-grained parallel genetic algorithms could become efficient models for data mining. Theoretical analysis of performance and scalability were developed and validated with proper simulations. Recently, Llorà & Sastry [25] explored how current hardware can be efficiently used to speed up the required matching of solutions against the data set. These three approaches are the basis of the incremental rule learning proposed in the next section to approach very large data sets—such as the prostate tissue classification one.

### 4.2 The Road to Tractability

NAX evolves, one at a time, maximally general and maximally accurate rules. Then, the covered instance are removed and another rule is added to the previously stored one, forming a decision list. This process continues until no uncovered instances are left. Llorà, Sastry & Goldberg [26] showed that maximally general and maximally accurate rules [32] could also be evolved using Pittsburgh-style learning classifier systems. Later, Llorà, Sastry & Goldberg [27] showed that competent genetic algorithms [15] evolve such rules quickly, reliably, and accurately. From these early works, it can be inferred that approaching real-world problems, such as the prostate tissue classification and cancer diagnosis, using GBML techniques may produce the desired byproduct: proper scalability. We discuss next efficient implementation techniques to deal with very large data sets using NAX [24].

### 4.3 Exploiting the Hardware

Recently, multimedia and scientific applications have pushed CPU manufacturers to include support for vector instruction sets again in their processors. Both applications areas require heavy calculations based on vector arithmetic. Simple vector operations such as *add* or *product* are repeated over and over. During 80s and 90s supercomputers, such as Cray machines, were able to issue hardware instructions that took care of basic vector operations. A more constrained scheme, however, has made its way into general-purpose processors thanks to the push of multime-

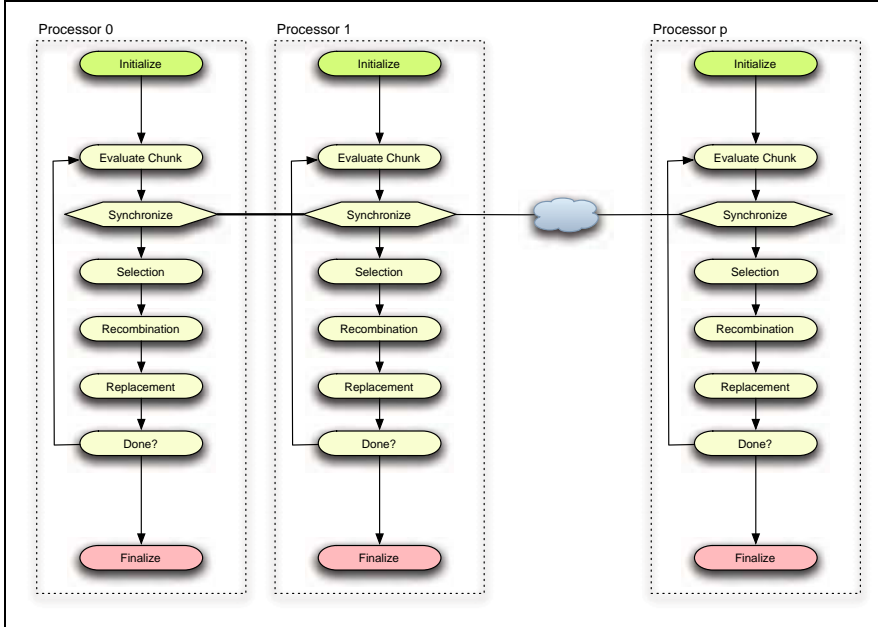


Figure 2: This figure illustrates the parallel model implemented. Each processor is running an identical NAX algorithm. They only differ in the portion of the population being evaluated. The population is treated as collection of chunks where each processor evaluates its own assigned chunk sharing the fitness of these individuals with the rest of processors. This approach minimizes communication cost.

dia and scientific applications. Main chip manufacturers—IBM, Intel, and AMD—have introduced vector instruction sets—AltiVec, SSE3, and 3DNow<sup>+</sup>—that allow performing vector operations over packs of 128 bits by hardware. We will focus on a subset of instructions that are able to deal with floating point vectors. This subset of instructions to implemented by hardware vector operations against groups of four floating-point numbers. These instructions are the basis of the fast rule matching mechanism proposed.

Our set of rules seek both to correctly classify the prostate data set and provide biological insight into the rules. All the attributes of the domain are real-value and the conditions of the rules need to be able to express conditions in a  $\mathbb{R}^n$  spaces. We use a rule encoding similar to the one proposed by Wilson [33] and widely used in the GBML community. Rules express the conjunction of tests across attributes. Each test can be defined in multiple fashions, but without loss of generality, we pick a simple interval based one. A simple example of an *if-then* rule, could be expressed as follows:

$$1.0 \leq a_0 \leq 2.3 \wedge \dots \wedge 10.0 \leq a_n \leq 23 \rightarrow c_1 \quad (1)$$

Where the condition is the conjunction of the different attribute tests, as introduced earlier, and the condition is the predicting class. We also allow a special condition—*don't care*—which always returns `true` to allow generalized to rules evolve. The rule below illustrates an example of a generalized rule.

$$1.0 \leq a_0 \leq 2.3 \wedge -3.0 \leq a_3 \leq 2 \rightarrow c_1 \quad (2)$$

All attributes except  $a_0$  and  $a_3$  were marked as *don't care*.

Matching a rule requires performing the individual tests before the final *and* condition can be computed. Vector instruction sets can help improve the performance of this process by performing four tests at once. Actually, this process can be regarded as four parallel running pipelines. The

process can be improved further by stopping the matching process when any one test fails. The code implemented assumes that the two vectors containing the upper and lower bounds are provided and records are stored in a two dimensional matrix. As also shown elsewhere [25], exploiting the hardware available can speed between 3 and 3.5 times the matching process[24].

#### 4.4 Massive Parallelism

Since most of the time is spent on the evaluation of candidate rules when dealing with large data sets, our next goal was to find a parallelization model that could take advantage of this feature. Due to the embarrassing parallelism model [17] for rule evaluation, we designed a coarse-grain parallel model for distributing the evaluation load. Cantú-Paz [8] proposed several schemes, showing the importance of the trade off between computation time and time spent communicating. When designing the parallel model, we focused on minimizing the communication cost. Usually, a feasible solution could be a master/slave one—the computation time is much larger than the communication one. However, GBML approaches tend to use rather large populations, forcing us to send rules to the evaluation slaves and collect the resulting fitness. This scheme also increments sequential instructions that cannot be parallelized, reducing the overall speedup of the parallel implementation as a result of Ambdhal's law [1].

To minimize communication cost, each processor runs identical NAX algorithms—all seeded in the same manner, and, hence performing the same genetic operations. They only differ in the portion of the population being evaluated. Thus, the population is treated as collection of chunks where each processor evaluates its own assigned chunk, sharing the fitness of the individuals in its chunk with the rest of processors. in this manner fitness can be encapsulated and broadcasted, maximizing the occupation of the underlying pack-

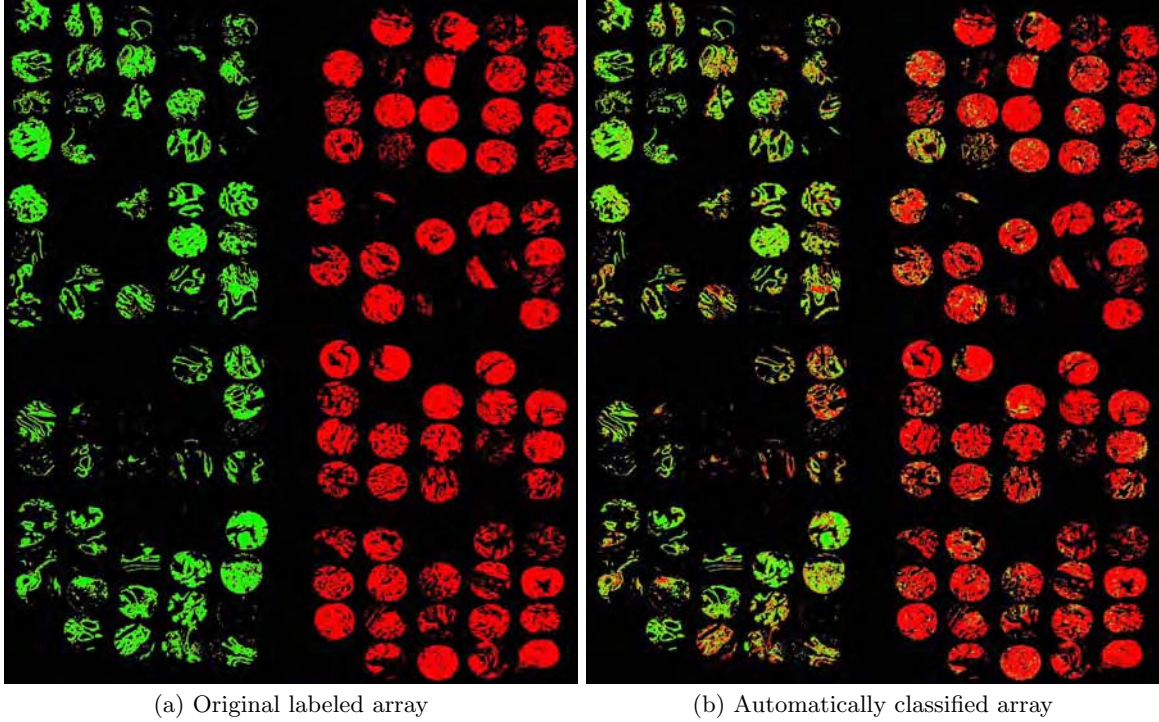


**Figure 3:** This figure on the left-hand side presents the original labeled data contained in the P80 array. The figure on the right-hand side presents the reconstructed image based on the predictions issued by the the rule set evolved by NAX. Green represent non cancerous tissue spots; red represent malignant tissue spots.

ing frames used by the network infrastructure. Moreover, this approach also removes the need for sending the actual rules back and forth between processors—as a master/slave approach would require—thus, maintaining the communication to the bare minimum—namely, the fitness. Figure 2 presents a conceptual scheme of the parallel architecture of NAX.

To implement the model presented in Figure 2, we used C and the *open message passing interface* (openMPI) implementation [13]. Each processor computes which individuals are assigned to it. Then it computes the fitness and, finally, it broadcasts the computed fitness. The rest of the process is unchanged. Except for the cooperative evaluation, all the processors generate the same evolutionary trace.

#### 4.5 Lists of Maximally General and Maximally Accurate Rules

One main characteristic of the so-called Pittsburgh-style learning classifier systems—a particular type of GBML—is that the individuals encode a rule set [14, 22, 15]. Thus evolutionary mechanisms directly recombine one rule set against another one. For classification tasks of moderate complexity, the rule sets are not large. For complex problems, however, the potential number of rules required to ensure accurate classification may use prohibitively large amounts of memory. The requirements increase even further in the presence of noise [23]. Hence, this family of GBML techniques works very well on moderate complexity problems [6, 3], but needs to be modified for complex and large data sets.

A sequential rule learning approach may alleviate the re-

quirements by evolving only one rule at a time, hence, reducing the memory requirements [9, 4]. This allows maintaining relatively small memory footprints that makes feasible processing large data sets. However, an incremental approach to the construction of the rule set requires paying special attention to the way rules are evolved. For each run of the genetic algorithm, we would like to obtain a maximally general and maximally accurate rule, that is, a rule that covers the maximum number of examples without making mistakes [32]. NAX (our proposed incremental rule learner) evolves maximally general and maximally accurate rules by computing the *accuracy* ( $\alpha$ ) and the *error* ( $\varepsilon$ ) of a rule [26]. In a Pittsburgh-style classifier, the *accuracy* may be computed as the proportion of overall examples correctly classified, and the *error* is the proportion of incorrect classifications issued. Once the *accuracy* and *error* of a rule are known, the fitness can be computed as follows.

$$f(r) = \alpha(r) \cdot \varepsilon(r)^{\gamma} \quad (3)$$

where  $\gamma$  is the error penalization coefficient. We have set  $\gamma$  to 18 to guarantee that the evolutionary process will produce maximally general and maximally accurate solutions. Further details may be found elsewhere [24]. The above fitness measure favors rules with a good classification accuracy and a low error, or maximally general and maximally accurate rules. By increasing  $\gamma$ , we can bias the search towards correct rules. This is an important element because assembling a rule set based on accurate rules guarantees the overall performance of the assembled rule set. NAX’s efficient implementation of the evolutionary process is based on the techniques described using hardware acceleration—section

4.3—and coarse-grain parallelism—section 4.4. The genetic algorithm used was a modified version of the *simple genetic algorithm* [14] using tournament selection ( $s = 4$ ), one point crossover, and mutation based on generating new random boundary elements.

## 5. RESULTS

**NAX** has shown competitiveness in evolving rule sets that perform as accurately as the ones evolved by other genetics-based machine learning and non-evolutionary machine learning techniques. However, **NAX**'s key element is the ability to deal with large data sets. In this paper, we present preliminary results towards evolving a model capable of correctly classifying pixels as cancerous or non-cancerous. The original array of spots is presented in figure 3(a). Each spot corresponds to a different biopsy sample from a patient. The pixels present in each spot correspond to the epithelial tissue of the biopsy, we suppress all other tissue types with a prior classification filter based on Bayesian Likelihood.[7] Each pixel of a spot is defined by 93 different metrics extracted from the processed infrared spectra—as described in section 3. Finally, each pixel in the array was labeled with the diagnostic class provided by a human pathologist. Figure 3(a) presents in green all the non-cancerous pixels while red identifies cancerous ones.

Our goal with the initial experiments here was to demonstrate the usefulness of the proposed approach to computer-aided diagnosis. Our current experimental efforts are planning mass experimentation on several tissue arrays using the Tungsten cluster at the National Center for Supercomputing Applications. These initial experiments were conducted on a dual core Intel Xeon 2.8GHz Linux computer with 1Gb of RAM. **NAX** was run using both processors. The training time to obtain a model describing all the data took less than ten hours—indicating that very competitive training times can be achieved by just using more processors. The obtained model was able to correctly classify  $> 99.99\%$  of the training pixels correctly. However, these results do not illustrate the generalization capabilities of the models evolved by **NAX**. Hence, we ran a series of ten-fold stratified cross-validation runs [34] to measure generalization and test performance of the evolved models. It is important to mention that tools such as WEKA [34] and other off-the-shelf data miners were not able to handle the volume of data required to evolve a model—either due to the large memory footprint required or by not being able to provide an accurate model in a feasible time period. The results of the cross-validation experiments using **NAX** correctly classified 87.34% of validation pixels. Such results are more than encouraging, because they show a human-competitive computer-aided diagnosis system is possible. Another interesting property is that a few rules classify a large number of pixels—see Figure 4. Such a result is interesting for the interpretability of the model, since a small number of rules have a great expressiveness, and hence may provide valuable biological insight. Most importantly, they allow us to classify tissue accurately. Subsequent to this pixel level classification, each circular spot in figure 3 was assigned as malignant or benign based on the majority of pixels of he class in the sample. We were able to accurately classify 68 of 69 malignant spots and 70 of 71 benign spots in this manner. While human accuracy is difficult to quantify due to the variation between persons, a generally accepted anecdotal figure is about 5%

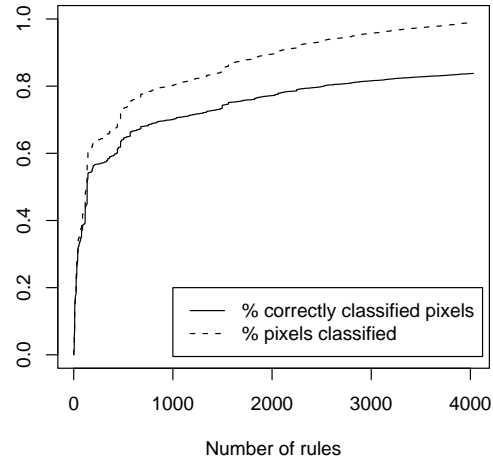


**Figure 4: Performance of the evolved model as a function of the number of rules used.**

error rates. The preliminary results we demonstrate here could potentially reduce that five-fold to about 1%, providing a solution to this real-world problem by a combination of novel spectroscopy and advanced machine learning.

## 6. CONCLUSION

In this manuscript, we present the application of advanced genetics-based machine learning algorithms to a real-world problem of large scope, namely, the diagnosis of prostate cancer. As opposed to subjective human recognition of disease in tissue using light microscopy, we employed a chemical microscopy approach that required extensive computation but provided a decision without human input. Our development of a learning algorithm based on maximally general and maximally accurate rules was scalable to very large data sets and parallelized to provide learning and classification speed advantages. The algorithm was able to classify a majority of pixels correctly, resulting in overall error rates that were comparable to human examination, the current gold standard of care.

## 7. ACKNOWLEDGMENTS

This work was sponsored by the Air Force Office of Scientific Research, Air Force Materiel Command, USAF, under grant FA9550-06-1-0370, the National Science Foundation under grant ISS-02-09199 at the National Center for Supercomputing Applications, UIUC. The U.S. Government is authorized to reproduce and distribute reprints for government purposes notwithstanding any copyright notation thereon.

The views and conclusions contained herein are those of the authors and should not be interpreted as necessarily representing the official policies or endorsements, either expressed or implied, of the Air Force Office of Scientific Research, the National Science Foundation, or the U.S. Government. We would like to thank Dr. Stephen M. Hewitt, MD PhD, who provided us the samples and expert pathol-

ogy consultation. The research is also supported by grants to RB from the Research Board, UIUC; the Department of Defense through the Prostate Cancer Research Program and by the National Center for Supercomputing Applications, under the auspices of the NCSA/UIUC faculty fellows program.

## 8. REFERENCES

- [1] G. Amdahl. Validity of the single processor approach to achieving large-scale computing capabilities. In *Proceedings of the American Federation of Information Processing Societies Conference (AFIPS)*, volume 30, pages 483–485. AFIPS, 1967.
- [2] M. Amin, D. Grignon, P. Humphrey, and J. Srigley. *Gleason Grading of Prostate Cancer: A Contemporary Approach*. Lippincott Williams & Wilkins: Philadelphia, 2004.
- [3] J. Bacardit and M. Butz. *Advances at the frontier of Learning Classifier Systems (Volume I)*, chapter Data Mining in Learning Classifier Systems: Comparing XCS with GAssist, page in press. Springer-Verlag, 2006.
- [4] J. Bacardit and N. Krasnogor. Biohel: Bioinformatics-oriented hierarchical evolutionary learning. Nottingham eprints, University of Nottingham, 2006.
- [5] A. Barry and J. Drugowitsch. LCSWeb: the LCS wiki, 1997. <http://lcsweb.cs.bath.ac.uk/>.
- [6] E. Bernadó, X. Llorà, and J. Garrell. *Advances in Learning Classifier Systems: 4th International Workshop (IWLCS 2001)*, chapter XCS and GALE: a Comparative Study of Two Learning Classifier Systems with Six Other Learning Algorithms on Classification Tasks, pages 115–132. Springer Berlin / Heidelberg, July 2001.
- [7] R. Bhargava, D. Fernandez, S. Hewitt, and I. Levin. High throughput assessment of cells and tissues: Bayesian classification of spectral metrics from infrared vibrational spectroscopic imaging data. *Biochimica et Biophysica Acta*, pages 830–845, 2006.
- [8] E. Cantú-Paz. *Efficient and Accurate Parallel Genetic Algorithms*. Kluwer Academic Publishers, 2000.
- [9] O. Cordón, F. Herrera, F. Hoffmann, and L. Magdalena. *Genetic Fuzzy Systems. Evolutionary tuning and learning of fuzzy knowledge bases*. World Scientific, 2001.
- [10] J. Epstein, P. Walsh, and F. Sanfilippo. Clinical and Cost Impact of Second-opinion Pathology: Review of Prostate Biopsies Prior to Radical Prostatectomy. *American Journal of Surgical Pathology*, 20:851–857, 1996.
- [11] D. Fernandez, R. Bhargava, S. Hewitt, and I. Levin. Infrared spectroscopic imaging for histopathologic recognition. *Nature Biotechnology*, 23(4):469–474, 2005.
- [12] I. Flockhart. GA-MINER: parallel data mining with hierarchical genetic algorithms (final report). Technical Report Technical Report EPCCAIKMS-GA-MINER-REPORT 1.0, University of Edinburgh, 1995.
- [13] E. Gabriel, G. Fagg, G. Bosilca, T. Angskun, J. Dongarra, J. Squyres, V. Sahay, P. Kambadur, B. Barrett, A. Lumsdaine, R. Castain, D. Daniel, R. Graham, and T. Woodall. Open MPI: Goals, concept, and design of a next generation MPI implementation. In *Proceedings of the 11th European PVM/MPI Users' Group Meeting*. Springer, 2004.
- [14] D. Goldberg. *Genetic Algorithms in Search, Optimization, and Machine Learning*. Addison-Wesley Professional., 1989.
- [15] D. Goldberg. *The Design of Innovation: Lessons from and for Competent Genetic Algorithms*. Springer, 2002.
- [16] S. J. Jacobsen, S. K. Katusic, E. J. Bergstrahl, J. E. Oesterling, O. Del, G. G. Klee, C. G. Chute, and M. M. Lieber. Incidence of prostate cancer diagnosis in the eras before and after serum prostate-specific antigen testing. *JAMA*, 274:1445–1449, 1995.
- [17] V. Kumar, A. Grama, A. Gupta, and G. Karpis. *Introduction to Parallel Computing: Design and Analysis of Parallel Algorithms*. Benjamin-Cummings Publishing Company, 1994.
- [18] J.-B. Lattouf and F. Saad. Gleason score on biopsy: is it reliable for predicting the final grade on pathology? *BJU International*, 90:694–699, 2002.
- [19] I. Levin and R. Bhargava. Fourier transform infrared vibrational spectroscopic imaging: integrating microscopy and molecular recognition. *Annual Review of Physical Chemistry*, 56:429–474, 2005.
- [20] X. Llorà. Learning Classifier Systems and other Genetics-Based Machine Learning Blog, 2006. <http://www.illigal.ge.uiuc.edu/lcs-n-gbml/>.
- [21] X. Llorà. *Genetics-Based Machine Learning using Fine-grained Parallelism for Data Mining*. PhD thesis, Enginyeria i Arquitectura La Salle. Ramon Llull University, Barcelona, Catalonia, European Union, February, 2002.
- [22] X. Llorà and J. Garrell. Knowledge-independent data mining with fine-grained parallel evolutionary algorithms. In *Proceedings of the Genetic and Evolutionary Computation Conference (GECCO'2001)*, pages 461–468. Morgan Kaufmann Publishers, 2001.
- [23] X. Llorà and D. Goldberg. Bounding the effect of noise in multiobjective learning classifier systems. *Evolutionary Computation Journal*, 11(3):279–298, 2003.
- [24] X. Llorà, A. Priya, and R. Bhargava. Observer-invariant histopathology using genetics-based machine learning. Technical report, Illinois Genetic Algorithms Laboratory, University of Illinois at Urbana-Champaign (IlliGAL TR No 200627), 2006.
- [25] X. Llorà and K. Sastry. Fast rule matching for learning classifier systems via vector instructions. In *Proceedings of the 2006 Genetic and Evolutionary Computation Conference*, pages 1513–1520. ACM Press, 2006.
- [26] X. Llorà, K. Sastry, and D. Goldberg. The compact classifier system: Motivation, analysis and first results. In *Proceedings of the Congress on Evolutionary Computation*, volume 1, pages 596–603. IEEE press, 2005. (Also as IlliGAL TR No. 2005019 ).
- [27] X. Llorà, K. Sastry, D. Goldberg, and L. de la Ossa. The  $\chi$ -ary extended compact classifier system: Linkage learning in Pittsburgh LCS. In *Advances at the frontier of Learning Classifier Systems (Volume II)*, page in preparation. Springer, 2007. IlliGAL report no. 2006015.
- [28] C. J. Merz and P. M. Murphy. UCI repository for machine learning data-bases, 1998. <http://www.ics.uci.edu/~mlearn/MLRepository.html>.
- [29] W. Murphy, I. Rivera-Ramirez, L. Luciani, and Z. Wajsman. Second opinion of anatomical pathology: A complex issue not easily reduced to matters of right and wrong. *J. Urol.*, 165:1957–1959, 2001.
- [30] J. Nguyen, D. Schultz, A. Renshaw, R. Vollmer, W. Welch, K. Cote, and A. D'Amico. The impact of pathology review on treatment recommendations for patients with adenocarcinoma of the prostate. *Urologic Oncology: Seminars and Original Investigations*, 22:295–299, 2004.
- [31] A. C. Society. How Many Men Get Prostate Cancer?, 2006. [http://www.cancer.org/docroot/CRI/content/CRI\\_2\\_2\\_1X\\_How\\_many\\_men\\_get\\_prostate\\_cancer\\_36.asp?rnav=cri](http://www.cancer.org/docroot/CRI/content/CRI_2_2_1X_How_many_men_get_prostate_cancer_36.asp?rnav=cri).
- [32] S. Wilson. Classifier fitness based on accuracy. *Evolutionary Computation*, 3(2):149–175, 1995.
- [33] S. Wilson. Get real! XCS with continuous-valued inputs. *Lecture Notes in Computer Science*, 1813:209–219, 2000.
- [34] I. H. Witten and E. Frank. *Data Mining. Practical Machine Learning Tools and Techniques with Java Implementations*. Morgan Kaufmann, San Francisco, CA., 2000.

# **Fourier transform infrared spectroscopic imaging: the emerging evolution from a microscopy tool to a cancer imaging modality**

Gokulakrishnan Srinivasan and Rohit Bhargava

*Department of Bioengineering and Beckman Institute for Advanced Science and Technology,  
University of Illinois at Urbana-Champaign, Urbana, IL 61801*

## **INTRODUCTION**

The integration of FTIR spectroscopy with microscopy facilitates recording of spatially resolved spectral information, allowing the examination of both the structure and chemical composition of a heterogeneous material. While the first such attempt was over 50 years ago,<sup>1</sup> present day instrumentation largely evolved from the point microscopy detection of interferometric signals that developed in the mid-80s.<sup>2</sup> The successful coupling of interferometry for spectral recording and microscopy for spatial specificity in these systems spurred interest in a variety of fields, including the materials,<sup>3</sup> forensic<sup>4</sup> and biomedical arenas.<sup>5, 6</sup> Point microscopy utilizes an aperture to restrict radiation incident on a sample and permits the recording of spatially localized data. The primary utilities of this form of microscopy lay in acquiring accurate spectra from small-size samples, in determining the chemical structure and composition of heterogeneous phases at specified points and in building a two-dimensional map of the chemical composition of samples. Since the data were acquired at a single point, composition maps could only be acquired by rastering the sample. Hence, the approach was termed mapping or point mapping and involved as many spectral scans as the number of pixels in the map.

The use of focal plane array (FPA) detectors for microscopy<sup>7, 8</sup> allowed for the acquisition of large fields of view in a single interferogram acquisition sweep. The multichannel detection enabled by array detectors was similar to the concept of recording images with charge coupled devices in optical microscopy; hence, the approach was termed imaging. The unique advantages of observing an entire field of view rapidly permitted applications that allowed monitoring of dynamic processes, spatially resolved spectroscopy of large samples or many samples and enhancement of spatial resolution due to retention of radiation throughput that was lost in point microscopy systems due to diffraction at the aperture. Just as for the previous generation of microspectroscopy instruments, applications rapidly followed in the materials<sup>9</sup> and biomedical fields.<sup>10-14</sup> Research activity in this area can be divided into three major categories: instrumentation and sampling methodologies, applications and data extraction algorithms. In this manuscript, we review key advances and recent developments in the context of biomedical imaging. We do not provide comprehensive overview but selectively highlight certain features of importance for cancer-related imaging. Last, we focus on one emerging application area, namely tissue histopathology, and provide illustrative examples from our laboratory indicating the integrative nature of the three in developing protocols.

## **INSTRUMENTATION, SAMPLING AND DATA HANDLING TECHNIQUES**

### **Instrumentation**

Since imaging is largely based on new detectors with unique performance characteristics for spectroscopy, efforts in instrumentation have largely focused on the efficient integration of FPA detectors with interferometers. Due to the size, different electronics and unique noise characteristics of FPAs, an optimization of data acquisition methodology was a primary activity in the initial time period of availability of instrumentation. The first rational attempt at understanding performance and optimizing the data acquisition process revealed the unique noise characteristics that limited the first generation of array detectors.<sup>15</sup> Briefly, this paper established that the general behavior of FTIR spectrometers is generally held for imaging spectrometers but the detector may serve to limit the applicability of established practices in IR spectrometry. An explicit optimization of the data acquisition time revealed several strategies for speeding data collection for both the step scan and rapid scan mode.<sup>16</sup> The first example of rapid-scan FTIR imaging<sup>17</sup> was conducted using asynchronous sampling, followed by descriptions of synchronously triggered sampling and generalized methodologies<sup>18</sup> that could use any detector at any modulation frequency using post-acquisition techniques. Advances in detector technology have now allowed for rapid scan imaging to become routine for large FPA detectors, while innovative new detectors have been developed (first by PerkinElmer) that trade off a large multichannel detection advantage of arrays against the speed of smaller detector arrays to provide a very high performance instrument.<sup>19</sup>

At present, rapid scan imaging has become the mode of choice for most manufacturers and detector sizes have proliferated from the classic 64 x 64 format to range from 16 x 1 to 256 x 256 formats (see figure 1). While the smaller detectors require rastering to image most samples and can provide data of higher quality more efficiently, larger detectors are generally employed for their large field of view and are useful for studying dynamics. It is interesting to note that the linear array approach has an entirely different detector technology and considerations for electronics compared to the two-dimensional FPAs. While it is beyond the scope of this article to discuss the differences, the use of “macro” electronics that are offset from the actual detector and AC mode of operation are the two major differences that affect data. Consequently, comparisons in performance are slightly more complicated. On the large format FPA front, the latest advance seems to be a detector developed jointly by NIH and FBI personnel in 2005. The detector can operate at 16 KHz for 128 x 128 pixel snaps (*Bhargava, Levin, Perlman and Bartick, Unpublished*). This is in the speed regime of single element detectors. Hence, the development can truly lead to the acquisition of an entire image in a single interferometer mirror sweep in the same time that it takes to acquire 1 spectrum with a benchtop IR spectrometer. To handle the large data output, we designed on-chip co-addition and various corrections. We believe that similar detector systems, operating in a fast regime and integrating processing with electronics, are likely to be the technology of tomorrow for FTIR imaging.

The wide variety of instrumentation makes comparisons difficult, especially when manufacturers provide different specifications for instruments. We have proposed a comparison index for these systems based on performance per unit time. Recognizing that spectral resolution, time for scanning, data processing (e.g. apodization) and resultant image size are the primary determinants of performance, a measure can be formulated to describe performance. For a fixed

data processing scheme (filtering, apodization etc.), the time taken to acquire 1 megapixels of data for  $8\text{ cm}^{-1}$  resolution at a signal to noise ratio (SNR) of 1000:1 is found to be a good measure. We would like to emphasize that the performance is the performance of the entire imaging spectrometer and not due to the detector alone. Efficient coupling of the interferometer and optimization of the optical train will both affect performance as will the correct setup of the experiment. This index also does not consider the ease of use or “user-friendliness” of systems. These are other important considerations and must also be considered by organizations interested in FTIR imaging technology. The issue of time resolution for acquiring data is one such concern. The first approach is the kinetics approach in which the interferometer is repeatedly scanned and imaging data sets are sequentially acquired as quickly as possible. Clearly, rapid scan is favored and the availability of fast readout detectors is mandatory for fast events. The limit to this method is the readout speed of the array (frames in ms) as interferometers can generally be scanned fast enough and the integration time required is typically in the tens of microseconds regime. An example is shown in figure 2 to demonstrate applicability in monitoring polymerization kinetics.

Though rapid scan imaging has displaced the step-scan mode in most new instrumentation, a very important application of the step-scan approach remains in time-resolved imaging.<sup>20-22</sup> Briefly, the method is applicable to systems that can be repeatedly and reproducibly excited and relax back to their ground state. At each mirror retardation, the FPA is repeatedly triggered to acquire data. At the same time, the sample is excited once and the dynamics of excitation and decay of the excited state are monitored. Mirror stepping, data acquisition and sample excitation are all precisely synchronized. Figure 3 demonstrates the synchronization. Time resolved FTIR imaging was first demonstrated using polymer-liquid crystal composites. Examples of the types of data that may be obtained are also shown in figure 3. Last, the technology was extended to provide significantly higher time resolution than could be obtained by the electronics of the detector alone.<sup>23</sup> While FPA detectors are slow compared to single point detectors used in conventional FTIR spectroscopy, the cause is the need to read out data from several thousand pixels and not from the need to record data from all pixels. Hence, by staggering the data recording time over multiple sample excitations, higher temporal resolution may be obtained. With current detectors, a time resolution of  $\sim 30\text{ }\mu\text{s}$  should be possible.

## Sampling

### *Interferometer Issues*

Among the sampling configurations, the first clearly was the optimization of the microscope for transmission and sampling. Unexpected issues were encountered in initial devices. For example, the detector for the mono-wavelength laser provides a fringe pattern to allow for tracking mirror retardation. The signal from this laser is measured by a small detector located at the center of the beamsplitter (to minimize errors) with an arm that extends out to the edge. When imaged onto the FPA, this laser detector leads to a pattern with low signal levels. Hence, the field of view is not uniform, leading in turn, to lower signal to noise ratios (SNR) for the affected region. Many manufacturers, hence, have re-designed their spectrometers for imaging use. Another manufacturer has avoided this issue by aligning their microscope to sample only the unaffected part of the beam. Since the non-imaging spectrometer did not require imaging and the interferometer was simply coupled to a microscope, these issues were slowly addressed.

## ***Sampling Modes: Transmission, Transmission-reflection, Reflection and Attenuated Total Reflection***

A vast majority of studies report the use of transmission sampling. Other major developments have been the incorporation of reflective slides,<sup>24, 25, 26</sup> the integration of ATR elements for both microscopy and large sample imaging, integration of ATR technology with various sample forming accessories, grazing angle accessories and multi-sample accessories. Reflective slides actually result in reflection-absorption that allows the beam to sample the signal twice, though with a different phase and lower signal due to half the objective being used for transmitting light to the sample and the other half being used to acquire light from it. A detailed theoretical understanding of the confounding effects has not been published, though an example of the possible data correction algorithm has been reported. ATR imaging is also highly prevalent and available as attachments to conventional imaging microscopes, using the sample chamber of the spectrometer and using it as a solid immersion lens.<sup>27</sup> We discuss examples of ATR imaging next.

### **ATR**

In the Attenuated Total Reflection (ATR) mode, an IR transmitting crystal of precise geometry of high refractive index is employed as a solid immersion lens. Light is totally reflected at the sample-crystal interface and an evanescent field penetrates into the sample to provide the interaction to be observed using the traveling wave. Since the sample interaction is largely determined by the lens and not by the sample, precise and controlled depth of interaction is available. The sample, however, needs to be in good contact to allow efficient coupling with the evanescent wave. ATR imaging allows users to work with relatively thick sample sections that do not require much sample preparation expertise or time. The first use of ATR imaging was reported by Digilab in analyzing large samples that were not sectioned, as for transmission. ATR imaging microscopy was demonstrated soon after,<sup>28</sup> followed by other novel accessories. There were other unpublished attempts that one of the authors is aware of: In 1999, for example, Snively *et al.* (personal communication, unpublished) demonstrated imaging data from an inverted ZnSe prism acting as a single bounce ATR. Soon after, we employed a Ge crystal but found the signal to noise ratio of the imaging system of that time to be very poor. In addition to the ease of sample preparation, another major advantage of ATR imaging lies in improving the limited spatial resolution of transmission microscopy.<sup>29</sup> The authors assessed that they were able to achieve a spatial resolution of 1 $\mu\text{m}$  with a Ge internal reflection element

Both micro and macro sampling has been extensively utilized.<sup>30</sup> A spatial resolution of 3-4  $\mu\text{m}$  using a Ge ATR element was claimed based on more stringent criteria than used previously.<sup>29</sup> Ge, ZnSe and diamond<sup>30</sup> crystals have been the materials of choice for most applications. In particular, Kazarian and co-workers have extensively employed ATR-FTIR imaging for various applications including drug release; polymer/drug formulations and biological systems.<sup>30-33</sup> The same group has provided other innovative sampling configurations for specific experiments, including a compaction cell that allows compaction of a tablet directly on a diamond crystal with a subsequent imaging.<sup>34</sup> The changes in the distribution of a tablet consisting of hydroxypropyl methylcellulose (HPMC) and caffeine upon contact with water were studied. In this manner, conventional dissolution measurements were combined with a concurrent assessment of the compacted tablet structure.<sup>35</sup> As opposed to the organic solvent-polymer dissolution experiments reported earlier, this configuration allows for easy handling and imaging of water-induced dissolution. The setup can also provide high throughput analysis of materials under controlled

environments.<sup>36</sup> Microdroplet sample deposition system was combined with a humidity control device to image about 100 samples deposited on the surface of an ATR crystal simultaneously. The approach was extended to 165 samples and were reported to study parallel dissolution of formulations.<sup>37</sup>

### **Multi-sample Accessories and Sampling**

While imaging the structure of materials has been the primary focus of FTIR imaging, a number of applications utilize the imaging of multiple samples. The first examples were from the field of catalyst research.<sup>38</sup> Typically 2-12 samples could be imaged and analyzed under the same conditions. High throughput validation or method development was the primary goal in these studies. Tissue microarrays (TMAs) provide the same function in biomedical imaging. TMAs consist of tens to hundreds of samples arranged on a grid format. This allows for easy visualization of the structure and classification accuracy across many patients and the statistical measures needed for rigorous validation. The primary utility of the multisample image in this case is to provide wide-ranging sampling and convenient archiving or data storage, not necessarily to provide a higher throughput.<sup>14, 39</sup> With the appropriate geometry, many samples can be imaged to understand their dynamics in a concerted fashion. To accommodate the samples, the field of view is often expanded. This results in a lower spatial resolution. For imaging multiple samples, though, the spatial resolution can be conserved but temporal resolution is restricted.

## **BIOMEDICAL APPLICATIONS**

### **Bone**

Bone has been the tissue studied most by FTIR imaging. Bone composition changes with development, environment, genetics, health and disease, is amenable to imaging at the resolution length scale of imaging and has a limited chemical composition that is characterized using IR spectroscopy.<sup>40</sup> For almost 30 years until the late 1980s,<sup>41</sup> bone structure was studied using single element detectors in FTIR spectrometers. Typically, ground bone was analyzed using the conventional KBr pellet method. This pellet method obviously destroyed local structures, precluding an understanding of molecular variations due to disease. Nevertheless, it was sensitive to chemical composition and did provide useful information. With microscopy and now with FTIR imaging, sample integrity is maintained and ability to acquire spectral information at anatomically discrete sites is possible. From the resulting spectra, several important pieces of information can be obtained. For example, a) relative mixture composition of hydroxyapatite and collagen by calculating the ratio of the integrated  $\nu_1$ ,  $\nu_3$  phosphate and amide 1 (mineral: matrix ratio), b) carbonate substitution by calculating the ratio of carbonate/phosphate ratio from the ratio of integrated  $\nu_2$  carbonate peak ( $850\text{-}900\text{ cm}^{-1}$ ) and  $\nu_1$ ,  $\nu_3$  phosphate contour ( $900\text{-}1200\text{ cm}^{-1}$ ), c) crystallinity of the mineral phase from the ratio of 1030/1020 peak intensity.<sup>42</sup> These assays illustrate several quantities important to bone research and disease diagnoses that can be readily performed. Though a complete discussion is available in the reference<sup>40, 42-44</sup>, we pick three illustrative examples demonstrating the applicability in disease and in research.

IR spectral analysis of healthy and disease bone has been reviewed by Boskey *et al.*<sup>42</sup> with particular emphasis on changes in bones composition, physiochemical status of mineral and matrix of bones during osteoporosis and the effect of therapeutics on these parameters. Osteoporosis or porous bone is a bone disease characterized by low bone mass and structural

deterioration of bone tissue. This leads to bone fragility and an increased susceptibility to fractures, especially at the hip, spine and wrist. FTIR images of the mineral content and crystallinity in trabecular bone of normal and osteoporotic samples clearly depicts that the trabeculae in diseased tissue are thinner. Moreover, the mineral/matrix ratio in osteoporotic bone is significantly reduced, whereas crystallinity is increased. These advances demonstrate the potential and applicability of the technique to characterize diseased tissue. Bone mineral changes between a healthy mouse model and Fabry diseased (lipid storage disease) mouse model were also analyzed in which globotriaosylceramide (Gb3) accumulates in tissues.<sup>43</sup> No significant differences in the bone mineral properties were observed between Fabry and healthy mice, which might reflect the similar lack of major bone phenotype in human patients with Fabry's disease and may also be related to the developmental age of these animals. The study provides an example of the applicability to laboratory research.

Calcified tissue in biopsies from adults with osteomalacia has been studied.<sup>44</sup> Osteomalacia results in a deficiency of the primary mineralization of the matrix, leading to an accumulation of osteoid tissue and reduction in bone's mechanical strength. A decrease in trabecular bone content with absence of changes in matrix or mineral is noticed when iliac crest biopsies of individuals with vitamin D deficient osteomalacia are compared to normal controls. These findings support the assumption that, in osteomalacia, the quality of the organic matrix and of mineral in the centre of the bone does not vary, where as less-than optimal mineralization occurs at the bone surface.

### **Brain**

Monkey brain tissues were one among the first tissues examined by using FTIR imaging.<sup>12</sup> Lately, the applications have experienced a renaissance with applications to the human brain. Grossly, brain can be divided into two types of matter, namely gray matter and white matter. These names derive simply from their appearance to the naked eye. Gray matter consists of cell bodies of nerve cells while white matter consists of the long filaments that extend from the cell bodies - the "telephone wires" of the neuronal network, transmitting the electrical signals that carry the messages between neurons. A visualization of the two compartments formed the first demonstrative application of FTIR microspectroscopic imaging.

FTIR imaging and multivariate statistical analyses (unsupervised hierarchical cluster analysis) were applied alongwith histology and immunohistochemistry in an animal model having Glioblastoma multiform (GBM).<sup>45</sup> GBM is a highly malignant human brain tumor that is considered to be the one of the most difficult to treat effectively.<sup>46</sup> Authors were able to identify the tumor growth as chemically distinct from the surrounding brain tissue. The distribution of the absorbance of amide I in images highlighted high concentrations of proteins in the corpus callosum and regions of basal ganglia for healthy brain. Low absorbance was generally observed in the cortex, whilst a higher absorbance was observed at outer layer of the cortex. For a GBM bearing animal, the highest absorbance was found at the tumor site. In contrast to healthy brain, a lower absorbance of the amide I band was observed at the corpus callosum when compared to that in the cortex and the caudoputamen. The study demonstrates a powerful application of simple analyses that can indicate disease. It also highlights the multitude of spatial and spectral clues that can be used to diagnose or understand the disease.

In addition to primary disease sites, diagnoses metastatic spread from various cancers was also reported.<sup>47</sup> A multivariate classification algorithm was used to distinguish normal tissue from brain metastases successfully and to classify the primary tumor of brain metastases from renal cell carcinoma, lung cancer, colorectal cancer, and breast cancer. In the cluster averaged IR spectra from a brain metastasis of renal cell carcinoma, the main spectral differences were observed for the three tissue regions in the region from 950 to 1200 cm<sup>-1</sup> and from 1500 to 1700 cm<sup>-1</sup>. Band intensities of 1026, 1080 and 1153 cm<sup>-1</sup> are at maximum in the spectrum of black cluster and minimum in the spectrum of light gray cluster. The comparisons of the IR spectra of normal brain tissue and brain metastases of lung, breast cancer and colorectal cancer were made and found that these spectra do not contain spectral features at 1026, 1080 and 1153 cm<sup>-1</sup> that are indicative of the presence of glycogen. It was concluded that these aforementioned spectral features would be considered as a biomarkers for brain metastases of the primary tumor renal cell carcinoma. In addition to these three bands, the spectral differences were observed for the bands at 1542 and 1655 cm<sup>-1</sup>, owing to the presence of amide I and amide II vibrations. It is clear from the results that the maximum protein concentrations correlate with minimum glycogen concentrations in the IR image. However, the protein and glycogen properties evident in the IR image are not visible in the unstained cryosection. It is noteworthy that simple univariate analyses provide the end clues to the disease. Even on application of multivariate techniques, the most prominent and easy to understand biomarkers of disease are those defined by conventional spectroscopic knowledge as being important for identification, namely, features and their absorption.

In the cluster-averaged IR spectra of white matter from the three normal brain tissue samples, intense bands at 1060, 1233, 1466, 1735, 2850 and 2920 cm<sup>-1</sup> due to the high lipid concentration in white matter were noticed. Intensity changes were due to inter-sample and patient to patient variances of the same tissue type. In addition, cluster-averaged IR spectra of a brain metastasis of (renal cell carcinoma, breast cancer, lung cancer, and colorectal cancer) and gray matter of normal brain tissue were compared after baseline subtraction and then normalization with respect to the amide I band. Significant differences in the band positions, intensities and area were observed between these samples which were then used as potential candidates to differentiate normal and tumor tissue and for the identification of the primary tumor. Here, authors used only eight spectroscopic features for LDA model. They were able to classify correctly for three out of three normal brain tissue and 16 out of 17 brain metastases samples. Hence, though univariate analyses and features provide useful recognition, their integration into a multivariate algorithm provides for automated recognition of clinical importance. It may also be argued, however, that it is questionable whether the small numbers of samples employed represent a true performance condition for the algorithm or are simply reflective of bias arising from the clinical setting or sample sources. The advent of faster imaging approaches and advanced sampling techniques like TMAs can allow for larger numbers of samples to be analyzed and such doubts about the validity of studies be put to rest.

Similarly, tissues from rat Glioma models have been characterized and used to discriminate healthy from tumor sections using principal component analysis and K-means.<sup>48</sup> Pseudo color maps reported were constructed on 8-means clusters, where each cluster is consisting of similar spectra. The lipids/protein ratio (1466/1452 cm<sup>-1</sup>) was found to be decreased and the band at 1740 cm<sup>-1</sup> became weak and almost vanished as compared to the corresponding bands in the

healthy tissue. In addition to the above mentioned differences, significant differences between healthy and tumor affected tissue were observed in the finger print region. In the healthy tissue, a weak band at  $1172\text{ cm}^{-1}$ , representing the stretching mode of C-O groups were observed. Reduced intensity as well as shifting of peak to  $1190\text{ cm}^{-1}$  was noted for tumor and surrounding tumor spectra. Tumor tissue was observed to contain a decreased intensity of the asymmetric phosphate stretching and C-C stretching and an increased intensity of the symmetric phosphate stretching when compared to the healthy tissue. Variations in lipid features (methylene and methyl stretching) were also observed. The major point here is that the entire spectrum contains numerous points of difference between healthy and diseased tissue. Results were found to be in agreement with those obtained from pathology.<sup>49</sup> The structural difference around the tumor was noted, which could be ascribed to the peritumoral edema observed during glioma development. An increase in the permeability of the blood-brain barrier and aggravation in the mass effect of tumors are the rationale for edema, which is associated with brain tumor. Fundamental understanding can be enhanced by a complete understanding of the spectral differences but prediction algorithms need only a few measures of the spectral data to be effective.

## Breast

Two major applications in breast tissue deal with complications arising from artificial alterations of the tissue and the evolution of cancer. While breast augmentation by implants is highly prevalent, its complications have been discussed more recently. On the other hand, the conventional method for diagnosing and evaluating the prediction of breast disease is a histopathological examination of biopsy samples, a practice that has some shortcomings. For breast implants, a major question is the containment of filling material as its leakage can lead to potential diseases. The silicone gel in implants is very different chemically from surrounding tissue and its presence in tissue sections indicates a definite leak from the implant either due to material failure as a consequence of aging. A spectroscopic image<sup>50</sup> generated from the asymmetric stretching modes of the methyl groups attached to silicon in the gel allowed for the examination of silicone in the tissue. Due to the unique chemical contrast employed in FTIR imaging, such presence can be discerned within the tissue, even when optical microscopy contrast was poor. An example of presence of Dacron (a commercial name for poly(ethylene terephthalate)) fixative patch threads in the breast tissues was shown.<sup>50</sup> It was noted that the technique is capable of rapid analysis within minutes of sectioning the tissue.

A few reports have also applied FTIR imaging for diagnosing breast diseases. Breast tumor tissues were characterized by both FTIR Imaging and point mapping techniques and advantages over the other were evaluated.<sup>51</sup> Similar comparisons had previously been reported for polymeric materials, analyzing both static and dynamic samples.<sup>52</sup> Comparison images from the two methods, imaging data provided a clearer structure in the tumor area than the data obtained from point mapping. Since breast tumor cells are  $\sim 10\text{ }\mu\text{m}$  in diameter, point mapping data (with an aperture of  $30\text{ }\mu\text{m}$ ) would always contain the spectrum of tumor cells as well as from the contributions of other components surrounding the cells. The study clearly indicated that the conventional point mapping approach can fail to detect a small number of malignant cells due to its poor resolution capabilities. Nevertheless, the contamination problem, i.e., the spectral contributions of other components surrounding the cell is found to be less severe in case of ductal carcinoma in situ (DCIS). The study illustrates the need for matching the appropriate level

of spatial resolution to the task. While the 30  $\mu\text{m}$  resolution may be appropriate for some applications, it was clearly insufficient for detecting smaller numbers of cells.

Artificial network and K-means cluster analysis have also been employed for the classification of FTIR imaging data from normal and malignant immortalized human breast cell lines.<sup>53</sup> Normal cells, carcinoma cells, mixed normal and carcinoma cells were used. Differences in the spectral backgrounds between the training and test data were observed, which confounds the reproducibility of recorded spectra and, thus, causes the classifier to fail. Using rejection thresholds in the application of the ANN classifier was reported to be helpful in identifying doubtful classifications. Another study<sup>54</sup> reported imaging fibroadenoma, a benign breast tumor. Data were evaluated using unsupervised cluster analysis by utilizing two spectral regions, namely 1000-1500 and 2800-3000  $\text{cm}^{-1}$ . The distribution of four main tissue components—epithelium, retro nuclear basal epithelial regions, mantle zone and distant connective tissue were visualized. The spectral features from each component were discussed in detail. Furthermore, comparing epithelia from fibroadenoma and DCIS, the authors determined that subtle distinctions between the IR characteristics of these two are reproducible. The initial study used tissue from a single patient.

The work was recently extended<sup>55</sup> to diagnose benign and malignant lesions from 22 patients. The study utilized only spectra from well-defined tumor areas owing to the heterogeneity of tissues. Based on the cluster analysis and on comparison with the H & E images, four classes of distinct breast tissue spectra were identified - fibroadenoma (FA), ductal carcinoma in situ (DCIS), connective tissue and adipose tissue. Further, ANNs were developed as an automated classifier to differentiate the four classes. All spectra of connective tissue and adipose tissue were classified correctly, where the spectral features are clearly different from each other and from tumors as well. Differentiating fibroadenoma from DCIS was more difficult. A toplevel/sublevel strategy was further applied and was able to differentiate 93% between fibroadenoma and DCIS spectra by employing principal component analysis. From the mean spectra, it was found that the DCIS has more lipid content than the fibroadenoma. Invasive ductal carcinoma (IDC) could not be well characterized due to contamination from surrounding cells, illustrating the limited spatial resolution.

### Cervical Cancer

The cervix is the lower part of the uterus (womb) in which two major types of cancers occur: squamous cell carcinoma and adenocarcinoma. About 80% to 90% of cervical cancers are squamous cell carcinomas, and the remaining 10% to 20% are adenocarcinomas. Less commonly, cervical cancers have features of both squamous cell carcinomas and adenocarcinomas. These are called adenosquamous carcinomas or mixed carcinomas. Typically, the Papanicolaou (Pap) test checks for changes in the exfoliated cells of cervix to find the presence of any infection, abnormal (unhealthy) cervical cells, or cervical cancer. FTIR spectroscopy, micro spectroscopy and FTIR imaging have been widely utilized to study cervical cancer and to perform the same function using computer analyses of spectra.<sup>26, 56-60</sup> While the first reports in diagnosing cervical cancer are now generally not regarded as leading to solutions,<sup>56</sup> two groups have provided definitive proof of the potential of IR spectroscopy by careful microscopy studies.<sup>26, 57, 45, 59, 60</sup>

While FTIR images of the amide I and  $\nu_{\text{asy}}$   $\text{PO}_2^-$  bands with H&E stained image were compared and only a rough correlation with the pathological features or cell types were obtained, cluster

maps of two, five and eight clusters resulting from UHC analysis for the whole spectrum demonstrated good segmentation. In five clusters, most cell types are apparent including superficial (1), intermediate (2), parabasal (3), and connective tissue (5) upon correlation with the stained image. As in univariate images, the connective tissue region (5) is split in to two clusters. Furthermore, by comparing between the UHC analysis of the whole spectrum and only the amide I region, authors demonstrated that minimizing the spectral region for analysis and using fewer clusters does not lead to the loss of useful information. Both univariate FTIR and multivariate images of the sample with several endocervical ducts within the connective tissue were shown. These endocervical ducts lined with columnar endocervical cells were apparent in all those images, in particular even with two clusters.

Cultures derived from cervical cancer cells (HeLa) are one of the most popular model systems and have been studied using FTIR imaging.<sup>61</sup> The cells were directly grown as sparse monolayers onto low-e slides. FTIR image of amide I band region was shown; where large differences in spectral intensities associated with the cells were observed even though these cells are from a homogeneous and exponential cell culture. Cluster analyses of normalized spectra shows distinct differences that were not appreciated in the univariate image. Similarly,<sup>62</sup> IR imaging with fuzzy C- means clustering and hierarchical cluster analysis were utilized to study the thin sections of cervix uteri encompassing normal, precancerous and squamous cell carcinoma. These studies demonstrate that IR imaging, in combination with multivariate techniques, is capable of segmenting cervical tissues in a manner that is comparable to H&E stained image differentiation and is significantly more sensitive in terms of the chemical composition of the cells – whether it be due to metabolic or disease reasons.

## Prostate

Prostate cancer is the most prevalent internal cancer in the US.<sup>63</sup> Hence, its pathologic diagnosis and correct interpretation of disease state is crucial.<sup>64</sup> FTIR imaging has been proposed as solution that can potentially help pathologists by providing an objective and reproducible assessment of disease in a manner that is easily understood by clinicians. It is also a good model system for the development of FTIR imaging protocols. We first review progress in the field and then describe efforts in our and collaborator's laboratories towards formulating a practical algorithm for prostate cancer pathology. While a number of studies examined human prostate tissue with IR spectroscopy<sup>65-68</sup> microscopy approaches have recently been extensively utilized to study both fundamental properties of prostate tissue and to determine structural units in normal and disease states.<sup>69-75</sup> An understanding of the tissue is now emerging as a result of these studies. While the fundamental properties of the tissue are being examined, we have focused on developed statistically validated diagnostic methods.

We have utilized high throughput imaging with the express purpose of correlating spectra to clinical practice.<sup>39, 64, 76</sup> It is instructive to first examine the approaches of some previous studies and then describe our approach in some detail. A variety of techniques have been reported for analyzing prostate tissue, including unsupervised multivariate data analysis techniques such as agglomerative hierarchical clustering (AH), fuzzy C-means (FCM), or k-means (KM) clustering to construct infrared spectral maps of tissue structures.<sup>77</sup> The results from these multivariate techniques confirmed the standard histopathological techniques and found out to be helpful for identifying and discriminating the tissues structures. Agglomerative hierarchical clustering was

found to be the best method among the cluster imaging methods in terms of segmenting the tissue. While these techniques comprise one end of the approach in using large spectral regions and completely objective methods, the other extreme has also proven to be useful. In the second paradigm, careful examination of the spectral data yields some measures that prove useful. For example, the ratio of peak areas at  $1030$  and  $1080\text{ cm}^{-1}$ , corresponding to the glycogen and phosphate vibrations respectively were utilized as a diagnostic marker for the differentiation of benign from malignant cells.<sup>69</sup> Authors summarized that the use of this ratio in association with FTIR spectral imaging provides a basis for estimating areas of malignant tissue within defined regions of a specimen. While it may be argued that the former is not based on clinical knowledge and is more suited for discovery, it also involves the choice of selecting specific number of clusters and their subsequent interpretation. The latter is based on a single parameter whose utility for universal diagnoses remains to be tested. Nevertheless, these studies indicate that both approaches provide information about the tissue that is useful.

Our approach has used elements from both pattern recognition and spectroscopic analyses of univariate measures.<sup>39,76</sup> In all cases, one starts with the acquired imaging data (figure 4). Since the data set is large (typically 10-1000 GB), it is advisable to reduce the dimensionality of data using some numerical procedure. Compression algorithms, principal components analyses or simply storing only the information needed for classification (if the algorithm is known) is useful. We sought expressly to relate the recorded IR imaging data to clinical knowledge base. Hence we started with a model that is derived from clinical practice. Clearly, the approach limits the discovery of new knowledge but it assures the clinician that all quantities of importance for diagnoses will be considered. The acquired data is labeled with known cell identity or disease states. These pixels are best identified by a combination of very careful manual labeling and test for absorbance fidelity.<sup>78</sup> Spectra from the label regions are employed via average values, medians and standard deviation analyses to determine a set of spectral features that are descriptive of the major features of all spectra. We first note that the characteristic IR absorbance spectra of ten histological classes comprising prostate tissue look similar. Though small differences in spectral features were observed at many frequencies, summary statistics are limited in their examination of spectra for classification. Further, the small differences indicate that noise and biological variability may render univariate measures less reliable. The large number of classes usually implies that univariate analyses cannot distinguish all histological classes present in the tissues and hence the need for multivariate analyses is apparent. Here the similarity of the spectral features for all classes works in our favor. Very similar baseline points are obtained from an analysis of all spectra and only subtle feature differences are noted to distinguish the various class spectra. Hence, unknown spectra can be processed in the same specified manner, without introducing any bias. Each of these features is termed a metric to denote that it is a useful measure of the spectrum. Individual metrics can allow segmentation of various tissue types if they are sufficiently different in a sampled population.

We then employ the equivalent of a t-test in that the overlap between the absorbance distributions of metrics is determined and equated to the error in prediction. The metrics are arranged in the order of increasing overlap. Hence, we have an ordered set that differentiates at least two classes. To obtain overall accuracy, we employ a modified Bayesian algorithm to provide the probability of each class for every pixel. This fuzzy result is employed to determine the area under the curve (AUC) of a receiver operating characteristic (ROC) curve. The ROC

curve is built from accepting the probability of each class at an increasing threshold that varies between 0 and 1. For optimized threshold values, the fuzzy classification is turned into a classified image, where each pixel is assigned a distinct class. We note that the method incorporates analysis of all spectral features, a selection of the best features based on statistical analysis of data and an optimal prediction of the class of each pixel based on an objective selection rule from the fuzzy classification. The method is very powerful in that it employs spectral features that are ordinarily employed by spectroscopists as metrics, which permits a spectroscopic analysis of the basis of decision-making. Further, the method explicitly obtains the fuzzy rule data for final classification. The value of the rule data for each class is actually the probability of belonging to the class without consideration for the prior prevalence of the class. Hence, the method can allow direct comparisons between performances for different classes. The dependence of the process on various experimental parameters has also been reported.

The complication inherent in translating the results from small data set of patients to clinical applications is well recognized in the spectroscopy community. The variability in data, arising from variations within and between patients, sample preparation and handling, is likely to provide noisy estimates of performance. Hence, statistical stability may be obtained by examining a large number of samples. Similarly, large number of patients may be employed to provide calibration models, likely improving the robustness of the developed algorithm. We have described a high throughput sampling method from tissues.<sup>14, 39, 76</sup> Briefly, the approach uses a combinatorial sampling of tissue type and pathology to first acquire small sections of tissues from large archival cases. These small sections are arranged in a grid pattern and placed on the same substrate. The sample is termed a tissue microarray to reflect the similarity with cDNA microarrays. For spectroscopic imaging and the development of automated algorithms, the approach represents a large number of cases that can be used both for accurate prediction algorithm building and for extensive validations. The same approach is likely to prove useful for extensions to determining pathology. Figure 5 demonstrates the typical workflow of a validation algorithm and methods used for statistical comparison. We strongly suggest a variety of methods for measuring performance as each method has its own advantages and disadvantages. For example, summary measures from ROC curves only provide information about accuracy but do not provide which class the inaccuracies arise from. Similarly, confusion matrices provide cross-class information but do not provide global performance measures in the mold of ROC curves.

## **OUTLOOK**

FTIR imaging has experienced rapid growth in the past 10 years and is increasingly being applied to biomedical tissue, especially for the analyses of cancer. The major trends emerging in instrumentation include faster detectors and novel modes of data collection (e.g. time –resolved imaging), of sampling (e.g. ATR) and application areas. For biomedical samples, the information content is quite rich and is often available through simple univariate analysis. For more complex applications, e.g. cancer diagnoses, the data acquisition, sampling and data analyses must be integrated in a coherent manner to provide a practical solution. We anticipate that the technology and its application to biomedical problem will continue to grow with the cooperation of instrument manufacturers, applications scientists, numerical methods developers and communities that can utilize the information effectively, e.g. pathologists or surgeons.

## References

- 1.Gore, R. C.; Barnes, R. B.; Petersen, E., Infrared Absorption of Aqueous Solutions of Organic Acids and Their Salts. *Anal. Chem.* **1949**, 21, (3), 382-386.
- 2.Kwiatkoski, J. M.; Reffner, J. A., FT-IR microspectrometry advances. *Nature* **1987**, 328, (6133), 837-838.
- 3.Koenig, J. L., *Microspectroscopic imaging of polymers*. American Chemical Society Washington, DC: 1998.
- 4.Williams, D. K.; Schwartz, R. L.; Bartick, E. G., Analysis of latent fingerprint deposits by infrared microspectroscopy. *Appl Spectrosc* **2004**, 58, (3), 313-6.
- 5.Petricch, W., Mid-Infrared and Raman Spectroscopy for Medical Diagnostics *Applied Spectroscopy Reviews* **2001**, 36, (2), 181-237.
- 6.Naumann, D., FT-infrared and FT-Raman Spectroscopic in Biomedical Research *Applied Spectroscopy Reviews* **2001**, 36, (2), 239-298.
- 7.Lewis, E. N.; Levin, I. W., Vibrational Spectroscopic Microscopy: Raman, Near-Infrared and Mid-Infrared Imaging Techniques. *Microscopy and Microanalysis* **1995**, 1, (01), 35-46.
- 8.Lewis, E. N.; Treado, P. J.; Reeder, R. C.; Story, G. M.; Dowrey, A. E.; Marcott, C.; Levin, I. W., Fourier transform spectroscopic imaging using an infrared focal-plane array detector. *Anal Chem* **1995**, 67, (19), 3377-81.
- 9.Bhargava, R.; Wang, S. Q.; Koenig, J. L., FTIR microspectroscopy of polymeric systems. *Advances in Polymer Science* **2003**, 163, 137-191.
- 10.Mendelsohn, R.; Flach, C. R.; Moore, D. J., Determination of molecular conformation and permeation in skin via IR spectroscopy, microscopy, and imaging. *Biochimica et Biophysica Acta (BBA) - Biomembranes* **2006**, 1758, (7), 923-933.
- 11.Garidel, P.; Boese, M., Mid infrared microspectroscopic mapping and imaging: A bioanalytical tool for spatially and chemically resolved tissue characterization and evaluation of drug permeation within tissues. *Microsc Res Tech* **2007**, 70, (4), 336-349.
- 12.Lewis, E. N.; Gorbach, A. M.; Marcott, C.; Levin, I. W., High-fidelity Fourier transform infrared spectroscopic imaging of primate brain tissue. *Applied Spectroscopy* **1996**, 50, (2), 263-269.
- 13.Lewis, E. N.; Kidder, L. H.; Levin, I. W.; Kalasinsky, V. F.; Hanig, J. P.; Lester, D. S., Applications of fourier transform infrared imaging microscopy in neurotoxicity. *Ann N Y Acad Sci* **1997**, 820, 234-46; discussion 246-7.
- 14.Levin, I. W.; Bhargava, R., Fourier transform infrared vibrational spectroscopic imaging: integrating microscopy and molecular recognition. *Annu Rev Phys Chem* **2005**, 56, 429-74.
- 15.Snively, C. M.; Koenig, J. L., Characterizing the Performance of a Fast FT-IR Imaging Spectrometer. *Applied Spectroscopy* **1999**, 53, (2), 170-177.
- 16.Bhargava, R.; Levin, I. W., Fourier transform infrared imaging: theory and practice. *Anal. Chem* **2001**, 73, (21), 5157-5167.
- 17.Snively, C. M.; Katzenberger, S.; Oskarsdottir, G.; Lauterbach, J., Fourier-transform infrared imaging using a rapid-scan spectrometer. *Opt. Lett* **1999**, 24, 1841-1843.
- 18.Huffman, S. W.; Bhargava, R.; Levin, I. W., Generalized Implementation of Rapid-Scan Fourier Transform Infrared Spectroscopic Imaging. *Applied Spectroscopy* **2002**, 56, (8), 965-969.
19. *Spectrochemical Analysis using Infrared Multichannel Detectors*, Bhargava, R.

*Levin, I. W. (Eds).* Blackwell Publishing, Sheffield, UK: 2005.

20.Bhargava, R.; Levin, I. W., Time-resolved Fourier transform infrared spectroscopic imaging. *Appl Spectrosc* **2003**, 57, (4), 357-66.

21.Bhargava, R.; Levin, I. W., Noninvasive Imaging of Molecular Dynamics in Heterogeneous Materials. *Macromolecules* **2003**, 36, (1), 92-96.

22.Bhargava, R.; Levin, I. W., Gram-Schmidt orthogonalization for rapid reconstructions of Fourier transform infrared spectroscopic imaging data. *Appl Spectrosc* **2004**, 58, (8), 995-1000.

23.Bhargava, R.; Levin, I. W., Enhanced Time-Resolved Fourier Transform Infrared Spectroscopic Imaging for Reversible Dynamics. *J. Phys. Chem. A* **2004**, 108, (18), 3896-3901.

24.O'Leary, T. J.; Engler, W. F.; Ventre, K. M., Infrared Microspectroscopy of Human Tissue. *Applied Spectroscopy* **1989**, 43, (6), 1095-1097.

25.Marcott, C.; Story, G. M.; Dukor, R. K., Infrared Spectral Imaging of H&E-Stained Breast Tissue Biopsies. *Microscopy and Microanalysis* **2004**, 10, (S02), 182-183.

26.Romeo, M.; Mohlenhoff, B.; Jennings, M.; Diem, M., Infrared micro-spectroscopic studies of epithelial cells. *Biochimica et Biophysica Acta (BBA) - Biomembranes* **2006**, 1758, (7), 915-922.

27.Patterson, B. M.; Havrilla, G. J., Attenuated Total Internal Reflection Infrared Microspectroscopic Imaging Using a Large-Radius Germanium Internal Reflection Element and a Linear Array Detector. *Applied Spectroscopy* **2006**, 60, (11), 1256-1266.

28.Sommer, A. J.; Tisinger, L. G.; Marcott, C.; Story, G. M., Attenuated Total Internal Reflection Infrared Mapping Microspectroscopy Using an Imaging Microscope. *Applied Spectroscopy* **2001**, 55, (3), 252-256.

29.Otts, D. B.; Zhang, P.; Urban, M. W., High Fidelity Surface Chemical Imaging at 1000 nm Levels: Internal Reflection IR Imaging (IRIRI) Approach. *Langmuir* **2002**, 18, (17), 6473-6477.

30.Chan, K. L. A.; Kazarian, S. G., New opportunities in micro- and macro-attenuated total reflection infrared spectroscopic imaging: Spatial resolution and sampling versatility. *Applied Spectroscopy* **2003**, 57, (4), 381-389.

31.Chan, K. L.; Hammond, S. V.; Kazarian, S. G., Applications of attenuated total reflection infrared spectroscopic imaging to pharmaceutical formulations. *Anal Chem* **2003**, 75, (9), 2140-6.

32.Colley, C. S.; Kazarian, S. G.; Weinberg, P. D.; Lever, M. J., Spectroscopic imaging of arteries and atherosclerotic plaques. *Biopolymers* **2004**, 74, (4), 328-35.

33.Kazarian, S. G.; Chan, K. L. A., Applications of ATR-FTIR spectroscopic imaging to biomedical samples. *Biochimica et Biophysica Acta (BBA) - Biomembranes* **2006**, 1758, (7), 858-867.

34.van der Weerd, J.; Andrew Chan, K. L.; Kazarian, S. G., An innovative design of compaction cell for in situ FT-IR imaging of tablet dissolution. *Vibrational Spectroscopy* **2004**, 35, (1-2), 9-13.

35.van der Weerd, J.; Kazarian, S. G., Combined approach of FTIR imaging and conventional dissolution tests applied to drug release. *J Control Release* **2004**, 98, (2), 295-305.

36.Chan, K. L.; Kazarian, S. G., Fourier transform infrared imaging for high-throughput analysis of pharmaceutical formulations. *J Comb Chem* **2005**, 7, (2), 185-9.

37.Chan, K. L.; Kazarian, S. G., ATR-FTIR spectroscopic imaging with expanded field of view to study formulations and dissolution. *Lab Chip* **2006**, 6, (7), 864-70.

38.Snively, C. M.; Oskarsdottir, G.; Lauterbach, J., Chemically sensitive parallel analysis of combinatorial catalyst libraries. *Catalysis Today* **2001**, 67, (4), 357-368.

39.Fernandez, D. C.; Bhargava, R.; Hewitt, S. M.; Levin, I. W., Infrared spectroscopic imaging for histopathologic recognition. *Nat Biotechnol* **2005**, 23, (4), 469-74.

40.Boskey, A. L.; Mendelsohn, R., Infrared spectroscopic characterization of mineralized tissues. *Vibrational Spectroscopy* **2005**, 38, (1-2), 107-114.

41.Posner, A. S.; Duyckaerts, G., Infrared study of the carbonate in bone, teeth and francolite. *Experientia* **1954**, 10, (10), 424-5.

42.Boskey, A.; Mendelsohn, R., Infrared analysis of bone in health and disease. *J Biomed Opt* **2005**, 10, (3), 031102.

43.Boskey, A. L.; Goldberg, M.; Kulkarni, A.; Gomez, S., Infrared imaging microscopy of bone: Illustrations from a mouse model of Fabry disease. *Biochimica et Biophysica Acta (BBA) - Biomembranes* **2006**, 1758, (7), 942-947.

44.Faibis, D.; Gomes, A.; Boivin, G.; Binderman, I.; Boskey, A., Infrared imaging of calcified tissue in bone biopsies from adults with osteomalacia. *Bone* **2005**, 36, (1), 6-12.

45.Bambery, K. R.; Schultke, E.; Wood, B. R.; MacDonald, S. T. R.; Ataelmannan, K.; Griebel, R. W.; Juurlink, B. H. J.; McNaughton, D., A Fourier transform infrared microspectroscopic imaging investigation into an animal model exhibiting glioblastoma multiforme. *Biochimica et Biophysica Acta (BBA) - Biomembranes* **2006**, 1758, (7), 900-907.

46. American Brian Tumor Association.

47.Krafft, C.; Shapoval, L.; Sobottka, S. B.; Schackert, G.; Salzer, R., Identification of primary tumors of brain metastases by infrared spectroscopic imaging and linear discriminant analysis. *Technol Cancer Res Treat* **2006**, 5, (3), 291-8.

48.Amharref, N.; Beljebbar, A.; Dukic, S.; Venteo, L.; Schneider, L.; Pluot, M.; Vistelle, R.; Manfait, M., Brain tissue characterisation by infrared imaging in a rat glioma model. *Biochimica et Biophysica Acta (BBA) - Biomembranes* **2006**, 1758, (7), 892-899.

49.Kneipp, J.; Lasch, P.; Baldauf, E.; Beekes, M.; Naumann, D., Detection of pathological molecular alterations in scrapie-infected hamster brain by Fourier transform infrared (FT-IR) spectroscopy. *Biochimica et Biophysica Acta (BBA) - Molecular Basis of Disease* **2000**, 1501, (2-3), 189-199.

50.Kidder, L. H.; Kalasinsky, V. F.; Luke, J. L.; Levin, I. W.; Lewis, E. N., Visualization of silicone gel in human breast tissue using new infrared imaging spectroscopy. *Nat Med* **1997**, 3, (2), 235-237.

51.Fabian, H.; Lasch, P.; Boese, M.; Haensch, W., Mid-IR microspectroscopic imaging of breast tumor tissue sections. *Biopolymers - Biospectroscopy Section* **2002**, 67, (4-5), 354-357.

52.Bhargava, R.; Wall, B. G.; Koenig, J. L., Comparison of the FT-IR mapping and imaging techniques applied to polymeric systems. *Applied Spectroscopy* **2000**, 54, 470-479.

53.Zhang, L.; Small, G. W.; Haka, A. S.; Kidder, L. H.; Lewis, E. N., Classification of Fourier transform infrared microscopic imaging data of human breast cells by cluster analysis and artificial neural networks. *Appl Spectrosc* **2003**, 57, (1), 14-22.

54.Fabian, H.; Lasch, P.; Boese, M.; Haensch, W., Infrared microspectroscopic imaging of benign breast tumor tissue sections. *Journal of Molecular Structure* **2003**, 661-662, (1-3), 411-417.

55.Fabian, H.; Thi, N. A. N.; Eiden, M.; Lasch, P.; Schmitt, J.; Naumann, D., Diagnosing benign and malignant lesions in breast tissue sections by using IR-microspectroscopy. *Biochimica et Biophysica Acta (BBA) - Biomembranes* **2006**, 1758, (7), 874-882.

56.Wong, P. T.; Wong, R. K.; Caputo, T. A.; Godwin, T. A.; Rigas, B., Infrared spectroscopy of exfoliated human cervical cells: evidence of extensive structural changes during carcinogenesis. *Proc Natl Acad Sci U S A* **1991**, 88, (24), 10988-92.

57.Boydston-White, S.; Romeo, M.; Chernenko, T.; Regina, A.; Miljkovic, M.; Diem, M., Cell-cycle-dependent variations in FTIR micro-spectra of single proliferating HeLa cells: Principal component and artificial neural network analysis. *Biochimica et Biophysica Acta (BBA) - Biomembranes* **2006**, 1758, (7), 908-914.

58.Walsh, M. J.; German, M. J.; Singh, M.; Pollock, H. M.; Hammiche, A.; Kyrgiou, M.; Stringfellow, H. F.; Paraskevaidis, E.; Martin-Hirsch, P. L.; Martin, F. L., IR microspectroscopy: potential applications in cervical cancer screening. *Cancer Letters* **2007**, 246, (1-2), 1-11.

59.Bambery, K. R.; Wood, B. R.; Quinn, M. A.; McNaughton, D., Fourier transform infrared imaging and unsupervised hierarchical clustering applied to cervical biopsies. *Australian Journal of Chemistry* **2004**, 57, (12), 1139-1143.

60.Wood, B. R.; Chiriboga, L.; Yee, H.; Quinn, M. A.; McNaughton, D.; Diem, M., Fourier transform infrared (FTIR) spectral mapping of the cervical transformation zone, and dysplastic squamous epithelium. *Gynecol Oncol* **2004**, 93, (1), 59-68.

61.Diem, M.; Romeo, M. J.; Boydston-White, S.; Matthaus, C., "IR Spectroscopic Imaging: from Cells to Tissue" in "Spectrochemical Analysis using Infrared Multichannel Detectors", R.Bhargava and I.W.Levin, Editors,. Blackwell Publishing, Sheffield, UK: 2005.

62.Steller, W.; Einenkel, J.; Horn, L. C.; Braumann, U. D.; Binder, H.; Salzer, R.; Krafft, C., Delimitation of squamous cell cervical carcinoma using infrared microspectroscopic imaging. *Anal Bioanal Chem* **2006**, 384, (1), 145-54.

63. [http://seer.cancer.gov/csr/1975\\_2004/results\\_single/sect\\_01\\_table.01.pdf](http://seer.cancer.gov/csr/1975_2004/results_single/sect_01_table.01.pdf). 2007.

64. Bhargava, R., *Anal Bioanal Chem* (in press).

65.Paluszkiewicz, C.; Kwiatek, W. M., Analysis of human cancer prostate tissues using FTIR microspectroscopy and SRIXE techniques. *Journal of Molecular Structure* **2001**, 565, 329-334.

66.Bhargava, R.; Fernandez, D. C.; Schaeberle, M. D.; Levin, I. W., Theory and application of gain ranging to Fourier transform infrared spectroscopic Imaging. *Applied Spectroscopy* **2001**, 55, (12), 1580-1589.

67.Hsu, H. S.; Lin, S. Y.; Li, M. J.; Liang, R. C., Ultrastructural and biophysical studies on protein conformations of epithelium and stroma in benign prostatic hyperplasia before and after transurethral resection of the prostate. *Ultrastructural Pathology* **2002**, 26, (3), 137-141.

68.Li, M. J.; Hsu, H. S.; Liang, R. C.; Lin, S. Y., Infrared microspectroscopic detection of epithelial and stromal growth in the human benign prostatic hyperplasia. *Ultrastructural Pathology* **2002**, 26, (6), 365-370.

69.Gazi, E.; Dwyer, J.; Gardner, P.; Ghanbari-Siahkali, A.; Wade, A. P.; Miyan, J.; Lockyer, N. P.; Vickerman, J. C.; Clarke, N. W.; Shanks, J. H.; Scott, L. J.; Hart, C. A.; Brown, M., Applications of Fourier transform infrared microspectroscopy in studies of benign prostate and prostate cancer. A pilot study. *J Pathol* **2003**, 201, (1), 99-108.

70.Gazi, E.; Dwyer, J.; Lockyer, N.; Gardner, P.; Vickerman, J. C.; Miyan, J.; Hart, C. A.; Brown, M.; Shanks, J. H.; Clarke, N., The combined application of FTIR microspectroscopy and ToF-SIMS imaging in the study of prostate cancer. *Faraday Discuss* **2004**, 126, 41-59; discussion 77-92.

71.Gazi, E.; Dwyer, J.; Lockyer, N. P.; Miyan, J.; Gardner, P.; Hart, C.; Brown, M.; Clarke, N. W., Fixation protocols for subcellular imaging by synchrotron-based Fourier transform infrared microspectroscopy. *Biopolymers* **2005**, 77, (1), 18-30.

72.Gazi, E.; Dwyer, J.; Lockyer, N.; Gardner, P.; Miyan, J.; Hart, C.; Brown, M.; Clarke, N., A study of cytokinetic and motile prostate cancer cells using synchrotron based FTIR-microspectroscopic imaging. *Vibrational spectroscopy* **2005**, 38, (1-2), 193-201.

73.German, M. J.; Hammiche, A.; Ragavan, N.; Tobin, M. J.; Cooper, L. J.; Matanhelia, S. S.; Hindley, A. C.; Nicholson, C. M.; Fullwood, N. J.; Pollock, H. M.; Martin, F. L., Infrared spectroscopy with multivariate analysis potentially facilitates the segregation of different types of prostate cell. *Biophysical Journal* **2006**, 90, (10), 3783-3795.

74.Gazi, E.; Baker, M.; Dwyer, J.; Lockyer, N. P.; Gardner, P.; Shanks, J. H.; Reeve, R. S.; Hart, C. A.; Clarke, N. W.; Brown, M. D., A correlation of FTIR spectra derived from prostate cancer biopsies with Gleason grade and tumour stage. *European Urology* **2006**, 50, (4), 750-761.

75.Wolkers, W. F.; Balasubramanian, S. K.; Ongstad, E. L.; Zec, H. C.; Bischof, J. C., Effects of freezing on membranes and proteins in LNCaP prostate tumor cells. *Biochimica Et Biophysica Acta-Biomembranes* **2007**, 1768, (3), 728-736.

76.Bhargava, R.; Fernandez, D. C.; Hewitt, S. M.; Levin, I. W., High throughput assessment of cells and tissues: Bayesian classification of spectral metrics from infrared vibrational spectroscopic imaging data. *Biochimica et Biophysica Acta (BBA) - Biomembranes* **2006**, 1758, (7), 830-845.

77.Lasch, P.; Diem, M.; Naumann, D. In *FT-IR microspectroscopic imaging of prostate tissue sections*, Biomedical Vibrational Spectroscopy and Biohazard Detection Technologies, San Jose, CA, USA, 2004; SPIE: San Jose, CA, USA, 2004; pp 1-9.

78.Bhargava, R.; Hewitt, S. M.; Levin, I. W., Reply to Unrealistic expectations for IR microspectroscopic imaging. *Nat Biotech* **2007**, 25, (1), 31-33.

### **SBFP Javelin (Rolling Mode)**

- 64 x 64 bump-bonded: 180 Hz (1996)
- 64 x 64 : 250 Hz to 315 Hz (1996-98)
- 64 x 64 : 430 Hz (2000)
- 64 x 64 : 615 Hz, Triggered Mode (2001)
- Step-scan (1997); rapid-scan (1999) imaging

### **Perkin-Elmer Spotlight**

- 16 x 1 "linear" array (2001)
- ~ 100 spectra/s
- Exceptionally high SNR
- Thermo: 16 x 2 array (2005)

### **NIH256-SBFP (Snapshot Mode)**

- 256 x 256 MBE grown (1997) - NIST
- 256 x 256 : 143 Hz Capable
- Rapid-scan (2000) imaging
- TRS : 10 ms (2002)
- TRS : 0.1 ms resolution (2004)

### **FBI-NIH128-RSC (Snapshot)**

- 128 x 128 MBE: >16 KHz (2003)
- On-chip co-addition
- Advanced software
- Spatial Subset
- Trigger
- Rapid Scan Imaging (2005)
- Potential
  - Rapid scan : 0.06 s acquisition
  - TRS : 40 microsecond
  - Step-scan : High SNR

### **Digilab-SBFP Lancer (Snapshot)**

- 64 x 64 MBE: 3774 Hz (2002)
- Step-scan imaging (2002)
- Digilab "fast" scan ~ 10 s acquisition
- NIH/Akron rapid scan : 0.25 s acquisition

Figure 1. Various MCT FPA detectors employed for FTIR imaging since the first reports using Santa Barbara Focalplane (SBFP) array detectors. The years in parentheses are the first reports of use for FTIR imaging. Perkin-Elmer introduced the concept of utilizing a small linear array for very high signal to noise ratios, an approach that has since been adopted by Thermo. Our research efforts have involved the use of a high end, custom-built detector that allows for fast imaging.

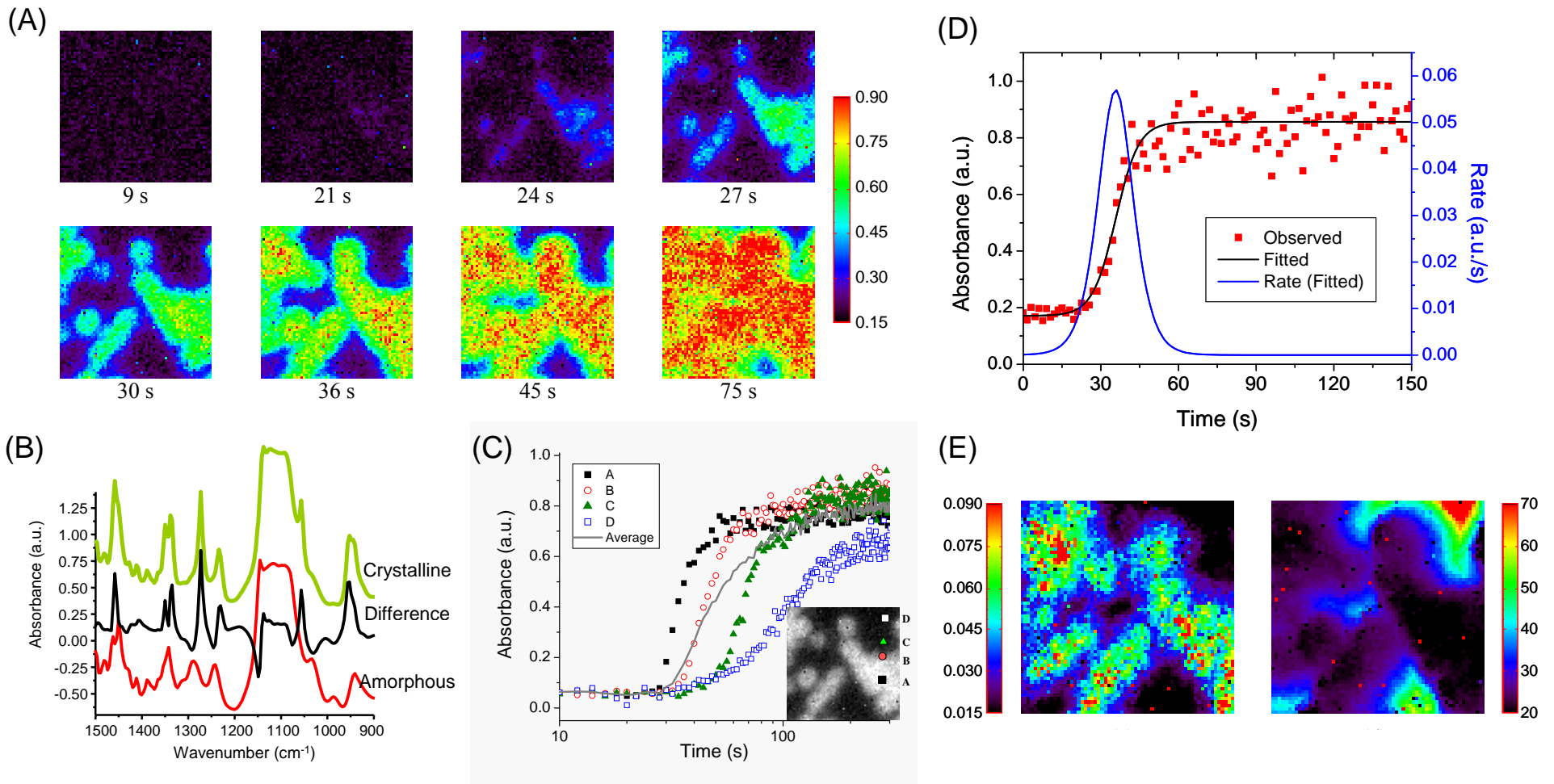


Figure 2. FTIR spectroscopy and imaging permits examination of molecular conformation changes preceding and during polymer crystallization. (A) The distribution of crystalline and amorphous fractions as a function of time for undercooling  $\text{PEO} \sim 13^\circ \text{C}$  below its melting point can be observed by the intensity of any peak that is different (B). The pixels crystallizing first can be analyzed prior to crystal formation for pre-ordering transitions. (C) Different regions of the sample have different kinetics (symbols), which are not apparent in the average spectral change (line). (D) The kinetic data (noisy) can be fit with a smooth curve and the rate of crystallization obtained. (E) spatial variation of crystallization rate (E, left) correlates with the onset of crystallization (E, right). Those regions that start to crystallize late also have a lower rate and lower ultimate purity, likely due to diffusion of impurities.

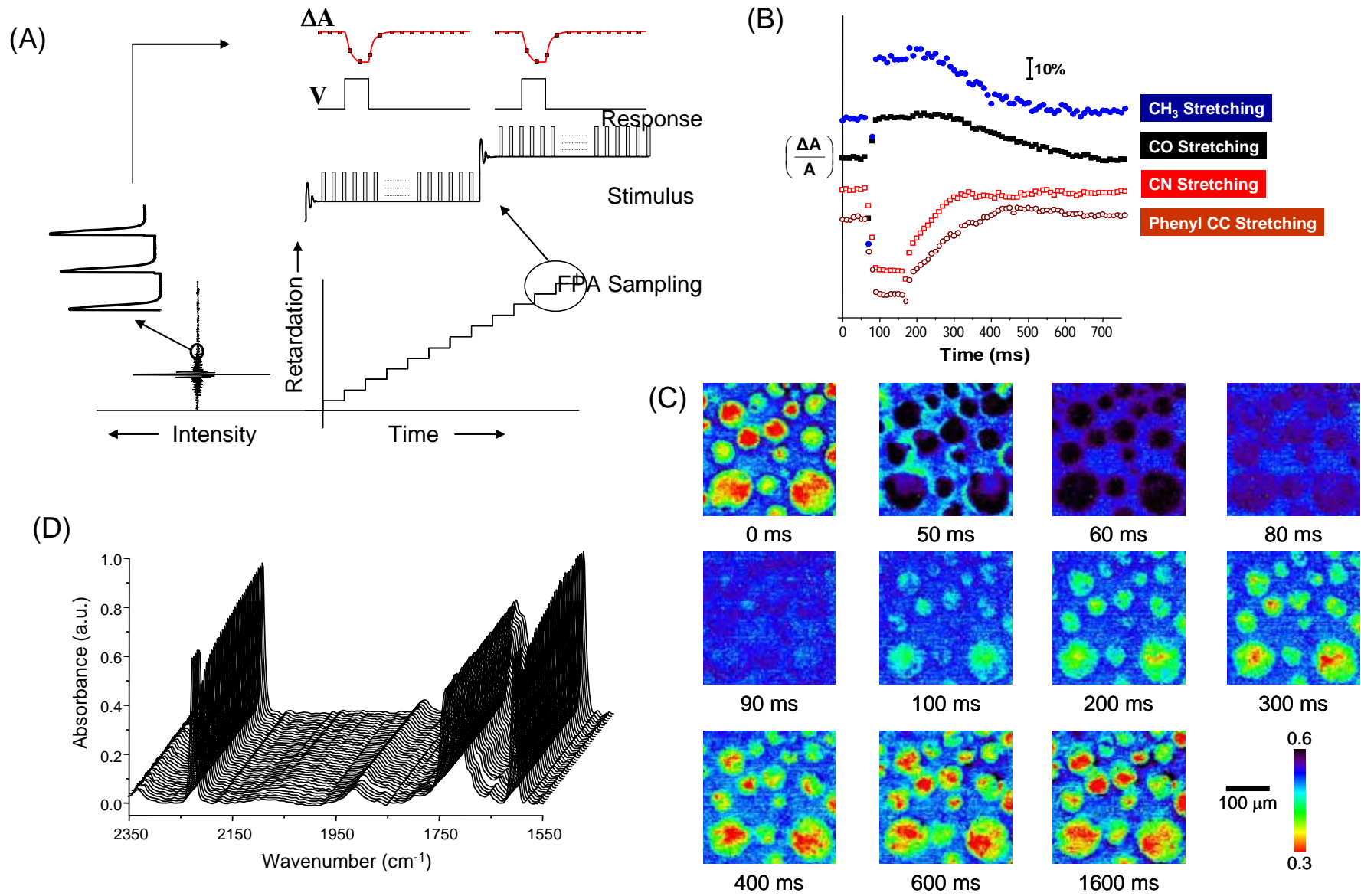


Figure 3. Time-resolved FTIR imaging can provide spatially-resolved, millisecond level dynamics over large sample areas. The operation (A) of the interferometer is similar to that of conventional step scan spectroscopy, except that an entire image is acquired for every sampling point. (B) Various functional groups may be monitored in time at specific pixels or (C) the entire image may be visualized. (D) Entire spectra from pixels may also be observed in the manner of conventional time resolved spectroscopy.

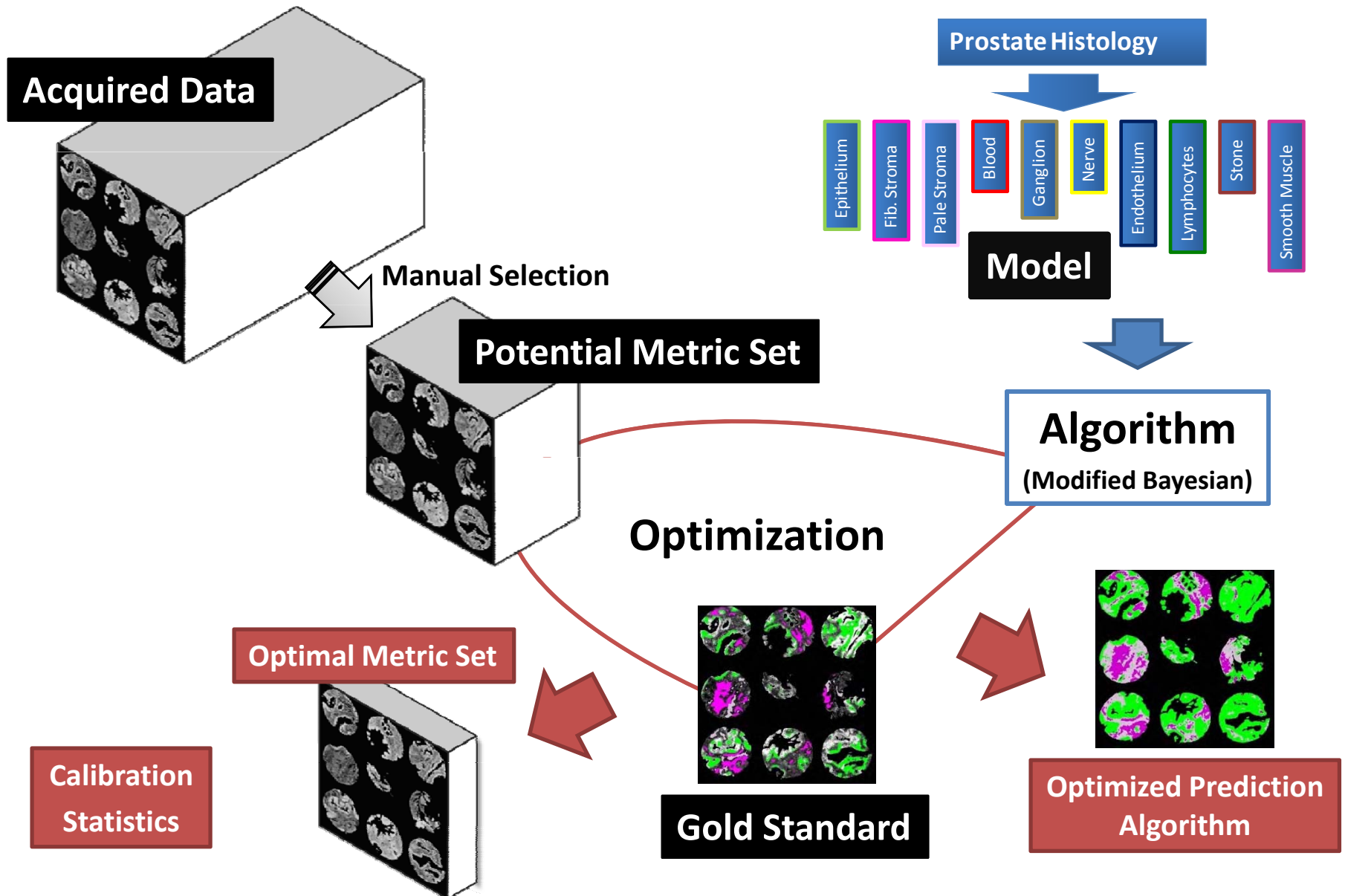
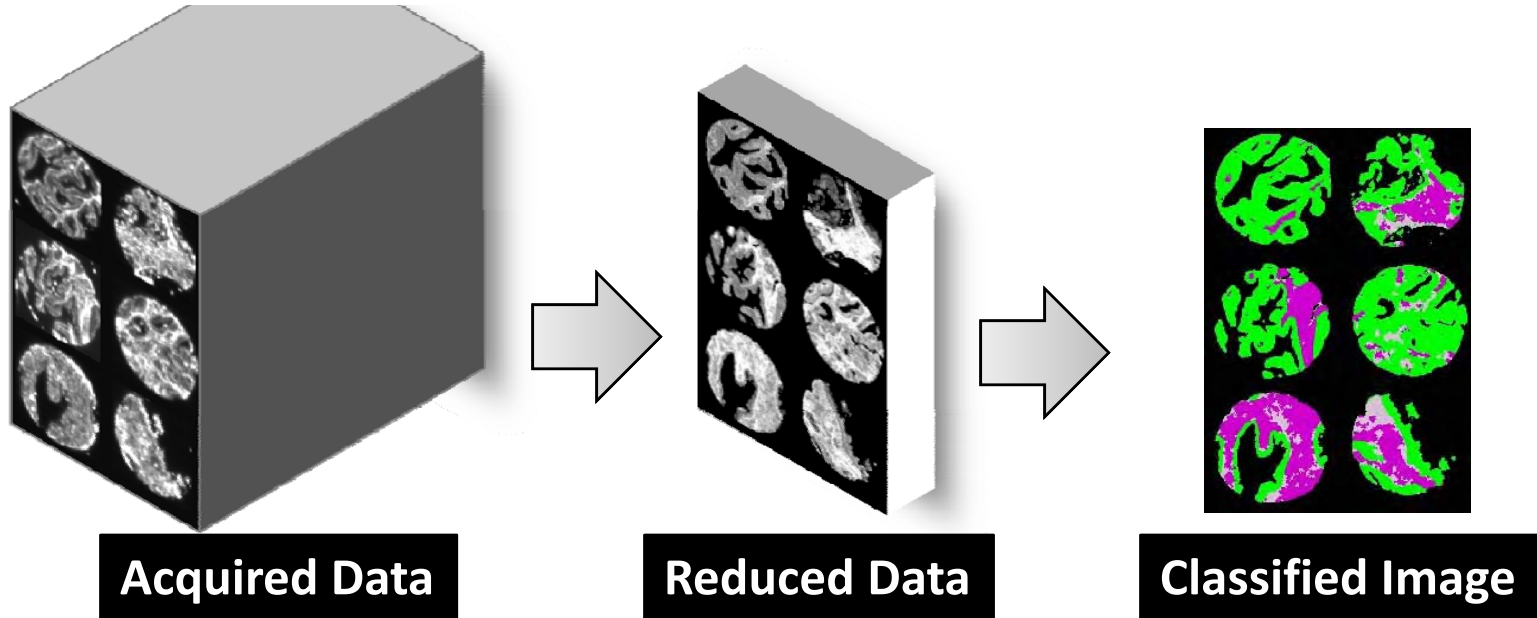
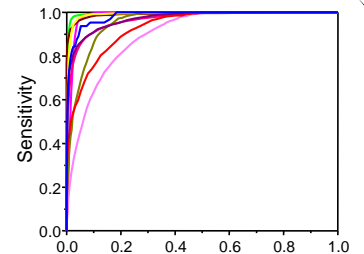


Figure 4. Organization of data into a prediction algorithm involves several steps. Acquired FTIR imaging data (top, left) is reduced by manual selection to a set of features that capture the essential elements of spectra from all tissue types. A model (top, right) is selected for the data and employed to develop an algorithm. The algorithm is applied to the entire metric set and prediction capabilities are optimized. Results of the optimization provide an optimal metric set for validation studies, the parameters of the algorithm to be applied and calibration classification statistics. The optimized algorithm is applied to acquired data without supervision (figure 5).



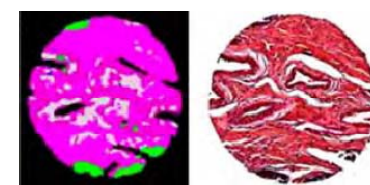
Ground Truth Class \ Result of Classification	EPITHELIUM	MIXED STROMA	FIBROUS STROMA	SMOOTH MUSCLE
EPITHELIUM	95.65	0.16	0.21	0.00
MIXED STROMA	0.00	92.51	0.79	2.76
FIBROUS STROMA	0.19	1.15	93.04	0.69
SMOOTH MUSCLE	0.00	5.53	0.94	94.04

Confusion Matrices



ROC Curves

## Validation/Statistics



Classified Images

Figure 5. Validation or unsupervised application of the developed protocol. FTIR imaging data are acquired (top, left), reduced to the optimal metric set (obtained as in figure 4), which is then converted to a single image that denotes each cell type by a specific color and empty space by black (top, right). Classified images can be compared to ground truth images by using confusion matrices, ROC curves and by comparisons of pixels between images. Statistical measures from these validation tests provide quantifiable results and high confidence in the development of robust algorithms.

# Practical protocols for fast histopathology by Fourier transform infrared spectroscopic imaging

Frances N. Keith, Rohith K. Reddy, and Rohit Bhargava\*

Department of Bioengineering and Beckman Institute for Advanced Science and Technology,  
University of Illinois at Urbana-Champaign  
3216 Digital Computer Lab, MC-278, 1304 W. Springfield Ave., Urbana, IL 61801

## ABSTRACT

Fourier transform infrared (FT-IR) spectroscopic imaging is an emerging technique that combines the molecular selectivity of spectroscopy with the spatial specificity of optical microscopy. We demonstrate a new concept in obtaining high fidelity data using commercial array detectors coupled to a microscope and Michelson interferometer. Next, we apply the developed technique to rapidly provide automated histopathologic information for breast cancer. Traditionally, disease diagnoses are based on optical examinations of stained tissue and involve a skilled recognition of morphological patterns of specific cell types (histopathology). Consequently, histopathologic determinations are a time consuming, subjective process with innate intra- and inter-operator variability. Utilizing endogenous molecular contrast inherent in vibrational spectra, specially designed tissue microarrays and pattern recognition of specific biochemical features, we report an integrated algorithm for automated classifications. The developed protocol is objective, statistically significant and, being compatible with current tissue processing procedures, holds potential for routine clinical diagnoses. We first demonstrate that the classification of tissue type (histology) can be accomplished in a manner that is robust and rigorous. Since data quality and classifier performance are linked, we quantify the relationship through our analysis model. Last, we demonstrate the application of the minimum noise fraction (MNF) transform to improve tissue segmentation.

**Keywords:** Breast Cancer, FT-IR Spectroscopy, Hyperspectral, Histopathology, Imaging, Diagnostics, MNF Transform

## 1. INTRODUCTION

As histologic analysis of biopsied tissue forms the standard in definitive diagnosis of breast lesions, it is estimated that more than 1.6 million women undergo breast biopsies each year in the US alone. Biopsy samples are fixed to ensure tissue stability<sup>1</sup> and then sectioned for staining.<sup>2</sup> Microscopic examinations of stained tissue sections by a trained pathologist are the gold standard used in diagnosing breast cancer.<sup>3</sup> Unfortunately, these evaluations are time consuming<sup>4</sup> and do not always lead to an unequivocal diagnosis. For example, a study of 481 breast cancer patients from 1982-2000 at a regional cancer center indicated that 73% of ductal carcinoma *in situ* (DCIS) patients are referred by a general pathologist to an expert pathologist for review.<sup>5</sup> After review, 43% of these cases received different treatment recommendations. Another study found that 52% of cases referred to a multidisciplinary tumor review board received different surgery recommendations.<sup>6</sup> Clearly, the diagnostic process is sub-optimal. Rapid, objective second opinions are desirable. The use of emerging biological understanding and technologies for diagnoses could provide additional information in tumor evaluation and help make accurate therapy decisions. Further, it is likely that the morphologic parameters of current diagnoses are insufficient and additional information must be added. This information is typically biochemical in nature. For example, staining for human epidermal growth factor receptor 2 (HER2) can identify 25-30% of breast cancers.<sup>7</sup> Such examples of success, unfortunately, are uncommon for cancers in complex tissues. Hence, alternative methods are urgently required to aid diagnostic pathology.

One such means is the use of molecular spectroscopy. For example, Fourier transform infrared (FT-IR) spectroscopy is traditionally used for molecular identifications and biomolecular structure elucidations, but is not currently applied in clinical pathology.<sup>8</sup> An IR spectrum provides a unique molecular fingerprint with a quantitative measure of the molecular bonds present in an examined material.<sup>9</sup> Thus it should give a reproducible measurement of tissue

\* rxb@uiuc.edu; phone 1 217 265 6596; cisl.bioen.uiuc.edu

composition. Tissue, however, is microscopically heterogeneous and the measurement of chemical composition must be made in the context of knowledge of tissue structure (histology).<sup>10</sup> The recent emergence of FT-IR imaging couples spectroscopy and microscopy to permit rapid acquisition of spectra from tens of thousands of pixels at a high spatial resolution. Each pixel (spectrum) typically contains thousands of data points in the mid-IR wavelength region (2–12 μm).<sup>11</sup> Automated classification can then be employed for rapid computerized tissue image analysis, as has been practiced in both the spectral processing and image processing communities. The end goal of the measurement and associated data processing steps is to permit the rapid segmentation of different types of tissue without the need for chemical dyes or contrast agents.<sup>10</sup> Last, the use of FT-IR imaging only involves light interacting with a sample and, unlike conventional biochemical analysis methods, does not alter the tissue in any manner. Thus it can provide additional information for pathology without the necessity of additional materials, tissue samples or changes in clinical protocols.

In this manuscript we use breast tissue as an example to illustrate the application of FT-IR imaging coupled with computerized classification for histopathology. Specifically, we demonstrate that a combination of FT-IR imaging, classification algorithms and integrated computational methods for enhancement of acquired data can be used in tandem to optimize the development of practical protocols for automated histopathology. Previous studies report on the potential for IR spectroscopy in breast pathology,<sup>12,13,14,15,16,17</sup> but no complete study on the spectral features of different histologic types of breast tissue exists. Preliminary efforts indicate significant spectral variation between different types of breast tissue and breast tumors,<sup>18,19,20</sup> but a protocol for clinical translation is lacking. We combine fast FT-IR imaging and tissue microarray sampling to demonstrate the effectiveness of our approach for automated breast histopathology on normal and malignant tissue from five patients. This approach is distinct from that in Raman spectroscopy, where histologic models are used in analyzing spectra.<sup>21,22</sup> As a first step towards automated tissue segmentation, we distinguish breast stroma and epithelium. This is a critical step, as over 99% of breast tumors arise in the epithelial tissue lining milk ducts and lobules.<sup>23</sup> False color classified images denoting stroma and epithelium are produced, followed by analysis of data collection parameters. We evaluate the impact of spectral resolution and noise on classification accuracy to demonstrate potential for faster data acquisition without loss in classification confidence. This study presents an initial effort in developing applications for FT-IR imaging in clinical pathology.

## 2. METHODOLOGY

### 2.1 Data Acquisition

The first studies to examine IR spectra of tissue began over fifty years ago,<sup>24</sup> but the field did not truly make progress due to limitations in instrumentation. Today, a combination of an IR microscope, Michelson interferometer and focal plane array (FPA) detector<sup>25</sup> permits efficient data acquisition for large sample areas. The data presented in this study is collected using the Perkin-Elmer Spotlight 400 imaging spectrometer. A spatial pixel size of 6.25 μm and a spectral resolution of 4 cm<sup>-1</sup> were employed, with 2 scans averaged for each pixel. An IR background is collected with 120 scans co-added at a location on the substrate where no tissue is present. No undersampling was employing in data acquisition and a NB medium apodization function was used. A ratio of the background to tissue spectra is then computed to remove substrate and air contributions to the spectral data. The Spotlight software atmospheric correction algorithm is applied to eliminate remaining atmospheric contributions to the tissue spectra. As opposed to other configurations that employ a large FPA detector, this instrument employs a linear array detector that is raster scanned to acquire data from large sample areas. We use a combination of instrument control and post-processing software to computationally re-organize data acquired into large image sizes. Images of stained tissue are acquired using a standard Zeiss optical microscope.

### 2.2 Tissue sampling

Tissue microarrays (TMAs) permit facile comparison of small tissue samples from numerous patients<sup>26</sup> and are an especially useful sampling medium for spectroscopic analyses.<sup>27</sup> A TMA contains numerous small round tissue samples, termed cores, which are extracted from biopsy samples from different patients. Two paraffin-embedded TMAs were obtained from a commercial source (US Biomax) for this study. The first TMA section is placed on a glass slide and stained with hematoxylin and eosin (H&E) dyes. In H&E staining, hematoxylin stains nucleic acids and eosin stains protein-rich tissue regions. This section is used for visual morphology interpretation by a pathologist. The second TMA section is placed on a barium fluoride (BaF<sub>2</sub>) substrate for FT-IR imaging. Though the arrays contained a large number

of samples, a smaller subset of malignant and normal tissue cores from five patients with invasive ductal carcinoma (IDC) is selected for this study as the illustrative example. Each of the ten cores is 1.5 mm in diameter; hence, at a 6.25  $\mu\text{m}$  pixel size, approximately 280,000 spectra are collected for each core. This results in the collection of over 560,000 spectra for each patient and approximately 2.8 million total spectra for all ten cores. This large spectral dataset facilitates rigorous validation of classification protocols at a pixel level. Paraffin is removed from the TMA by immersion in hexane with continuous stirring at 40 °C for 48-72 hours. Spectra are recorded at several locations on the TMA every 24 hours during this period to monitor paraffin removal with the disappearance of the 1462  $\text{cm}^{-1}$  peak.

### 2.3 Image analysis and classification

A supervised segmentation method is used for FT-IR image classification. This algorithm has been described in detail elsewhere,<sup>28</sup> but is based on a modified version of a Bayesian classifier. First, the spectral profile of 1641 bands is reduced to a set of 89 useful metrics by examination of spectra from manually selected stroma and epithelium tissue regions. Metrics are manually selected to include peak ratios, peak areas, and peak centers of gravity. A metric profile  $M$  is generated for each pixel in each tissue image of the form

$$M = [m_1, m_2, m_3, \dots, m_{n_m}], n_m=89 \quad (1)$$

where each  $m_i$  is the value for a single metric and  $n_m$  is the total number of manually selected metrics. Frequency distributions for stroma and epithelium are determined for each metric and used to estimate the probability of a given metric profile representing either of these two classes. The probability of an image pixel from each class  $c_i$  being represented by a given metric profile is determined using Bayes' Rule

$$p(c_i|M) = \frac{p(M|c_i)p(c_i)}{p(M)} \quad (2)$$

where  $p(M|c_i)$  is estimated from the metric class frequency distributions and  $p(M)$  is the probability of a given metric profile. The prior probability of particular tissue class  $p(c_i)$  in this model cannot be determined due the manual selection of tissue classes on FT-IR images, and is estimated as 0.5. Other ways to estimate or optimize the class prior probability may be utilized; we have noticed anecdotally, however, that the choice of this value across a large range does not significantly affect the classification results. Classification accuracy is estimated with receiver operating characteristic (ROC) analysis for selected tissue regions. The area under the ROC curve (AUC) is used to evaluate classifier sensitivity and specificity and estimate the potential of the algorithm for accurate histology determinations. The classification algorithm is trained on a large array dataset and separately validated on a second array. It is notable that we do not develop the entire classification algorithm anew here. First, the central idea of this manuscript is to demonstrate the optimization of a developed protocol and second, the sample sizes chosen here are insufficient for de novo algorithm development. Data is analyzed using the Environment for Visualizing Images (ENVI) software and with programs written in-house using Interactive Data Language (IDL).

### 2.4 Spectral resolution and noise analysis

Spectral resolution and noise are two common experimental variables that affect results in IR spectral analyses. The effects of spectral resolution and spectral noise are evaluated here in the context of quantitative histologic segmentation to minimize data collection time. As per the trading rules of IR spectroscopy, data collection time is expected to decrease linearly with spectral resolution and a quadratic rate with reduction in signal-to-noise ratio (SNR).<sup>29</sup> Ideally, these parameters would be analyzed by acquiring data at different spectral resolutions and numbers of spectral co-adds. However, the time required to collect multiple images for the TMA is prohibitive. Instead, computational methods are used to examine these parameters using the original FT-IR images acquired at 4  $\text{cm}^{-1}$  and 2 scans per pixel. First, spectral resolution is evaluated by downsampling the data using a neighbor binning procedure to resolutions of 8, 16, 32, 64 and 128  $\text{cm}^{-1}$ . Classification is then performed on downsampled datasets to determine the coarsest spectral resolution needed for satisfactory stroma and epithelium segmentation. For a fine spectral resolution data set at 4  $\text{cm}^{-1}$ , the effect of noise is evaluated by adding to each spectrum noise in Gaussian distributions with standard deviations of 0.001, 0.01, and 0.1 au. Classification accuracy is estimated by evaluating the AUC at each noise standard deviation. Computational noise reduction with the minimum noise fraction (MNF) transform<sup>30</sup> is evaluated by reducing noise in all the data sets. Classification is performed with the same algorithm on these MNF transformed images to determine the impact of this noise reduction algorithm on stroma and epithelium segmentation.

### 3. DATA

The classification model presented in this manuscript involves segmentation of stroma and epithelium, which are the two most prominent tissue classes in fixed breast tissue used for pathology evaluation.<sup>31</sup> In practice, the recognition of epithelial cells is especially critical for cancer diagnoses, as the vast majority (>99%) of breast cancers arise in this cell type.<sup>23</sup> Hence, the two class model is of practical significance. While seemingly simple and practical, however, the model can potentially be confounding as stroma consists of many cell types with disparate spectral characteristics. This model was employed to develop a classifier using training data from a TMA with forty patients. Final model calibration for sixty eight tissue cores yielded an AUC value of 0.99 with an eight metric classifier.<sup>32,33</sup> In this study we validate this classifier with one malignant and a matched normal TMA core from a subset of five patients. As seen in Figure 1A and B, absorbance images based on spectral features closely compare with images of H&E stained tissue. Hence, using conventional pathology knowledge we can select image pixels that unequivocally correspond between the two images - representing both stroma and epithelium. These pixels are selected by examining FT-IR images at  $1080\text{ cm}^{-1}$  to highlight asymmetric  $\text{PO}_2$  stretching vibrations in glycoprotein in epithelium,<sup>14</sup>  $1236\text{ cm}^{-1}$  to highlight  $\text{CH}_2$  wagging vibrations associated with collagen proteins,<sup>34</sup>  $1652\text{ cm}^{-1}$  to highlight  $\text{C=O}$  stretching vibrations at the protein amide I mode,<sup>34</sup> and  $3292\text{ cm}^{-1}$  to highlight NH bending vibrations at the protein amide A mode (shown as an example in Figure 1B).<sup>35</sup> We emphasize that multiple vibrational modes must be examined in tandem and pixels identified with great care and diligence as these form the gold standard for future comparisons. Over 185,000 pixels are marked in these ten tissue cores to serve as the gold standard for ROC analysis (as shown in Figure 1C). Selecting this large set of pixels is important to achieve a reasonable sample size to accurately estimate classification potential for the entire data set. Boundary pixels are not marked to avoid errors associated with mixed pixels in FT-IR images.<sup>27</sup> A qualitative comparison of stained and classified images indicates that stroma and epithelium segmentation is reasonable (Figure 1D), and this is confirmed with an AUC value of 0.98 after quantitative ROC analysis. Stroma and epithelium are easily identified on false color classified images without detailed examination and interpretation. This is advantageous over traditional staining methods that require the use of chemical dyes and subsequent expert pathologist examination for evaluation.

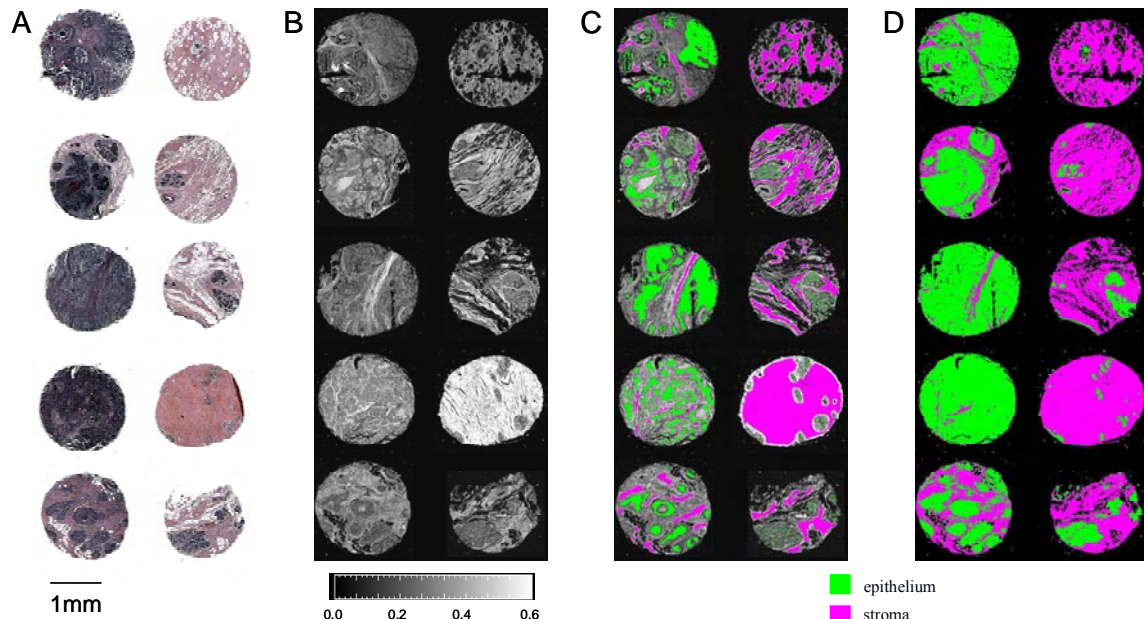


Fig. 1. Conventional H&E stained images, FT-IR spectral images and classification. (A) An H&E stained image of tissue cores from five invasive ductal carcinoma patients. Each row represents a single patient, with malignant tissue samples on the left and normal samples on the right. (B) An FT-IR image at  $3292\text{ cm}^{-1}$  denotes the NH bending vibration at the amide A protein mode. Brighter regions denote relatively protein-rich stroma. (C) A ground truth FITR image with pixels marked as stroma or epithelium serves as the gold standard for ROC analysis and classification evaluation. (D) A classified FT-IR image in which all pixels are labeled as stroma or epithelium accurately corresponds to the H&E stained image. The classification does not require stains or human interpretation.

## 4. RESULTS

### 4.1 Effect of spectral resolution on tissue segmentation

The impact of spectral resolution on classification performance is evaluated by downsampling spectra at every pixel with a neighbor binning and interpolation procedure. FT-IR image data sets are acquired at  $4\text{ cm}^{-1}$  spectral resolution and are downsampled to 8, 16, 32, 64, and  $128\text{ cm}^{-1}$  resolution. As seen in Figure 2A, an average spectrum at each resolution from epithelial cells in the gold standard demonstrates that important spectral elements remain identifiable at coarser resolutions. While we anticipate that the area under the peaks would be preserved, peak shapes begin to change at a coarser spectral resolution of 32 or  $64\text{ cm}^{-1}$  due to overlaps in the complicated spectral response. It would not be surprising to note that the most robust predictors of class incorporate best both biological diversity and spectral noise (arising from both measurement and artifacts). Hence, we anticipate that the use of these metrics would also prove robust when spectra are downsampled. Figure 2B demonstrates that the classification accuracy is not significantly affected until the spectral resolution is decreased to  $128\text{ cm}^{-1}$ .

The result is indeed surprising as numerous prior biomedical studies with vibrational spectroscopy have employed  $4\text{ cm}^{-1}$  to  $16\text{ cm}^{-1}$  spectral resolution. There are two important differences between the problem here and a majority of those studies. First, many of the reported studies used sensitive spectral analysis tools (e.g. second derivatives) or were looking for fine spectral features. Second, models for pathology may have needed more complex information. Here, we are examining a 2 class problem of very distinct cell types. Hence, the acceptable classification at very coarse resolutions is likely permitted by the significant biochemical differences between stroma and epithelium in the metrics selected. Previous studies have provided evidence of clear differences in IR spectra from DNA-rich tissues such as epithelium and RNA and protein-rich tissues such as stroma,<sup>14,20</sup> especially in the IR fingerprint region from  $500\text{-}1500\text{ cm}^{-1}$ .<sup>8</sup> We hypothesize that a more complex model with additional tissue classes would likely require a higher spectral resolution for reasonable classification, but that this resolution is not required to distinguish stroma and epithelium.

A powerful feature of the algorithm we employ is the utilization of prominent spectral features for classification. Here, the features selected as classification metrics are not very sensitive to changes in spectral resolution.<sup>36</sup> Absorbance values are accurate if the peak full width at half maximum (FWHM) is not significantly less than the spectral resolution. As biological materials have broad and overlapping lineshapes, the condition holds even for very coarse resolutions. Therefore, the values of spectral metrics are not significantly altered even if some details in the spectrum are affected at coarser spectral resolutions. The center of gravity metrics used for classification are particularly robust, as they incorporate peak position and shape and are not strongly influenced by peak modifications in downsampled spectra. Care must be exercised in making this extrapolation to all data quality. For example, for poor signal to noise ratio spectra, the center of gravity calculation will be sensitive to noise.

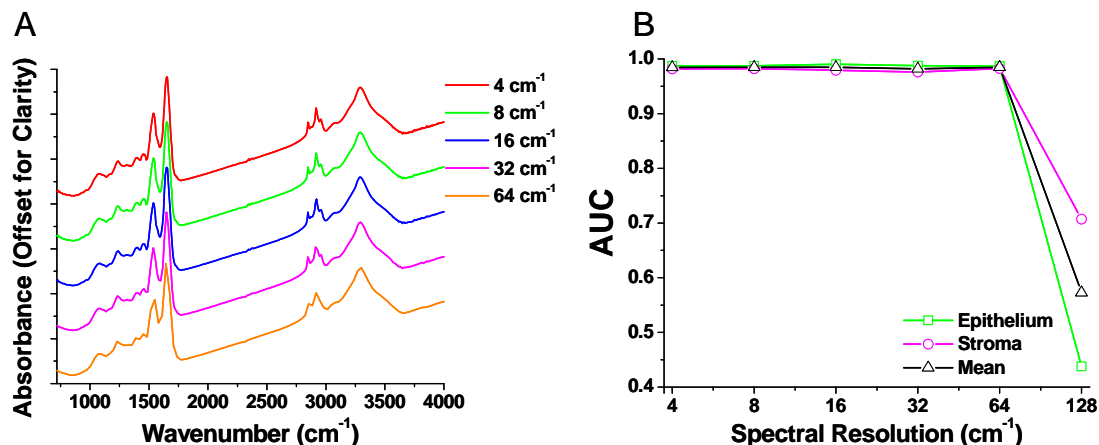


Fig. 2. Spectral resolution effect on classification. (A) Epithelial spectra obtained by downsampling data acquired at  $4\text{ cm}^{-1}$  indicate that IR spectrum quality degrades appreciably at a spectral resolution coarser than  $16\text{ cm}^{-1}$ , as anticipated for condensed phase biological materials. (B) AUC analysis for stroma and epithelium segmentation for each resolution demonstrates a significant decrease in classification accuracy only at a very coarse spectral resolution beyond  $64\text{ cm}^{-1}$ .

The effective classification in downsampled FT-IR images presented in this manuscript indicates potential for faster data acquisition without significant loss in classification accuracy. Figure 2 suggests that no significant classification differences are observed in images up to  $64\text{ cm}^{-1}$ . Since data acquisition time is estimated to decrease linearly with spectral resolution,<sup>29</sup> FT-IR images could be acquired 16 times as fast without any loss in classification performance for the two class model presented in this manuscript. Again, we emphasize that the results are preliminary and should be carefully validated. Nevertheless, the idea of optimizing data acquisition by modeling the results of other experimental conditions is an important one that should be pursued in practical translation of these protocols for clinical use.

#### 4.2 Effect of spectral noise on tissue segmentation

Evaluation of acceptable spectral noise for FT-IR image classification is important for efficient data collection. For practical applications, it is advantageous to acquire data with the lowest SNR that permits reasonable classification. Raw data is acquired with a peak-to-peak noise value of 0.011 au, a root mean square (rms) noise value of 0.008 au, and an average amide I height of 0.328 au. To assess the impact of spectral noise on classification accuracy, Gaussian noise is added with a standard deviation of 0.001, 0.01, and 0.1 au. Figure 3 provides a qualitative evaluation of histologic images from the acquired data set (Figure 3A) and from the data sets with added Gaussian noise (Figures 3B-D).

These images indicate that acceptable classification is achieved when noise is added at a standard deviation of 0.001 au (Figure 3B), but that classification accuracy appreciably decreases with the addition of noise at or above a standard deviation of 0.01 au. This is expected, since adding noise at a standard deviation of 0.001 au does not significantly change the FT-IR image data SNR. The data set with noise added at a standard deviation of 0.01 au (Figure 3C) produces a classified image with regions of distinguishable stroma and epithelium, although there are numerous stray pixels that are not correctly classified, similar to salt and pepper noise. Upon the addition of noise of ~0.1 au, classified images become completely indistinguishable (Figure 3D), including the misidentification of many pixels on the empty region of the slides as tissue. This loss in classification accuracy is caused by an underlying broadening of spectral metric distributions for each class. This broadening bridges the difference in metric values. The overlap in values in turn decreases classification confidence as measured by the AUC. Hence, we have used the AUC as a reasonable measure of the classification accuracy at every experimental condition.

A plot of AUC against the added noise (Figure 3E) demonstrates that the AUC value remains relatively constant with the addition of low levels of noise. It then decreases to a mean AUC of 0.77 with the addition of noise at a standard deviation of 0.01 au and falls to a mean AUC of ~0.5 at a noise standard deviation of 0.1 au. It is surprising that the stroma AUC actually falls below 0.5. Though the AUC values should not be below 0.5 for classified images, our algorithm contains a pixel rejection step. A pixel is rejected if the measured metric values do not lie within the prior probability distributions. Hence, a small number of pixels are rejected at low noise levels and are not accounted.

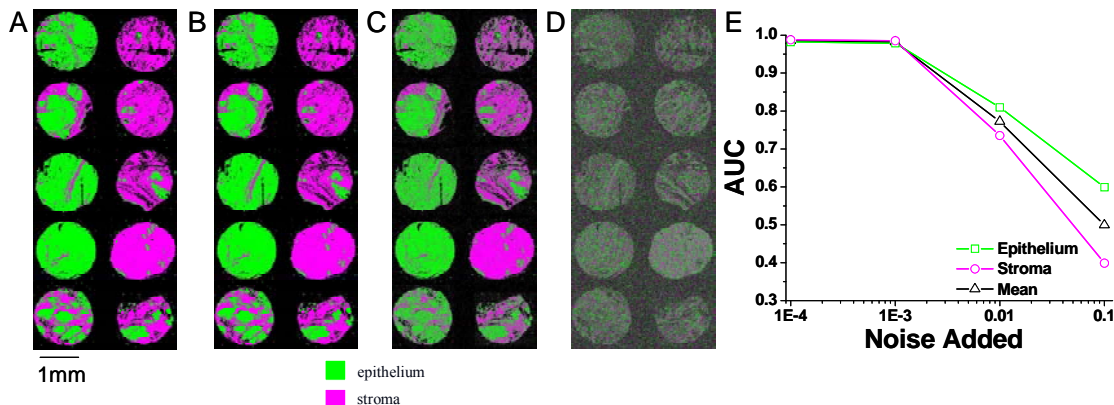


Fig. 3. Effect of noise on FT-IR image classification. Classified images are shown for (A) raw data, (B) data with Gaussian noise added at a standard deviation of 0.001 au, (C) data with Gaussian noise added at a standard deviation of 0.01 au, and (D) data with Gaussian noise added at a standard deviation of 0.1 au. (E) The AUC values for classification with noise added at a standard deviation of 0.001, 0.01, and 0.1 au confirm that classification accuracy is reasonable with a small amount of additional noise but unsatisfactory in data with a noise standard deviation at or above 0.01 au.

For the two class stroma and epithelium segmentation model presented in this manuscript, an AUC value of 0.77 does not indicate sufficient classification confidence. We would expect nearly perfect discrimination of these two types of tissue since there are numerous spectral features that distinguish epithelium and stroma.<sup>14,20,32,34</sup> An estimated classification accuracy of 0.5 for this model is equivalent to random guessing and does not provide any information about tissue histology. Examination of the curve in Figure 3E indicates that some additional spectral noise at a level of 0.001 can be present without loss in classification accuracy for this two class model. We did not observe any difference in this behavior with pathology of the tissue. Breast tumor tissue is often very heterogeneous and precise pixel classification is needed to produce reasonable automated classification results. Hence these results represent a good starting point to optimize a practical protocol. There may also be a patient or clinical setting dependence of these optimal operating points that remains to be probed. From the plot, it is likely that we are close to the operating point of a practical protocol, as addition of a small amount of noise ( $>0.01$  au) makes the classification unstable.

Last, the classification algorithm was optimized using a noise level similar to that of the acquired data set presented in this manuscript. Hence, the optimal metric sets and discriminant function are obtained for that noise level. It would not prove surprising if a de novo training and optimization of lower quality data could yield similar results. A de novo classification algorithm development, however, is not guaranteed to produce equivalent results for the higher noise cases and will fail where overlap between the prior distributions is significant due to noise broadening. Hence, we believe that the conditions found here are close to optimal.

#### 4.3 Noise reduction with the MNF transform

In this manuscript, we have used an instrument with a high performance detector that has a low multichannel detection advantage. FT-IR imaging using large focal plane array (FPA) detectors, however, is a promising avenue for rapid data acquisitions due to the large multichannel advantage. Imaging with FPAs, unfortunately, often results in low signal-to-noise (SNR) data due to the poor detector characteristics and other limitations.<sup>37</sup> From the trading rules of FT-IR spectroscopy,<sup>29</sup> achieving a factor of  $n$  improvement in SNR would result in a increase of  $n^2$  in data collection time. An alternative to improve SNR is to employ post-processing algorithms to reduce noise. One such avenue for noise reduction is the use of the minimum noise fraction (MNF) transform. The MNF transform can be used in a mathematical procedure to remove uncorrelated contributions from the spatial and spectral domains. First, a forward transform is used to perform a factor analysis and re-order spectral data in the order of decreasing SNR. The MNF calculation is a two-step process. A noise covariance matrix is estimated and used to decorrelate and rescale the noise in the data. Subsequently, a standard PCA performed on the noise-whitened data. A second step is to select only those factors that correspond to a sufficiently high SNR by examining the eigenvalue images. The first few eigenvalue images generally correspond to higher SNR values and contain most of the useful information. Noise reduction is achieved by suppressing the later factors corresponding largely to noise or zero-filling components and inverse transforming the data. A noise reduction by a factor greater than 5 could be achieved by this technique if the initial SNR is sufficiently high.<sup>38,39</sup> Though the utility of this method is demonstrated for IR imaging,<sup>40</sup> its use has not been widespread. Further, the use of MNF transformed data for tissue classification has not been attempted.

We propose to use the MNF transform route as a method for fast data acquisition without loss in classification accuracy. The protocol involves rapid data collection at a low SNR, followed by application of MNF transform for noise reduction. Classification is then performed on these noise-reduced images. It must be noted that the gain here is through computational techniques and does not involve changes in instrumentation hardware or data acquisition time. A secondary advantage that may arise is that decreasing the variance in spectral data could also decrease the biologic variance in the data and should improve separation of tissue classes. Excessive image noise will broaden spectral metric distributions for each class, which increases the error associated with each metric and decreases classification confidence. Therefore, if the metric distribution mean values for each class are sufficiently different decreasing noise will decrease the area of metric distribution overlap and improve segmentation confidence.

The impact of noise reduction on classification is demonstrated in Figure 4. The MNF transform-based protocol is applied to the acquired data set and the data sets with Gaussian noise added as discussed in the previous section. Classified images are displayed for each noise level after MNF transform-aided noise reduction (Figures 4A-D). The AUC values for the MNF transformed image sets are compared with the AUC values for noisy images (Figure 4E).

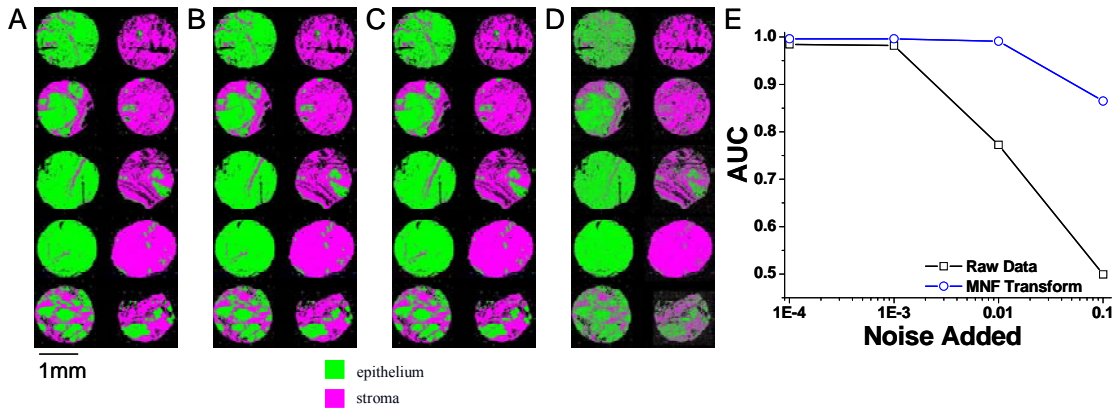


Fig. 4. Improvement in automated FT-IR image classification with the application of the MNF transform. Classified images from MNF transformed FT-IR images are shown for (A) raw data, (B) data with Gaussian noise added at a standard deviation of 0.001 au, (C) data with Gaussian noise added at a standard deviation of 0.01 au, and (D) data with Gaussian noise added at a standard deviation of 0.1 au. (E) Comparing AUC values for original FT-IR images and MNF transformed FT-IR images demonstrates that classification improves with noise reduction, especially when the noise has a standard deviation of 0.01 - 0.1 au.

Evaluation of classified images and AUC values indicates that the MNF transform improves classifier performance for each image. Given that the classification accuracy was very high, the effects of MNF transform are significant only when the noise level degrades the original data. Nevertheless, it can be seen from the figure that the high accuracy is recovered for an order of magnitude increase in data noise. Therefore, application of the MNF transform on data acquired with these noise distributions will make a significant difference in classifier performance. Specifically, we can acquire data with a noise standard deviation of 0.01 au and provide accuracy levels that are comparable to those obtained in our measurements of lower noise. This finding is significant in that noise levels of 0.01 au are commonly obtained in rapidly acquired FT-IR imaging data sets with large array detectors. Further, since the classification accuracy seems to be little affected by spectral resolution, we can anticipate that it will be little affected by the choice of an apodization function and other minor sources of error for a reasonable spectral resolution. Hence, we contend that the protocol developed here would be well-suited to rapid imaging with large array detectors.

## 5. CONCLUSIONS

Recent developments in FT-IR imaging and data processing facilitate new applications for this technology. In this manuscript, we report an initial application in automating histopathology of breast tissue. Supervised segmentation of breast stroma and epithelium in FT-IR images is presented and nearly-perfect classification accuracy is estimated. The impacts of spectral resolution and noise on image classification are evaluated. Results in this paper demonstrate that spectral resolution can be decreased 16-fold without loss in classification accuracy. The classification algorithm is more sensitive to noise, but noise reduction with the MNF transform can improve classification accuracy while decreasing the time required for data collection. This evaluation of the impact of experimental parameters on classification accuracy represents a first step in developing a practical protocol for rapid and automated histopathology.

## REFERENCES

- [1] L. Benoit, P. Fayoulet, F. Collin, L. Arnould, J. Fraisse, and J. Cuisenier, "Histological and cytopathological cancer specimens: good practice in the operating room," *Ann. Chir.*, 128, 637-641 (2003).
- [2] A. Creager and K. Geisinger, "Intraoperative evaluation of sentinel lymph nodes for breast carcinoma: current methodologies," *Adv. Anat. Pathol.*, 9(4), 233-243 (2002).
- [3] A. Cochran, R. Huang, J. Guo, and D. Wen, "Current practice and future directions in pathology and laboratory evaluation of the sentinel node," *Ann. Surg. Oncol.*, 8(9 Suppl.), 13S-17S (2001).

[4] M. Simunovic, A. Gagliardi, D. McCready, A. Coates, M. Levine, and D. DePetrillo, "A snapshot of waiting times for cancer surgery provided by surgeons affiliated with regional cancer centers in Ontario," *CMAJ*, 165(4), 421-425 (2001).

[5] E. Rakovitch, A. Mihai, J. Pignol, W. Hanna, J. Kwinter, C. Chartier, I. Ackerman, J. Kim, K. Pritchard, and L. Paszat, "Is expert breast pathology assessment necessary for the management of ductal carcinoma in situ?," *Breast Cancer Res. Treat.*, 87, 265-272 (2004).

[6] E. Newman, A. Guest, M. Helvie, M. Roubidoux, A. Chang, C. Kleer, K. Diehl, V. Cimmino, L. Pierce, D. Hayes, L. Newman, and M. Sabel, "Changes in surgical management resulting from case review at a multidisciplinary tumor board," *Cancer*, 107, 2346-2351 (2005).

[7] D. Slamon, G. Clark, S. Wong, W. Levin, A. Ullrich, and W. McGuire, "Human breast cancer: correlation of relapse and survival with amplification of the HER-2/neu oncogene," *Science*, 235(4785), 177-182 (1987).

[8] D. Naumann, "FT-infrared and FT-Raman spectroscopy in biomedical research," *Appl. Spec. Review*, 36(2-3), 239-298 (2001).

[9] D. Ellis and R. Goodacre, "Metabolic fingerprinting in disease diagnosis: biomedical applications of infrared and Raman spectroscopy," *Analyst*, 131, 875-885 (2006).

[10] G. Srinivasan and R. Bhargava, "Fourier transform-infrared spectroscopic imaging: the emerging evolution from a microscopy tool to a cancer imaging modality," *Spectroscopy*, 22(7), 30-43 (2007).

[11] I.W. Levin and R. Bhargava, "Fourier transform infrared vibrational spectroscopic imaging: integrating microscopy and molecular recognition," *Annu. Rev. Phys. Chem.*, 56, 429-474 (2005).

[12] M. Diem, M. Romeo, S. Boydston-White, M. Miljkovic, and C. Matthaus, "A decade of vibrational micro-spectroscopy of human cells and tissue (1994-2004)," *Analyst*, 129, 880-885 (2004).

[13] H. Fabian, N. Thi, M. Eiden, P. Lasch, J. Schmitt, and D. Naumann, "Diagnosing benign and malignant lesions in breast tissue sections by using IR-microspectroscopy," *Biochim. Biophys. Acta*, 1758(7), 874-882 (2006).

[14] H. Fabian, M. Jackson, L. Murphy, P. Watson, I. Fichtner, and H.H. Mantsch, "A comparative infrared spectroscopic study of human breast tumors and breast tumor cell xenografts," *Biospectroscopy*, 1, 37-45 (1995).

[15] Y. Ci, T. Gao, J. Feng and Z. Guo, "Fourier transform infrared spectroscopic characterization of human breast tissue: implications for breast cancer diagnosis," *Appl. Spec.*, 53(3), 312-315 (1999).

[16] C. Liu, Y. Zhang, X. Yan, X. Zhang, C. Li, W. and Yang, and D. Shi, "Infrared absorption of human breast tissues in vitro," *J. Lumin.*, 119-120, 132-136 (2006).

[17] C. Petibois, and G. Deleris, "Chemical mapping of tumor progression by FT-IR imaging: towards molecular histopathology," *Trends Biotechnol.*, 24(10), 455-462 (2006).

[18] M. Jackson, J. Mansfield, B. Dolenko, R. Somorjai, H.H. Mantsch, and P. Watson, "Classification of breast tumors by grade and steroid receptor status using pattern recognition analysis of infrared spectra," *Cancer Detect. Prev.*, 23(3), 245-253 (1999).

[19] R. Eckel, H. Huo, W. Guan, X. Hu, X. Che, and W.D. Huang, "Characteristic infrared spectroscopic patterns in the protein bands of human breast tissue," *Vib. Spec.*, 27, 165-173 (2001).

[20] M. Diem, S. Boydston-White, and L. Chiriboga, "Infrared spectroscopy of cells and tissues: shining light onto a novel subject," *Appl. Spec.*, 53(4), 148A-161A (1999).

[21] A. Haka, K. Shafer-Peltier, M. Fitzmaurice, J. Crowe, R.R. Dasari, and M.S. Feld, "Diagnosing breast cancer by using Raman spectroscopy," *Proc. Natl. Acad. Sci. USA*, 102(35), 12371-12376 (2005).

[22] P. Matousek and N. Stone, "Prospects for the diagnosis of breast cancer by noninvasive probing of calcifications using transmission Raman spectroscopy," *J. Biomed. Opt.*, 12(2), 024008 (2007).

[23] C. Adem, C. Reynolds, J. Ingle, and A.. Nascimento, "Primary breast sarcoma: clinicopathologic series from the Mayo Clinic and review of the literature," *Br. J. Cancer*, 91(2), 237-241 (2004).

[24] E. Blout, and R. Mellors, "Infrared Spectra of Tissues," *Science*, 110, 137-138 (1949).

[25] E.N. Lewis, P.J. Treado, R.C. Reeder, G. Story, A. Dowrey, C. Marcott, and I.W. Levin, "Fourier transform spectroscopic imaging using an infrared focal-plane array detector," *Anal. Chem.*, 67, 3377-3381 (1995).

[26] J. Kononen, L. Bubendorf, A. Kallioniemi, M. Barlund, P. Schraml, S. Leighton, J. Torhorst, M. Mihatsch, G. Sauter, and O. Kallioniemi, "Tissue microarrays for high-throughput molecular profiling of tumor specimens," *Nat. Med.*, 4(7), 844-847 (1998).

[27] D.C. Fernandez, R. Bhargava, S.M. Hewitt, and I.W. Levin, "Infrared spectroscopic imaging for histopathologic recognition," *Nat. Biotechnol.*, 23(4), 469-474 (2005).

[28] R. Bhargava, D.C. Fernandez, S.M. Hewitt, and I.W. Levin, "High throughput assessment of cells and tissues: Bayesian classification of spectral metrics from infrared vibrational spectroscopic imaging data," *Biochim. Biophys. Acta*, 1758(7), 830-845 (2006).

[29] P.R. Griffiths and J. De Haseth, *Fourier Transform Infrared Spectroscopy*, John Wiley & Sons, New York, 1986.

[30] A. Green, M. Berman, P. Switzer, and M. Craig, "A transformation for ordering multispectral data in terms of image quality with implications for noise removal," *IEEE Trans. Geosci. Remote Sensing*, 26, 65-74 (1988).

[31] P.P. Rosen, *Rosen's Breast Pathology*, Lippincott, Williams, and Wilkins, Philadelphia, 2001.

[32]. F.N. Keith and R. Bhargava, "Data processing for tissue histopathology using Fourier transform infrared spectra," *Proc. Asilomar Conference on Systems, Signals, and Computers*, 71-75 (2006).

[33]. F.N. Keith and R. Bhargava, "Towards automated breast histopathology using mid-IR spectroscopic imaging," *Technol. Cancer Res. Treat.*, in preparation.

[34] M. Jackson, L. Choo, P. Watson, W. Halliday, and H.H. Mantsch, "Beware of connective tissue proteins: assignment and implications of collagen absorptions in infrared spectra of human tissues," *Biochim. Biophys. Acta*, 1270, 1-6 (1995).

[35] R. Salzer, G. Steiner, H.H. Mantsch, J. Mansfield, and E.N. Lewis, "Infrared and Ramen imaging of biological and biomimetic samples," *Frensenius J. Anal. Chem.*, 366, 712-726 (2000).

[36] R. Bhargava, "Towards a practical Fourier transform infrared chemical imaging protocol for cancer histopathology," *Anal. Bioanal. Chem.*, 389, 1155-1169 (2007).

[37] C.M. Snively and J.L. Koenig, "Characterizing the performance of a fast FT-IR imaging spectrometer," *Appl. Spec.*, 53(2), 170-177 (1999).

[38] R. Bhargava, S.Q. Wang, and J.L. Koenig, "Route to higher fidelity FT-IR imaging." *Appl. Spec.*, 54(4), 486-495 (2000).

[39] R. Bhargava, T. Ribar, and J.L. Koenig, "Towards faster FT-IR imaging by reducing noise," *Appl. Spec.*, 53(11), 1313-1322 (1999).

[40] M. Wabomba, Y. Sulub, and G. Small, "Remote Detection of Volatile Organic Compounds by Passive Multispectral Infrared Imaging Measurements," *Appl. Spec.*, 61(4), 349-358 (2007).